EFFECTS OF CONFINED STRUCTURES ON POOL BOILING HEAT TRANSFER

A Thesis

by

HAO-EN LEE

Submitted to the Office of Graduate and Professional Studies of
Texas A&M University
in partial fulfillment of the requirements for the degree of

MASTER OF SCIENCE

Chair of Committee,	Jorge L. Alvarado
Committee Members,	Yassin A. Hassan
	Sungyon Lee
Head of Department,	Andreas A. Polycarpou

May 2016

Major Subject: Mechanical Engineering

ABSTRACT

Pool boiling heat transfer is one of the most effective heat transfer processes used in a host of applications. The enhancement of pool boiling has been studied for decades by considering a variety of surface modifications and configurations. For that reason, this study investigates the effects of the confined structures on the pool boiling heat transfer. The confined structures consist of flanges, a plate with a central orifice and a mesh with a central orifice. The diameters of the plate orifice are 2 and 4 mm; the diameter of the mesh orifice size are 2.5, 3.5, 4.5 mm. By comparing the boiling curves of different confined structures, the effects of confinement on heat transfer performance can be evaluated. An infrared camera and a high speed camera were used to capture bubble images and for measuring surface temperature. Furthermore, a pump assisted system was used to determine the effect of confinement on vapor quality and system pressure.

The test results show that pool boiling heat transfer can be generally enhanced by using confined structures. The level of enhancement depends on the orifice size of the plate and the mesh. Smaller orifice size leads to higher heat transfer enhancement. The results of the pump assisted test indicate that the boiling heat transfer enhancement can be attributed to the bubble coalescence process and the induced shear flow caused by the coalesced bubble departure. Results also indicate than an increase of vapor generation (quality) and the induced shear flow rate (shear stress) can be found when increasing the level of confinement on the pool boiling process. Furthermore, using a mesh in confined

structure can provide a higher heat transfer coefficient when compared to the no-mesh cases when a pump is used to facilitate bubble departure. In summary, the results show that using meshes leads to better heat transfer performance, which cannot be replicated using a solid surface as confinement structure.

DEDICATION

To Dr. Jorge L. Alvarado for his support and inspiration

To my family for their unconditional love

ACKNOWLEDGEMENTS

I would like to thank my committee chair, Dr. Alvarado, and my committee members, Dr. Hassan and Dr. Lee, for their guidance and support throughout the course of this research.

Thanks also go to my friends and colleagues and the department faculty and staff for making my time at Texas A&M University a great experience.

Finally, thanks to my mother and father for their encouragement and patience.

NOMENCLATURE

$A_v(r)$	local vapor area
$A_l(r)$	local liquid area
Bo	boiling number
C_{sf}	experimental value depending on liquid-surface combination
c_{pl}	liquid specific heat
d	diameter of the cylinder
F_{fl}	fluid-dependent parameter
f	bubble frequency
g	gravitational acceleration
h	local heat transfer coefficient
h_c	confined pool boiling heat transfer coefficient
h_{uc}	unconfined pool boiling heat transfer coefficient
h_{lv}	latent heat of vaporization per unit mass
h_{lo}	heat transfer coefficient with total liquid flow
h_{NBD}	nucleate boiling dominant heat transfer coefficient
h_{CBD}	convective boiling dominant heat transfer coefficient
h_{TP}	heat transfer coefficient during two-phase flow
Ja	Jakob number
k_l	thermal conductivity of liquid
L_b	length scale

L_c	capillary length of liquid
$\dot{m}$	total mass flow rate
$\dot{m}_v$	mass flow rate of vapor
Nu_b	Nusselt number
n'_a	density of active nucleation sites
Pr_l	liquid Prandtl number
q''	heat flux
$\overline{q''}$	mean surface heat flux
q''_{fc}	single phase liquid forced convection heat flux
q''_{pb}	pool boiling surface heat flux
q''_i	pool boiling threshold heat flux
q''_{max}	critical heat flux
Re_b	Reynolds number
R	bubble growth radius
$\dot{R}$	velocity of vapor-liquid interface
R_{max}	maximum bubble radius
$r_{orifice}$	plate orifice radius
Th	height of confined plate
ΔT	temperature difference
T_w	wall temperature
T_l	liquid bulk temperature

T_{sat}	saturation temperature
$t_l(r)$	local liquid thickness
$t_v(r)$	local vapor thickness
U_b	velocity scale
u_∞	cross-flow velocity
u_{in}	flow velocity at the circumference of confined plate
u_{exit}	flow velocity at the plate orifice
u(r,z)	local liquid velocity
$u_{max}(r)$	local liquid maximum velocity
u_{mix}	local two-phase flow velocity
x	two-phase flow quality
X(r)	local two-phase flow quality as function of r
X_m	measured two-phase flow quality
η	pump influence factor
μ	kinematic viscosity
μ_l	liquid viscosity
ρ_v	vapor density
ρ_l	liquid density
ρ_{mix}	two-phase flow quality
σ	interfacial tension
τ	local shear stress

TABLE OF CONTENTS

Page

LIST OF FIGURES

Page

LIST OF TABLES

1. INTRODUCTION

1.1 Background & motivation

Boiling is a phase change phenomenon that takes place between liquid and vapor phases. Vapor bubbles form when enough energy is provided to the liquid medium at the corresponding saturation temperature. Contrary to boiling, condensation is the process in which vapor is removed by using relatively cold surface or adjacent liquid. Under the right conditions, the phase change process can efficiently transfer large amounts of heat with only a small temperature difference between liquid and solid surface or vapor and solid surface. Consequently, many applications in industry are related to this topic, from crude oil distillation to high performance computer chip heat dissipation. Because of its pragmatic value, the liquid-vapor phase change process has been studied by many researchers in past several decades. However, the complexity of the phase change heat transfer mechanisms still is very difficult to understand. Hence, further research is required, specifically in pool boiling applications.

The boiling process can be classified into two main categories: pool boiling and forced convection boiling. Pool boiling refers to the boiling process at the surface of a body or heating element immersed in an extensive pool of motionless liquid [1]. The motion of fluid flow is driven by the buoyancy force caused by the motion of low density vapor bubbles. Pool boiling can be further characterized into two groups based on liquid pool temperature. When pool boiling happens in liquid pool temperature below the liquid saturation temperature, the process is name subcooled pool boiling. The vapor

bubble after departure from the heated surface will then condense back in the liquid pool. When the pool boiling happens in a saturated liquid pool, this process is named saturated pool boiling. Contrary to pool boiling, the fluid motion for forced convection boiling mainly comes from external force. Forced convection boiling strongly depends on the geometrical condition of the system and the corresponding flow structure. It can also be categorized into two groups: external flow boiling and internal flow boiling.

The history of research in pool boiling dates back to the 1930's. Nukiyama [2] first investigated the pool boiling process and identified different regimes in saturated pool boiling in 1934. These regimes can be described by the boiling curve, which is still widely used in pool boiling analysis. In different boiling curve regimes, bubble motion, heat transfer coefficient and dominant heat transfer mechanism are different. After Nukiyama's research, additional models were proposed to describe the pool boiling heat transfer and fluid motion based on simple postulations. Several correlations for nucleate boiling heat transfer data were also made by researchers such as Rohsenow [3], Forster and Zuber [4], Borishanski [5] and Stephan et al [6]. However, the mechanisms of pool boiling are not yet fully understood. There are many parameters that affect the pool boiling heat transfer process including nucleation site density, bubble departure rate, bubble departure diameter, heated surface conditions, liquid properties and so on. Consequently, further research into the boiling mechanism is required.

In this project, enhancement of saturated nucleate pool boiling heat transfer was studied by using different confined structures, which can change the motion of fluid and

the shear flow velocity. With the utilization of confined structures, higher heat pool boiling transfer efficiency can be achieved.

1.2 Objective

The objective of this research was to investigate the relationship between confined structures and pool boiling heat transfer. By controlling the diameter of plate orifice, the diameter of mesh orifice and flanged structure, the influences of confined structures on pool boiling heat transfer efficiency can be analyzed. This research also investigated the mechanisms of confined pool boiling enhancement. An infrared camera and high speed camera were used to acquire the heated surface temperature profile and bubble images. Further, an assistant pump system and a pressure transducer were used to investigate the bubble departure mass flow rate and pressure inside confined space. By analyzing the data from the cameras and the pressure transducer while utilizing different confined structures, the causes of pool boiling enhancement are investigated and discussed.

2. LITERATURE REVIEW

2.1 Fundamentals of pool boiling

The boiling process is an intensive interaction between liquid and a heated surface. When the temperature of a heated surface is sufficiently high, the phase change process of liquid starts and converts liquid into vapor bubbles. Following is the review of the pool boiling basic concepts including the boiling curve, nucleate boiling models and system parametric effects on pool boiling.

2.1.1 Boiling curve

The boiling curve is the most widely used tool to understand pool boiling regimes. In the early investigations of pool boiling heat transfer, Nukiyama [2] was the first identify different regimes of pool boiling and described it in the boiling curve. The general boiling curve and boiling regimes are shown in Figures 1 and 2, demonstrates the relationship between heat flux input (q") and wall superheat ($T_w - T_{sat}$), which is the difference between heated surface temperature and the liquid saturation temperature at certain pressure conditions. The boiling curve can be separated into five different regimes based on the vapor-liquid interaction. These five regimes are natural convection, isolated bubbles, slugs and columns, transition boiling and film boiling. The isolated bubbles regime and the slugs and columns regime can collectively refer to nucleate boiling regime.

At the natural convection regime (section A-B), the wall superheat is not high enough to initiate bubble formation. The dominant heat transfer process is the natural convection of liquid. If we gradually increase the wall superheat temperature, eventually the temperature will be sufficient to trigger bubble nucleation at some cavities on the surface. It would happen at point B, which is the onset of nucleate boiling (ONB). If the temperature of the surface is increased near the ONB point, the heat flux should suddenly increase without changing the superheat temperature. After ONB, further increase in wall temperature takes system into nucleate boiling regime (Section B-E). At lower wall superheat section, the bubbles generate at widely separated active sites. The regime is named isolated bubbles regime (Section B-D). With the increasing of the surface temperature, more cavities at the surface are activated. The bubbles start to coalesce and forming vapor columns near the surface. This regime is called the regime of slugs and columns (Section D-E). Vapor will start to accumulate at the surface with increasing surface temperature. Eventually, the heat flux will reach its peak value called the critical heat flux (CHF, Point E). If the surface temperature increases beyond the critical heat flux, a vapor film will form at the heated surface, which should lead to worse heat transfer performance and lower heat transfer coefficient in the transition regime (Section E-F). As the temperature continually increases, the heated surface will be entirely covered by a vapor film and reaching its minimum heat flux (Point F), where the film boiling regime starts. In the film boiling regime, the dominant heat transfer mechanisms are the conduction and the radiation of vapor film. In this regime, the heat flux increases with the heated surface temperature.

When using a temperature controlled heating system, if surface temperature is decreased from the film boiling regime, the system will progress through each regime reversely except with a little difference in the transition regime. On the other hand, when using a heat flux controlled heating system, the system will directly jump from Point E to Point G as the heat flux increases. The transition regime is not encountered in the heat flux controlled system. When decreasing heat flux from film boiling, the system will go through the path between Point F and Point C.

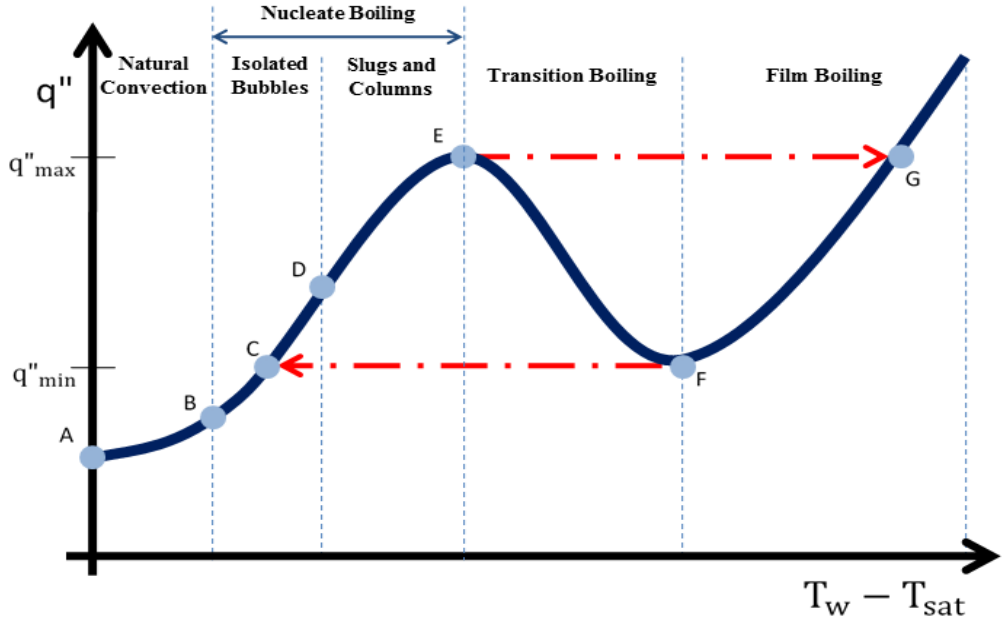

Figure 1. Boiling curve [1]

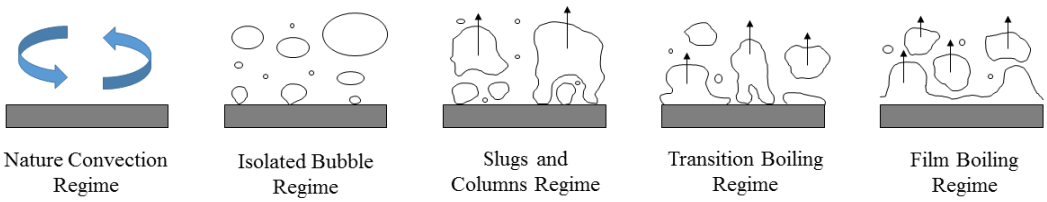

Figure 2. Bubble regimes [1]

2.1.2 Nucleate boiling models

Numerous investigations into the nucleate boiling mechanism have been done over the years. Several models had been proposed by researchers to describe the nucleate boiling process. This section will focus on some of the most frequently used models and the correlations related to them.

2.1.2.1 Rohsenow's model

Rohsenow's Model [3] is one of the most widely cited models in pool boiling research. Rohsenow studied and analyzed the heat transfer process from a heated surface to liquid in pool boiling as a single-phase convection process. The high heat transfer coefficient during pool boiling process is related to the agitation of liquid flow behind the wake of departing bubbles. The observations suggest that it was possible to correlate pool boiling data with a relation of the form:

$$Nu_b = \frac{hL_b}{k_l} = ARe_b^n Pr_l^m \tag{2.1}$$

Where the Reynolds number Re_b is given by

$$Re_b = \frac{\rho_v U_b L_b}{\mu_l} \tag{2.2}$$

Where L_b is an appropriate bubble length scale and the U_b is an appropriate velocity scale. The bubble departure diameter and the vapor superficial velocity were used as the length scale and the velocity scale in the Rohsenow's model.

The correlation Rohsenow used for the pool boiling heat transfer was first given as follows:

$$\frac{q"}{\mu_l h_{lv}}\left[\frac{\sigma}{g(\rho_l-\rho_v)}\right]^{\frac{1}{2}}=\left(\frac{1}{C_{sf}}\right)^{\frac{1}{r}} Pr_l^{\frac{-s}{r}}\left[\frac{c_{pl}\,\Delta\, T}{h_{lv}}\right]^{\frac{1}{r}} \tag{2.3}$$

With the recommended value of r = 0.33 and s = 1.7, equation 2.3 can be rearranged to the following form:

$$q" = \mu_l h_{lv}\left[\frac{g(\rho_l-\rho_v)}{\sigma}\right]^{\frac{1}{2}}\left(\frac{c_{pl}\,\Delta\, T}{C_{sf} h_{lv} Pr_l^{1.7}}\right)^3 \tag{2.4}$$

Where C_{sf} is the experimentally determined value depending on different liquid-surface combinations. A value of C_{sf} = 0.013 is recommended as a first approximation.

2.1.2.2 Microconvection model

The microconvection model was first proposed by Forster and Zuber [4]. Similar to Rohsenow's model, they assumed that heat transfer could be correlated using equation 2.1. Forster and Zuber used two times bubble growth radius, 2R as the length scale and

the velocity of vapor-liquid interface,$\dot{R}$ as the velocity scale. The bubble Reynolds number and the Nusselt number were:

$$Re_b = \frac{2R\rho_l\dot{R}}{\mu_l} = \pi Ja^2 Pr_l^{-1} \tag{2.5}$$

$$Nu_b = \frac{q"(2R)}{(T_w - T_l)k_l} \tag{2.6}$$

With equations 2.5 and 2.6, they were able to correlate pool boiling data using equation 2.1 with A = 0.0015, n = 0.62 and m = 0.33. Unlike Rohsenow's model, the heat transfer coefficient in Nusselt number was based on the temperature difference between the heated surface temperature and the liquid bulk temperature. The saturated pool boiling data generally support this correlation. However, in the significantly subcooled pool boiling, the liquid saturated temperature should be used instead of the liquid bulk temperature in equation 2.6 in order to achieve a better correlation.

2.1.2.3 Vapor-liquid exchange model

The vapor-liquid exchange model was first proposed by Forster and Greif [7]. They postulated that the bubble works as a micro pump inside the liquid pool. When the bubble grows, it would push the hot liquid out of near-wall region into the cold liquid pool. If the bubble departures or collapses, the cold liquid will be drawn to the heated surface. For each bubble, it can pump the same amount of liquid as its volume. Based on these postulations, the following correlation can be derived:

$$q'' = \rho_l c_{pl} \left(\frac{2\pi}{3}\right) R_{max}^3 \left(\frac{1}{2}\right) (T_w - T_l) f n_a' \tag{2.7}$$

With the similar vapor-liquid exchange concepts, a model was proposed by Mikic and Rohsenow [8-9]. They stated that the heat is transferred from the heated surface to the liquid through two main mechanisms: natural convection between active nucleation sites and the one dimensional transient conduction process into semi-finite medium after bubble departure. Their correlation of the mean surface heat flux can be derived in the following form:

$$q^* = \frac{\overline{q''}}{\mu_l h_{lv}} \left[\frac{\sigma}{g(\rho_l - \rho_v)}\right]^{\frac{1}{2}} = \mathrm{B}[\emptyset(T_w - T_{sat})]^{m+1} \tag{2.8}$$

$$\mathrm{B} = A_1^{\frac{2}{3}} A_2^{\frac{1}{2}} A_3 \left(\frac{2\pi^{\frac{1}{2}}}{g^{\frac{9}{8}}}\right) \left(\frac{R_0}{2}\right)^m \tag{2.9}$$

$$\emptyset = \left[\frac{k_l^{\frac{1}{2}} \rho_l^{\frac{17}{8}} c_{pl}^{\frac{19}{8}} h_{lv}^{m-\frac{23}{8}} \rho_v^{m-\frac{15}{8}}}{\mu_l (\rho_l - \rho_v)^{\frac{9}{8}} \sigma^{m-\frac{11}{8}} T_{sat}^{m-\frac{15}{8}}}\right]^{\frac{1}{(m+1)}} \tag{2.10}$$

Where A_1 and A_2 are determined experimentally. Both A_1 and A_2 depend on fluid types. A_3, R_0 and *m* are related to surface active sites conditions. Equation 2.8 is similar to equation 2.3, but equation 2.8 includes some physical properties of the fluid and the cavity size distribution.

2.1.3 System parametric effects on nucleate boiling

In Dhir's review of boiling heat transfer [10], he indicated that there are several system variables which affect the nucleate boiling heat transfer. Based on his review, these variables are listed below: surface finish, surface wettability, surface contamination, heater geometry, liquid subcooling, flow velocity, gravity, system pressure, thermal properties of the solid and the mode in which the tests are performed. In this section, the system variables that can significantly affect the nucleate pool boiling heat transfer will be introduced.

2.1.3.1 Surface finish

Many investigations into surface variables effects on nucleate boiling have been done [11]. It can be concluded that the rougher surface can provide better heat transfer performance for the same superheat temperature because of the higher density of the potential bubble nucleation sites. The rougher surface can shift the boiling curve to the left, which means the heat transfer performance is improved. Berenson [12] conducted a pool boiling experiment with n-pentane at atmospheric pressure. It was found that the critical heat flux and the film boiling regime were independent of surface conditions. However, the nucleate boiling heat transfer coefficient was improved by nearly 600% by changing the surface finish. It was also found by Bankoff [13] that only if the vapor can be trapped by the cavities associated with increased surface roughness, the surface roughness can affect the pool boiling heat transfer performance

2.1.3.2 Surface wettability

The surface wettability can significantly change the boiling curve. If the liquid could not wet the heated surface, the vapor blanket will quickly form over the heated surface after the boiling process was initiated. The boiling process immediately enters the film boiling regime. The nucleate boiling regime, the critical heat flux and the transition boiling regime will not be observed. The improvement on wettability will shift the boiling curve to the right. According to Phan and Hai Trieu et al. [14], the enhancement of wettability increases the bubble departure diameter but decreases the bubble departure frequency. Takata et al. [15] also investigated the wettability effects on boiling with the titanium dioxide (TiO_2) coated surface, which was a superhydrophilic surface. It was found that the critical heat flux of TiO_2 coated surface was about 2 times higher than the non-coated surface.

2.1.3.3 Heater geometry

The heater geometry can be categorized into two main groups: the heater orientation and the heater size. Kaneyasu et al. [16] studied the effect of heater orientation on the nucleate pool boiling of water at atmospheric pressure from a copper flat plate heater. The orientation of the heater was varied from 0^o to 175^o from horizontal plane. Kaneyasu et al. found that the heat transfer coefficient increased as the inclination angle increased. However, in the high heat flux region, there was no difference between different heater orientations. The capillary length of fluid (L_c) has been used to study the

effects of heater size by many researchers. The capillary length of fluid (L_c) can be given by the following form:

$$L_c = \sqrt{\frac{\sigma}{g(\rho_l - \rho_v)}} \tag{2.11}$$

Based on Park and Bergles experiments on the thin foil heater in R-113[17], the effects of heater size on the heat transfer performance in the nucleate pool boiling regime was insensitive compared to other boiling regimes. However, when using an extremely small heater, the nucleate boiling regimes might not happen [18]. Lu et al. [19] investigated the effect of heater size on the water pool boiling performance by using plan Si surface, which was covered with a dense array of Si nano-wires. It was found that if the heater length was smaller than 8 times of the capillary length, the critical heat flux significantly increased as the heater size decreased.

2.1.3.4 Liquid subcooling

The liquid pool subcooling could change the bubble departure mechanism. The bubble departed from the heated surface in subcooled liquid would soon condense back to the liquid pool. The effects of liquid subcooling in the nucleate boiling regime were usually not significant. However, the heat transfer in nature convection regime, transition boiling regime and film boiling regime would enhance by increasing liquid subcooling. The boiling curve would be shifted upward as subcooling increased. The

critical heat flux is strongly affected by the subcooling. Because of the condensation of departure bubbles, higher critical heat flux could be achieved.

2.1.3.5 Flow velocity

Flow velocity is another important factor that affects boiling phenomena. In general, increasing flow velocity would influence the bubble formation mechanism. Previous research studies show that the bubble departure diameter would decrease as the flow velocity increases [20-22]. Furthermore, in nucleate boiling, the bubble departure diameter is closely related to the bubble departure frequency. In general, the bubble departure frequency is inversely proportional to the bubble departure diameter at certain heat flux value [23]. Consequently, increasing flow velocity would directly decrease the bubble departure diameter and increase the bubble departure frequency. Increasing flow velocity in liquid pool also enhances the liquid convection and reduces the thermal boundary layer thickness. This may result in the delay of onset of nucleate boiling. It required higher heated surface temperature to start bubble nucleation [1]. For a pool boiling system with forced convection, it can be found that the critical heat flux, the natural convection regime and the film boiling regime would be shifted upward in the boiling curve. However, in the nucleate boiling regime, the enhancement is relatively small compared to other regimes. Some correlations have been proposed to account for the forced convection effect in pool boiling. Bergles and Rohsenow [24] recommended that the following correlation could be used to estimate the heat transfer at low wall superheat region:

$$q" = q"_{fc}\sqrt{1+\frac{q"_{pb}}{q"_{fc}}\left(1-\frac{q"_{i}}{q"_{pb}}\right)^{2}} \tag{2.12}$$

Where $q"_{fc}$ is the single phase liquid forced convection heat flux specified at the wall temperature, $q"_{pb}$ is the pool boiling heated surface heat flux at actual wall temperature and $q"_{i}$ is the pool boiling heat flux at the threshold superheat, where the nucleated boiling begins. Yilmaz et al. [25] conducted an experiment of Freon-113 boiling around the round horizontal copper tube at atmospheric pressure. They found that increasing velocity always resulted in an improvement in heat transfer. Furthermore, the peak heat flux is proportional to the square root of the liquid velocity when the vapor Weber number is in the range between 15 and 200.

2.1.3.6 Gravity

The gravitational condition may change the bubble departure mechanism. Siegel and Keshock [26] investigated the nucleate boiling bubble dynamic with saturated distilled water in gravity fields from 1.4 to 100% of Earth's gravity. It was found that the departure bubbles became larger and the growth times longer in reducing gravity fields. However, in Merte's [27] investigation, the increasing of the gravity field only slightly enhanced the low heat flux region. The influence of the gravity field on the nucleate boiling regime was found to be small.

2.1.3.7 System pressure

The system pressure would influence the pool boiling heat transfer performance. According to Dhir's [10] review of boiling heat transfer, increasing system pressure resulted in incipience superheat decrease, and the boiling curve would be shifted to the left. Rainey et al. [28] studied the effect of pressure on FC-72 pool boiling using a square pin-finned surface. They found that the nucleate boiling performance was enhanced by increasing pressure condition, which was consistent with Dhir's review. Further, they also stated that the critical heat flux also increased with pressure.

2.1.3.8 Heat flux and superheat

Heat flux and the wall or surface superheat temperature are the two main independent variables of concern in most boiling experiments. Increasing heat flux or superheat results in increased energy transfer into the working fluid. By plotting the heat flux versus the wall superheat, the boiling curve shown in section 2.1.1 can be generated and analyzed. Changing heat flux or superheat would take the system into different boiling regimes and change the primary boiling heat transfer mechanisms. Research to date has shown that the active nucleation site density on the heating surface increases as the wall heat flux or superheat increases [10]. The bubble departure frequency at each nucleation site also increases [1]. Increasing heat flux or superheat also results in a larger bubble departure diameter [20, 21].

2.2 Forced convection boiling

In forced convection boiling, the flow motion is related to the fluid bulk motion and the buoyancy force from the bubble formation and departure. The forced convection boiling mechanisms strongly depend on the geometry of the heater. It can be categorized into two main groups: external flow boiling and internal flow boiling [29].

2.2.1 External flow boiling

The external flow boiling generally is related to the boiling performance that the liquid fluid is forced to flow through heater surface. It would improve the heat transfer coefficient in the single-phase convection regime and significantly increase the critical heat flux. For the subcooled flow or the low quality flow, equation 2.12 listed in previous sections can be used to estimate the total external flow boiling heat flux [24]. In order to estimate the maximum heat flux, Lienhard and Eichhorn [30] have developed the following correlation for the cross-flow over a cylinder.

For the high cross-flow velocity:

$$\frac{q''_{max}}{\rho_l u_\infty h_{lv}} = \frac{1}{\pi}\left[\frac{1}{169}\left(\frac{\rho_v}{\rho_l}\right)^{\frac{1}{4}} + \frac{1}{19.2}\left(\frac{\rho_v}{\rho_l}\right)^{\frac{1}{6}}\left(\frac{\sigma}{\rho_l u_\infty^2 d}\right)^{\frac{1}{3}}\right] \tag{2.13}$$

For the low cross-flow velocity:

$$\frac{q''_{max}}{\rho_l u_\infty h_{lv}} = \frac{1}{\pi}\left[\left(\frac{\rho_v}{\rho_l}\right) + (4)^{\frac{1}{3}}\left(\frac{\rho_v}{\rho_l}\right)^{\frac{2}{3}}\left(\frac{\sigma}{\rho_l u_\infty^2 d}\right)^{\frac{1}{3}}\right] \tag{2.14}$$

Where u_∞ is the cross-flow velocity and d is the cylinder diameter.

The high and low velocity regime can be specified by:

$$\text{Low Velocity: } u_\infty \leq \frac{\pi q''_{max}}{\rho_v h_{lv}\left[0.275\left(\frac{\rho_l}{\rho_v}\right)^{\frac{1}{2}}+1\right]} \qquad (2.15)$$

$$\text{High Velocity: } u_\infty > \frac{\pi q''_{max}}{\rho_v h_{lv}\left[0.275\left(\frac{\rho_l}{\rho_v}\right)^{\frac{1}{2}}+1\right]}$$

2.2.2 Internal flow boiling

The internal flow boiling is closely related to the liquid-vapor two-phase flow inside a heated tube. It is one of the most complex boiling phenomena found in many applications. The internal flow boiling heat transfer has a strong dependence on the two-phase flow quality, the mean flow velocity, the tube diameter, the tube orientation, the heat flux input and the heated surface temperature. The two-phase flow quality or dryness fraction is defined by:

$$\text{x} = \frac{\dot{m}_v}{\dot{m}} \qquad (2.16)$$

Where $\dot{m}_v$ is the mass flow rate of vapor and $\dot{m}$ is the total mass flow rate equal to the liquid mass flow rate plus the vapor mass flow rate.

The two-phase flow behavior during internal flow boiling can be described by the flow regime plot in Figure 3

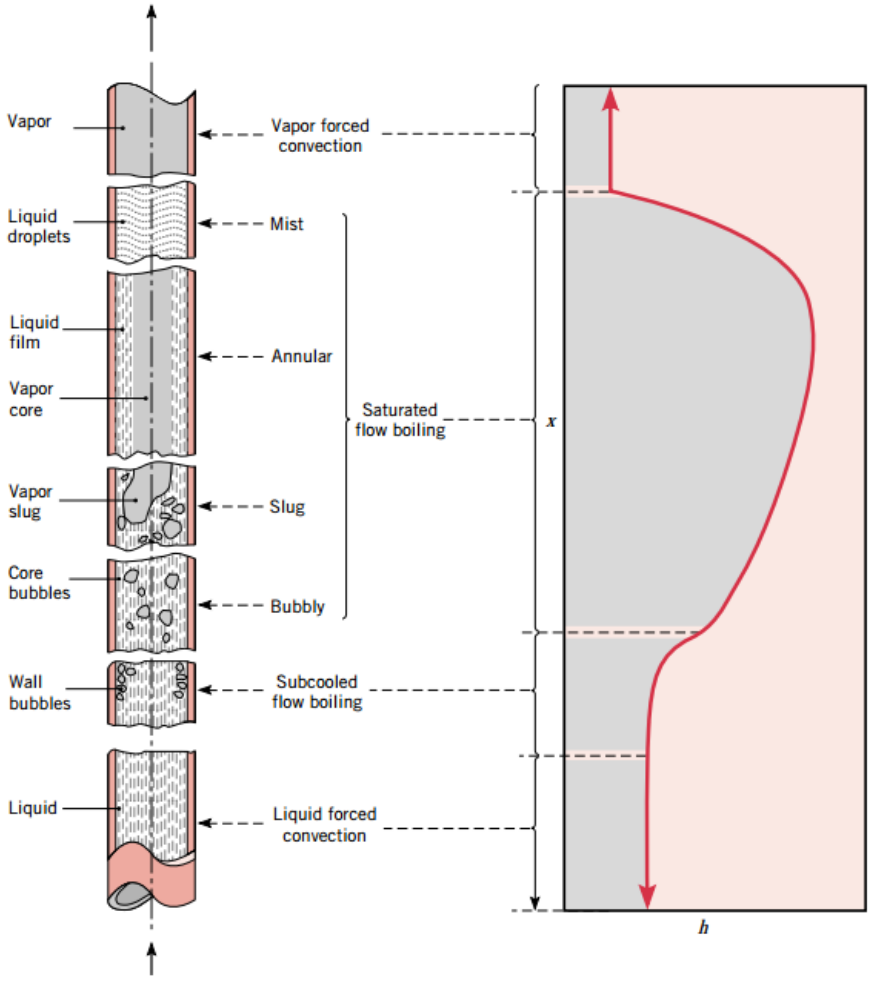

Figure 3. Flow regimes for forced convection boiling in vertical tube [29]

In general, the flow development in the vertical heated tube with constant heat flux input can be separated into several regimes. When the subcooled liquid enters the heated zone, the single phase liquid forced convection regime starts. The fluid constantly receives heat from the tube and the temperature of the fluid increases. When the surface temperature of the heated tube exceeds the liquid saturation temperature, the bubble is

generated at the heated surface. This region is named subcooled flow boiling region because the liquid at the center of tube is still subcooled. The temperature changes significantly along the tube radial direction in this region. Once the entire liquid flow reaches the saturation temperature, the bubbles can exist at any radial location inside the tube. Then, the saturated flow boiling regime begins. The two-phase flow quality increases with the liquid flow down the tube. The first regime in the saturated flow boiling is the bubbly regime. Small bubbles can be found in this regime. As the quality increases, the small bubbles coalesce and form bubble slugs. Further increasing the quality would drive the flow regime into the annular flow regime, where the bubbles occupy the center of the tube and form thin liquid film on the tube wall. The evaporation at this liquid film is so effective that it becomes the dominant heat transfer mechanism. The highest heat transfer coefficient can be found in this regime. One thing need to be noticed is that the vapor column and the liquid film would move at different velocities in this regime. The vapor has a larger velocity compared to the liquid film. Further down the tube, the dry spots appear on the tube surface. When the entire tube inner surface is dried, the remaining liquid would form droplets at the center of the tube. This regime is named the mist regime. If the droplets eventually vaporized, the superheated vapor occupies the entire tube, and then the vapor forced convection regime starts. In this regime, the heat transfer coefficient is the smallest because of the low thermal conductivity of vapor.

Because of the high thermal heat transfer efficiency in saturated flow boiling regime, several correlations have been proposed. Kandlikar's [31] correlation seems to

be one of the most reliable correlations for saturated flow boiling. This correlation can be applied to both vertical tubes and horizontal tubes. The form of Kandlikar's correlation is listed below:

For nucleate boiling dominant regime

$$\frac{h_{NBD}}{h_{lo}} = 0.6683\left(\frac{\rho_l}{\rho_v}\right)^{0.1} x^{0.16}(1-x)^{0.64} f_2(Fr_l) + 1058Bo^{0.7}F_{fl}(1-x)^{0.8} \tag{2.17}$$

For convective boiling dominant regime

$$\frac{h_{CBD}}{h_{lo}} = 1.136\left(\frac{\rho_l}{\rho_v}\right)^{0.45} x^{0.72}(1-x)^{0.08} f_2(Fr_l) + 667.2Bo^{0.7}F_{fl}(1-x)^{0.8} \tag{2.18}$$

$$\frac{h_{TP}}{h_{lo}} = \text{maximum value of equation of (2.17) or (2.18)} \tag{2.19}$$

Where h_{TP} is heat transfer coefficient during two-phase flow, x is quality, Fr_l is Froude number with all flow as liquid, F_{fl} is fluid-dependent parameter and $f_2(Fr_l)$ is given by following equation:

$$f_2(Fr_l) = \begin{cases} (25Fr_l)^{0.3} & (\text{for } \mathrm{Fr_l} < 0.04, \text{horizontal tube}) \\ 1 & (\text{for } \mathrm{Fr_l} > 0.04, \text{horizontal and vertical tube}) \end{cases} \tag{2.20}$$

The single-phase heat transfer coefficient with total flow as liquid, h_{lo}, can be calculated using the Petukhov et al.[32] and Gnielinski [33] correlations to achieve a better estimation of two-phase flow heat transfer coefficient.

2.3 Enhancement of pool boiling heat transfer

Although the normal pool boiling process already has high heat transfer coefficient, researchers continue to investigate pool boiling enhancement techniques. Bergles [34] summarized the pool boiling enhancement techniques and categorized it into three main groups: passive techniques, active techniques and compound enhancement. For the passive techniques, they do not require an external power input. However, the active techniques do require an external activator or a power supply to achieve enhancement. If two or more techniques are used at the same time to produce enhancement, it is called compound enhancement. According to Bergles's review, the passive techniques for pool boiling included treated surface, rough surface, extended surface, displacement enhancement devices, surface tension devices and additives for fluid. Active techniques included mechanical aids, surface vibration, fluid vibration, electrostatic field and jet impingement. The enhancement technique used in this project is categorized as a displaced enhancement device, which enhances pool boiling performance by creating a confined space. This section will focus on this category.

Yao et al. [35] investigated the confined pool boiling of Freon-113 in vertical narrow annuli with closed bottom. They found that at the same heat flux, the wall superheat reduced as gap size decreased. The boiling curve would be shifted to the left. The mean heat transfer coefficient increased when the gap size decreased. However, the

critical heat flux value decreased at the same time. Zhao et al. [36] also studied the enhancement of pool boiling in confined space, which consisted of two horizontal surfaces, the lower heated surface and an upper mesh screen. The working fluid was water. It was reported that the boiling heat transfer characteristic was significantly improved when using a mesh screen. The enhancement depended on the mesh sizes and the space gaps. Further, different from a non-hole plate, mesh screen enhanced the whole nucleate boiling curve. Because the mesh screen allowed vapor bubbles to form and coalesce within the confined space in the low heat flux region which allow bubbles to escape from the confined space in high heat flux region. Rops et al. [37] investigated the effects of pool diameter on the pool boiling heat transfer performance. They created a confined space by changing the pool boiling pot diameter from 15 to 4.5 mm. The enhancement of pool boiling heat transfer was found and explained by fluid motion. The unconfined pool boiling flow motion was driven by the chaotic and random motion of bubbles within the confined space. Misale et al. [38] reported that in confined pool boiling, the enhancement of heat transfer at low wall superheat was closely related to the Bond number, which is the ratio of the gap size and the nominal bubble departure diameter. When the Bond number was lower than one, the heat transfer coefficient increased as the confined space decreased. However, the heat transfer efficiency and the critical heat flux decreased drastically as the confined space decreased at high heat flux region. Hsu [39] performed a confined pool boiling test of HFE-7100 with a single orifice horizontal confined plate placed above the heated surface. Hsu [39] considered the effects of orifice diameter and the confined space gap distance on the nucleate pool

boiling heat transfer performance. It was concluded that the smaller orifice size and gap distance provided better heat transfer efficiency at low heat flux region. Further, the larger orifice size with the smaller gap size can provided slightly enhancement at entire boiling curve. The enhancement of pool boiling can be attributed to induce shear flow caused by departure of coalesced bubbles through orifice.

There are many techniques that can be used to improve confined pool boiling heat transfer efficiency. However, the mechanisms of the confined pool boiling enhancement are still not fully understood. Further research into the factors that influence confined pool boiling process is required in order to efficiently utilize it.

3. EXPERIMENTAL FACILITIES AND METHODS

3.1 Experimental facilities

The experimental facilities can be classified into two groups: pool boiling test setup and pump assisted test setup. Both of them were built to achieve the stated research objectives. In this section, the descriptions of the setups used in the research are introduced.

3.1.1 Pool boiling test setup

The scheme and photo of pool boiling test setup is shown in Figures 4 and 5. The setup includes six main parts: the testing chamber, the confined structures, the ITO heating element, the high speed camera and infrared camera, the data acquisition system, the power supply and the chiller. The description of the experimental setup is included in this section.

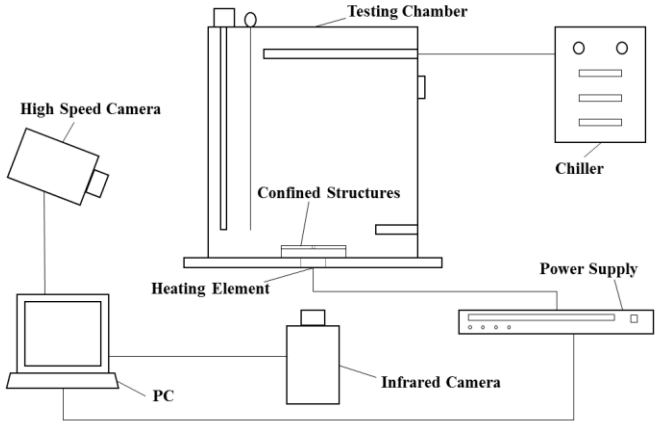

Figure 4. Scheme of the pool boiling test setup

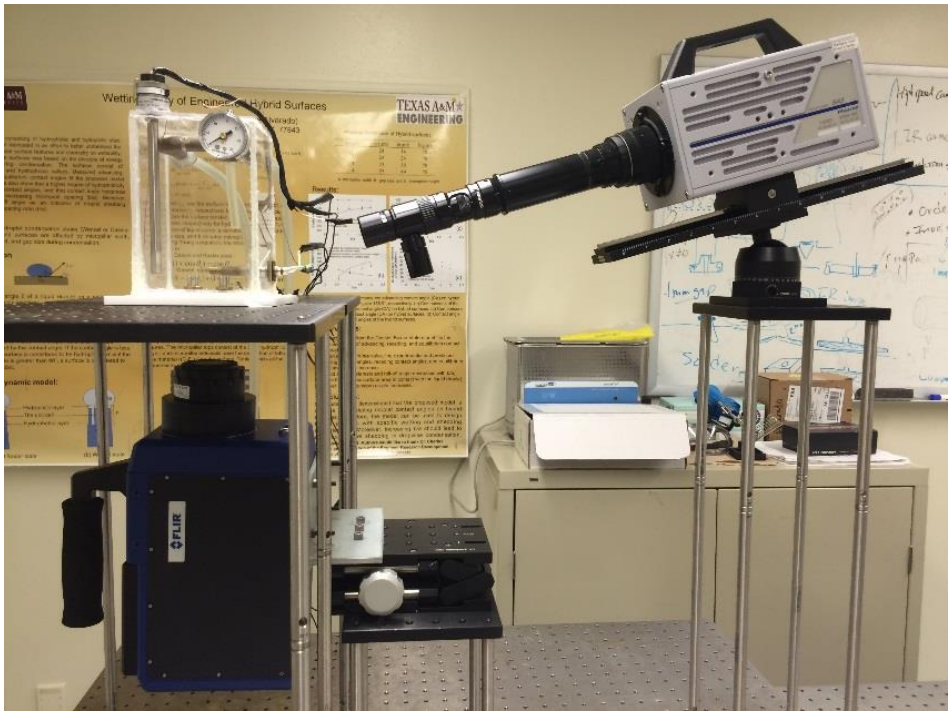

Figure 5. Actual the pool boiling test setup

3.1.1.1 Working fluid

The 3M^{TM}Novec^{TM} Engineered Fluid HFE-7100, methoxy-nonafluorbutane ($C_4F_9OCH_3$), was chosen as working fluid in this research study. Because of its low boiling point, chemical compatibility and low toxicity, HFE-7100 is an ideal working fluid for the pool boiling testing. Further, the appearance of HFE-7100 is clear and colorless, which allows for complete observation of the pool boiling process. The properties table of HFE-7100 is listed in Table 1.

Boiling point (°C)	61
Freeze point (°C)	-135
Liquid density (g/ml) @25 °C	1.52
Vapor density (g/ml) @100 °C	1.31
Heat of vaporization (kJ/kg)	111.6
Liquid thermal conductivity (W/m-K) @25 °C	0.069
Liquid specific heat (J/kg- °C) @25 °C	1183

Table 1. HFE-7100 properties table

3.1.1.2 Testing chamber

The testing chamber was designed to conduct pool boiling tests. The testing chamber walls were made of transparent acrylic. The testing chamber is shown in Figures 6 and 7. It consists of eight components: a cartridge heater, a temperature switch, a thermocouple, a pressure gauge, a condenser, a sample holder, a confined structure and a heating element. The cartridge heater was used to preheat the HFE-7100 pool to its saturation temperature before each test. The temperature switch was used to control the cartridge heater. It would turn off the cartridge heater when the liquid reach the saturation temperature, which kept the system at the desired temperature. The thermocouple was used to double check if the liquid remained at saturation temperature. The pressure gauge was attached to the chamber wall and used to monitor the chamber pressure. The condenser, which was a U shape copper tube was used to condense vapor

and maintain the constant pressure inside testing chamber. The testing chamber pressure was kept at atmospheric pressure during all the tests.

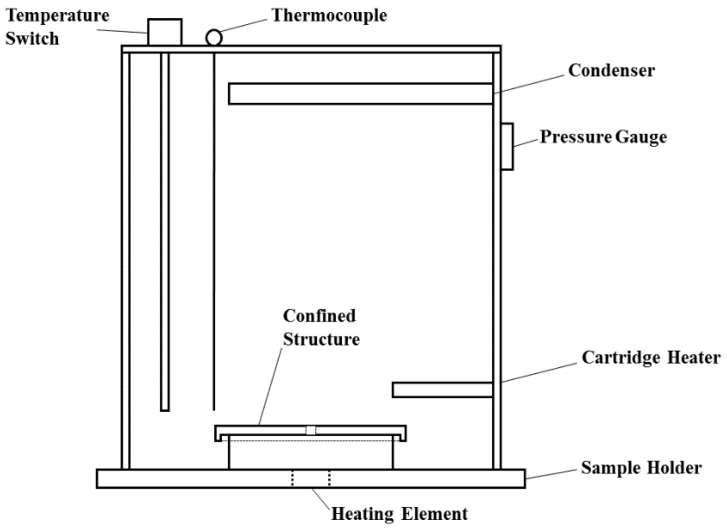

Figure 6. Scheme of testing chamber

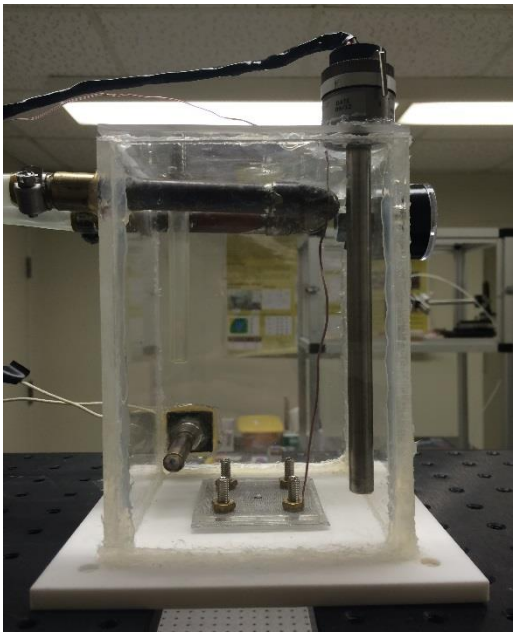

Figure 7. Actual of testing chamber

The sample holder was designed and fabricated by Hsu [39]. It was made of Teflon and used to hold the heating element and confined structures. The design drawing of sample holder is shown in Figure 8. The heating element was attached to the center of the sample holder by using adiabatic epoxy. Screws and washers were used to secure the confined structure at the desired position. In this research, the distance between confined structures was 2.3 mm, which was maintained by using four washers, as shown in Figures 9 through 11 (see below).

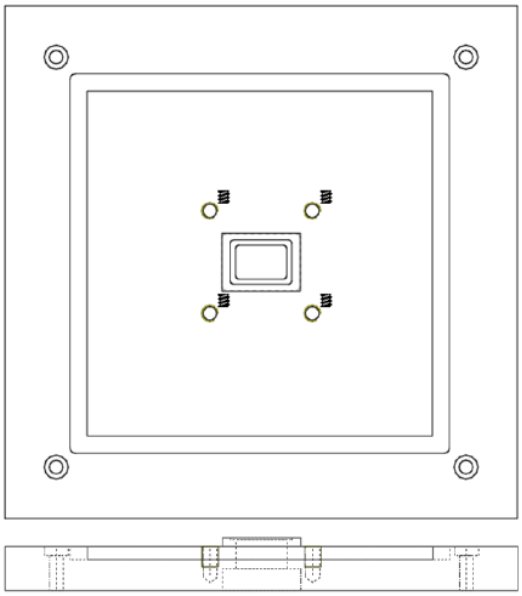

Figure 8. Design drawing of sample holder [39]

3.1.1.3 Confined structures

The confined structures used in this research included three main components: the confined plate with a central orifice, the flanges and the mesh with a central orifice. The scheme and the photos of the confined structure are shown in Figures 9, 10 and 11.

In this research, the gap distance between the confined plate and the sample holder was maintained at 2.3 mm using nuts and washers. The 1-mm flanges were attached to the sides of confined plate as shown in Figure 7. Both the confined plates and flange structures were made of acrylic plates. The mesh was held by the bottom of flanges and washers, which results in a 1.3 mm gap between the mesh and the heated surface.

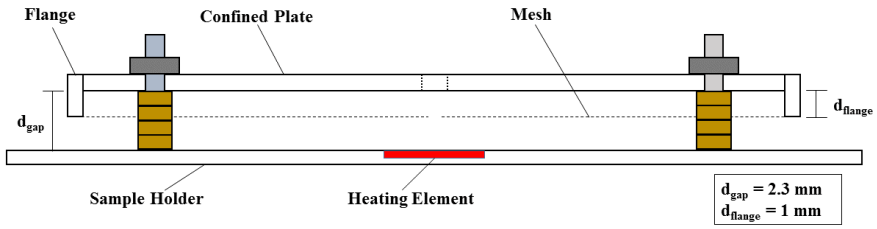

Figure 9. Scheme of confined structures

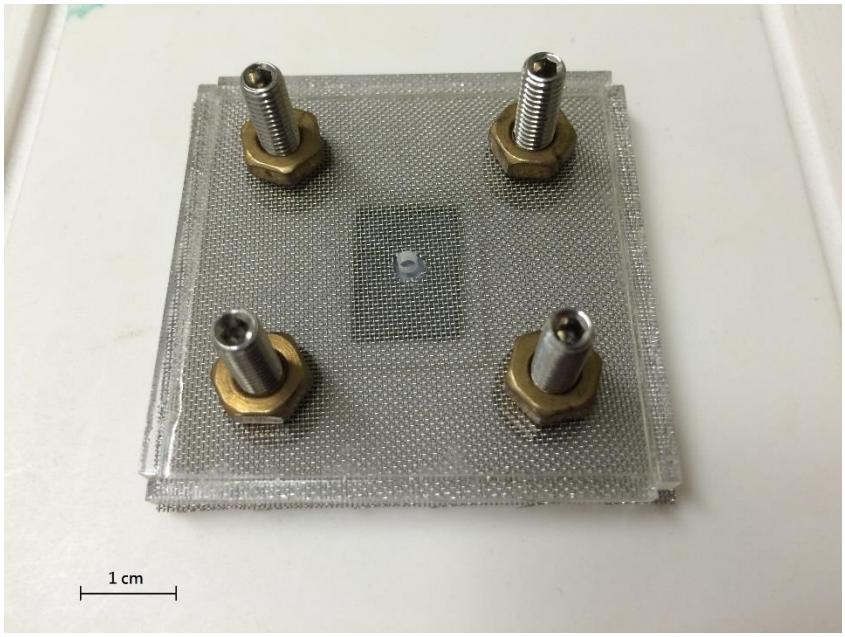

Figure 10. Top view photo of confined structures

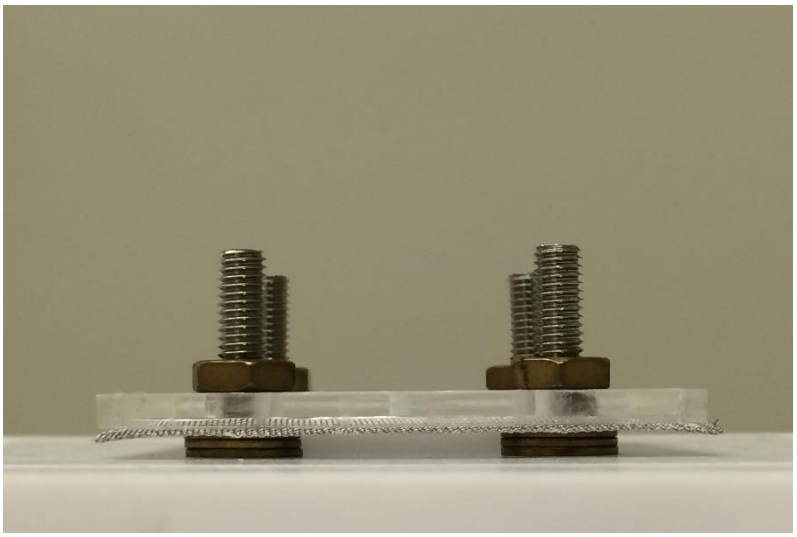

Figure 11. Side view photo of confined structures

The properties of mesh are listed in Table 2. The diameter of confined plate orifice, the flange existence and the diameter of mesh orifice were the variables in this research. Two different diameters of confined plate orifice were used including 2 mm and 4 mm together with three different diameters of mesh orifice including 2.5 mm, 3.5 mm and 4.5 mm.

Mesh material	Aluminum 5056
Mesh size	50 X 50
Opening size (mm)	0.279
Open area percentage (%)	30
Wire diameter (mm)	0.229

Table 2. Mesh properties

3.1.1.4 Heating element

The heating element used in this research was made of a thin film of Indium-Tin-Oxide (ITO), which was deposited on a silicon wafer substrate. The thickness of ITO was about 100 nm and the silicon wafer thickness was 500 μm. The properties of silicon wafer can be found in Table 3. The silicon wafer was used as substrate because of its high thermal conductivity, which can provide uniform temperature distribution. The heating element setup is shown in Figure 12. Hsu [39] measured the emissivity of the heating element to be 0.4 ± 0.022. The uncertainty of the emissivity measurement was about 5.5%.

In order to avoid the roughness effect of ITO coating surface, the ITO coating surface was designed to face downward and be isolated from liquid pool. The heating element was attached to the sample holder by using adiabatic epoxy. Two copper foils were connected to the ITO coating surface by using electrically conductive epoxy as power supply wires. The capillary length (L_c) of HFE-7100 was 0.88 mm. The heating element dimensions were 17 X 12 mm^2, which were at least 14 times the capillary length of liquid. Furthermore, due to the fragility of silicon wafer, the heating element size used in this research was sufficient small to avoid breakage due to the weight of the liquid inside the testing chamber.

Density (g/ml)	2.33
Melting point (^{o}C)	1414
Specific heat (J/g-^{o}C)	0.7
Thermal conductivity (W/m-K)	148
Thermal diffusivity (m^2/s)	8×10^{-5}

Table 3. Properties of silicon wafer

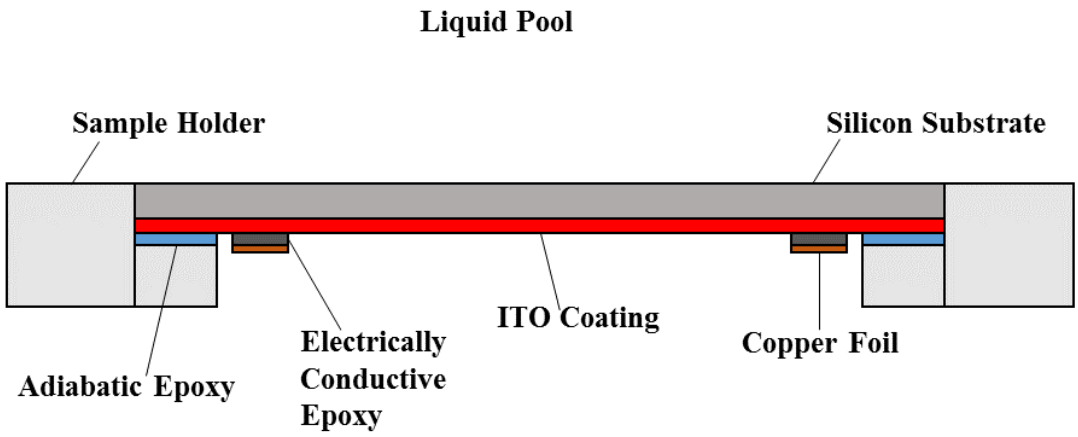

Figure 12. Scheme of heating element setup

3.1.1.5 Data acquisition system

The data acquisition system used in the pool boiling tests included two components: the infrared camera and high speed camera. The infrared camera was used to record the heating element surface temperature distributions. The infrared camera focused on the ITO coating surface, recording videos from the bottom of the heated surface. The high speed camera was used to acquire bubbles motion videos, which focused on the confined plate orifice. The videos were taken from the side wall of the

testing chamber. Similar data acquisition system and techniques were also used in several recent studies [40-46].

3.1.1.5.1 Infrared camera

A FLIR SC7650E infrared camera with 50 mm MW lens (L0106) and two extension rings (12 mm, 20 mm) was used in this research to acquire the temperature profile of the heating element surface. With the indium antimonide (InSb) type sensor, a IR wavelength between 1.5 and 5.1 µm can be captured by camera. The full resolution of infrared camera was 640 x 512 pixels and the maximum frame rate was 300 frame per second. In this research, the 60 Hz frame capture rate and 640 x 512 resolution were selected. The infrared camera control software, ExaminIR, was used to record the temperature distribution on the heater surface. By specifying the emissivity of the heated surface, frame rate and resolution, the average surface temperature can be obtained. Furthermore, the spatial and temporal standard deviations of surface temperature can also be found using ExaminIR.

3.1.1.5.2 High speed camera

A Photron FASTCAM SA3 high speed camera with a high resolution lens (Zoom 6000 series, Navitar) was used to record two-phase flow videos. The 1024 x 1024 pixels resolution and 1000 Hz frame rate were used in this research. The high speed camera control software, Photron FASTCAM Viewer (PSV), was used to record the video by setting the resolution, frame rate and shutter speed.

3.1.1.6 Power supply

The Lambda TDK GEN600-2.6, programmable DC power supply was used in the study. The power supply was connected to the heating element to provide the required power. The voltage output range was 0 to 600 Volt and the current output range was 0 to 2.6 A. The power supply was controlled by using a computer with the Hyperterminal version 5.1 software.

3.1.1.7 Chiller

The Thermo Scientific NESLAB Merlin M25 chiller was used in the study. The temperature range of the chiller was between -15 and 35 °C. The chiller was connected to the condenser tube, which maintained a condenser temperature of 20 °C during the tests.

3.1.2 Pump assisted system facilities

The pump assisted system was added to the original pool boiling test facility in order to measure the pressure profile inside confined structures, mass flow rate of fluid and the two-phase flow quality coming through the system. The system includes two different setups: the pressure measurement setup and the flow rate and quality measurement setup. The details of the pump assisted system are introduced in the following sections.

3.1.2.1 Pressure measurement setup

The pressure measurement setup is shown in Figure 13 and 14. The setup includes several components such as the pressure transducer, the pump, the heat exchanger and the syringe and valves and the tube system. The components are shown and described below.

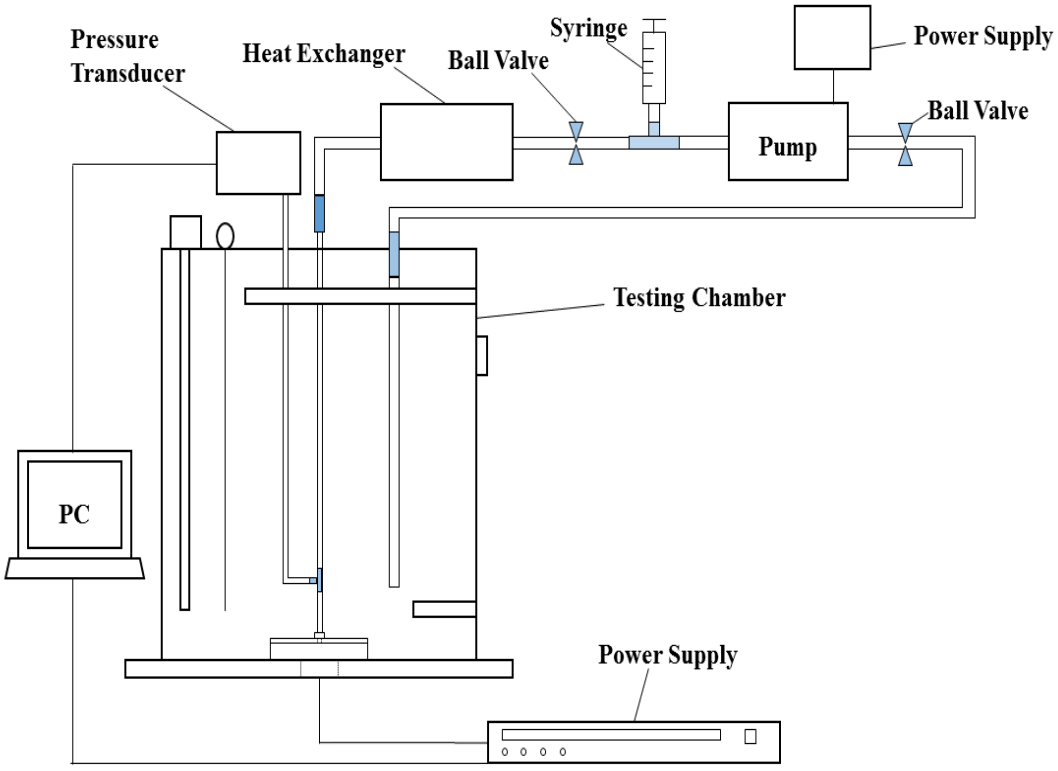

Figure 13. Scheme of pressure measurement pump assisted system

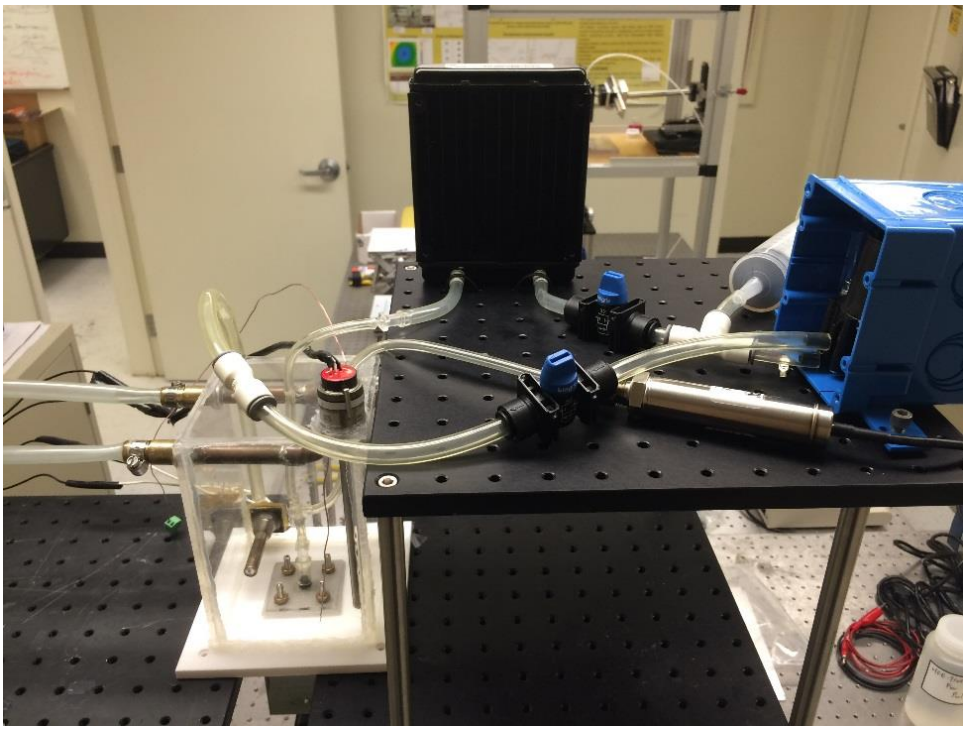

Figure 14. Actual pressure measurement pump assisted system

3.1.2.1.1 Pressure transducer

In this study, the Omega PX409-030AUSBH, absolute pressure transducer was used. The transducer was attached to the tube near the confined plate orifice. It can provide an estimation of pressure inside the confined structures. The pressure transducer can provide ± 0.08% BSL accuracy. It was directly connected to the computer through USB port. The Omega Digital Transducer Application software was used to acquire pressure data.

3.1.2.1.2 Pump

The ZC-A250 mini brushless magnetic self-priming hot water pump was used in this research. The pump was installed in a plastic box to hold it in position during tests. A cushion was attached to the bottom of the pump to minimize the vibration. During the pump assisted tests, the pump power input was set at 0.44 Watt, which was the minimum power input for the pump. It was relatively low compared to the heating element power input. The pump was maintained at a constant working speed during the experiment.

3.1.2.1.3 Heat exchanger

The heat exchanger was directly cooled by the surrounding air. It was used to condense the vapor in the two-phase flow to maintain constant working speed of the pump. Furthermore, the mass flow rate measurement would be easier if the vapor was condensed.

3.1.2.1.4 Syringe and valves

The syringe and valves were used in this study to assist the fluid circulation initiation. The tube system was filled with liquid before tests started by using syringe and valves. It was used to prime the suction side of the system to ensure that enough liquid could enter the pump. After circulation was initiated, the valves remained open and the syringe was emptied and held at the same position.

3.1.2.1.5 Tube system

Two different sizes of tubes were used in the study. The smaller tube was used to be able to visualize bubbles flowing through the system before reaching the condenser. Larger tubing was also used to minimize pressure drop throughout the system. The dimensions of the small tube were 6.35 mm for outer diameter and 3.18 mm for inner diameter. The dimensions of the larger tube dimensions were 9.53 mm for outer diameter and 6.35 mm for inner diameter. Both of the tubes were made of polyurethane and the tube walls were transparent.

3.1.2.2 Flow rate and quality measurement setup

The scheme and photos of the flow rate and quality measurement setup are shown in Figures 15, 16 and 17. The basic setup was similar to the pressure measurement system. The pressure transducer was removed from the system and a tube with mark and the flow rate measurement tools were attached to it.

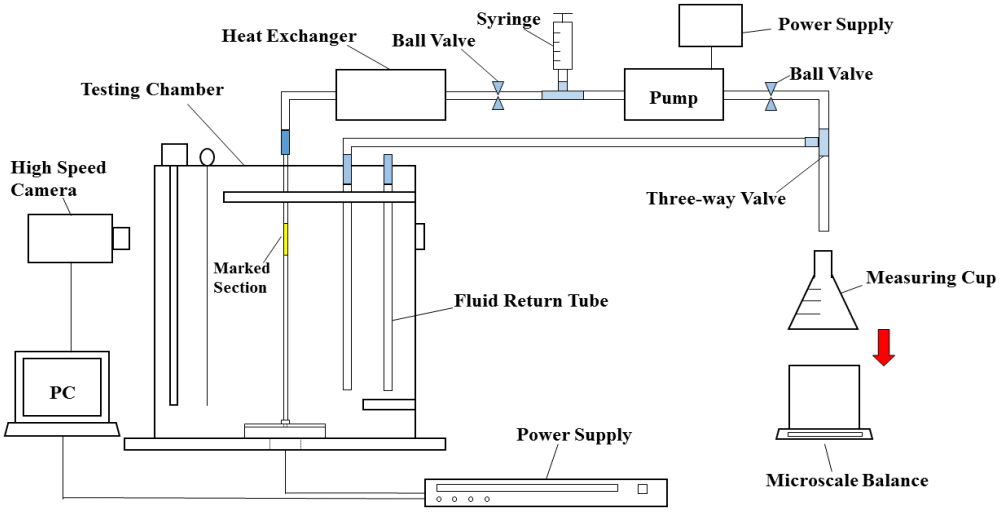

Figure 15. Scheme of flow rate and quality measurement pump assisted system

Figure 16. Side view of flow rate and quality measurement pump assisted system

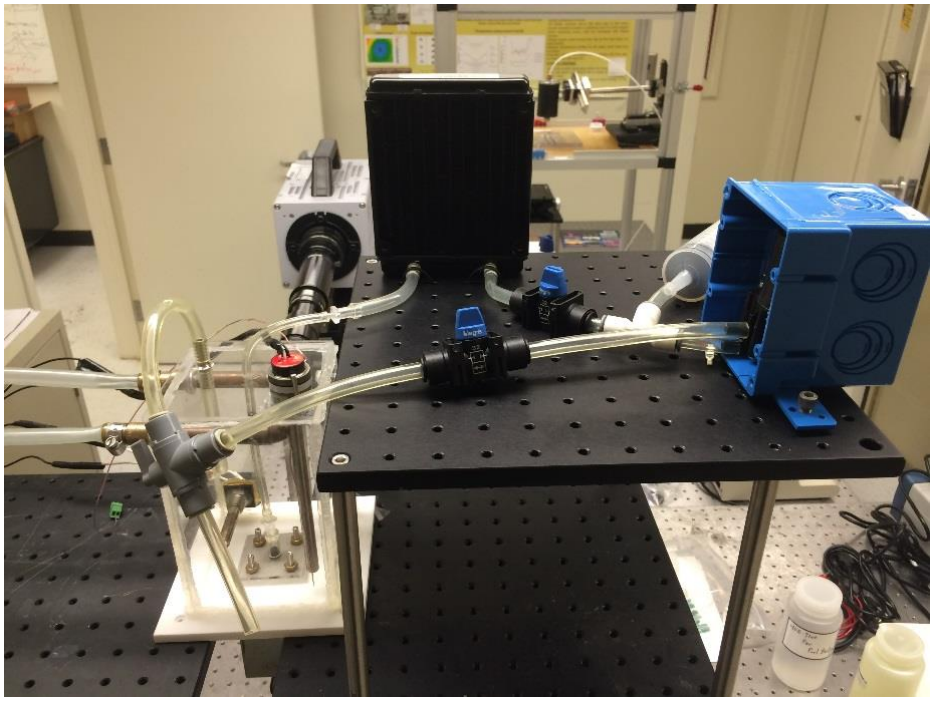

Figure 17. Top view of flow rate and quality measurement pump assisted system

3.1.2.2.1 Tube with scale mark

The tube with scale mark was used in the study to determine two-phase flow quality measurement. The photo of the tube is shown in Figure 18. The tube was transparent and the dimensions of the tube were 6.35 mm for outer diameter and 3.18 mm for inner diameter. The marked section was 2 cm long. The high speed camera was focused on the marked section and the estimation of the vapor mass flow rate was conducted in this section.

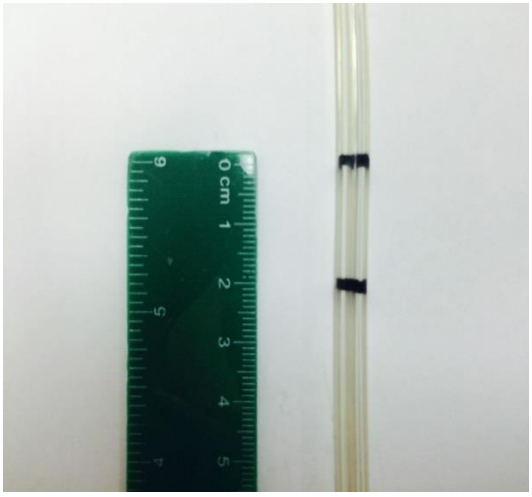

Figure 18. Tube with marked section

3.1.2.2.2 Flow rate measurement tools

The flow rate measurement tools included a three-way valve, a measuring cup with cap, a micro scale balance and a fluid return tube. The three-way valve was used to adjust the direction of the liquid flow. During the flow rate measurement phase, the three-way valve was turned to direct the fluid flow into the measuring cup. After measurement was done, the three-way valve was turned back to the original position,

maintaining the fluid circulation through the system. The measuring cup with cap was used to measure mass flow rate using a micro-scale balance. The cap was used to avoid liquid evaporation. The Denver Instrument APX-200 balance was used to measure mass flow rate of fluid. The accuracy of the balance was ± 0.2 mg. After the weight measurement, the liquid was returned to the testing chamber through the fluid return tube.

3.2 Experimental methods

The experimental procedures and the methods used are described in this section including the heat loss measurement procedure, the pool boiling test procedure, the pressure test procedure, the quality test procedure, and uncertainty analysis.

3.2.1 Heat loss measurement

Heat conduction through the sample holder and the convection through the air were two main factors that caused the heat loss from the testing chamber during pool boiling experiments. The test was conducted without working fluid in order to estimate the total heat loss from the testing chamber. The heating element power input was controlled by the power supply. The low power input of the heating element was maintained in order to avoid equipment damage. The surface temperature of the heating element was recorded using the infrared camera when the system reached steady state. The surrounding temperature was also recorded. The power input of the heating element

was considered as the heat loss in this test. The relation between the heat loss and the temperature difference between heat element surface and surrounding air is shown in Figure 19.

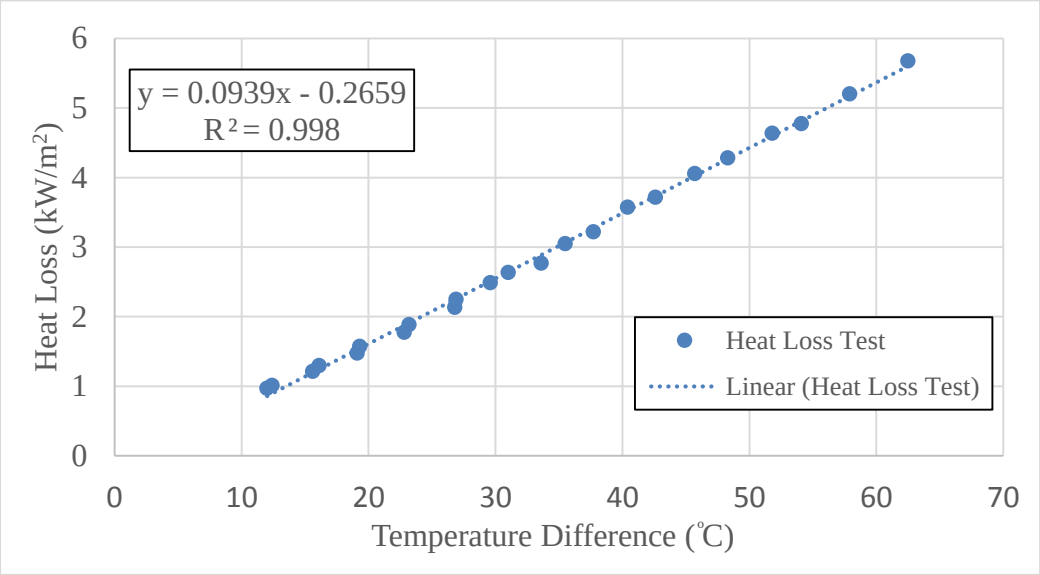

Figure 19. Estimation of heat loss corresponding to temperature difference

3.2.2 Pool boiling test procedure

Prior to running pool boiling tests, the heating element was cleaned by using methanol. The testing chamber was filled with HFE-7100 until it reached the 50 mm liquid level. Afterward, the testing chamber was sealed. The cartridge heater (pre-heater) was then started to heat the working fluid to its saturation temperature for 30 minutes to make sure the system was saturated and the working fluid was degassed. Then, the power supply was used to power the heating element by adjusting its voltage. In order to avoid the pool boiling hysteresis effect, the fluid was first heated to nearly the critical

heat flux point. However, it was not allowed to exceed the critical heat flux in order to avoid any damage to the heating element. When the pool boiling test started, the voltage input of the heating element was decreased in small steps. The heat flux input from the heating element to the working fluid was calculated by the power supply power input, the heat loss taking into account the area of the heating element. The following equation was used to determine effective heat flux:

$$q'' = \frac{Q_{in} - Q_{loss}}{A} \tag{3.1}$$

The heating element surface temperature profile was recorded by the infrared camera when the system reached steady state. Further, the high speed videos were also acquired by the high speed camera in order to observe the motion of bubbles.

3.2.3 Pressure test procedure

The pressure test procedure was similar to the pool boiling tests. Before the test started, the heating element was cleaned and the liquid pool was preheated to its saturation temperature. The heat flux input from the heating element was also increased to the value which was close to the critical heat flux point. During the test, the heat flux input was gradually decreased by controlling the power supply. When the system reached steady state, the heat flux transferred from the heating element to the liquid was recorded. The pressure transducer also started to record the pressure

data for 10 seconds. The average pressure was then used to determine the pressure condition at the given heat flux input.

3.2.4 Quality test procedure

The quality test followed the same preparation procedure as the pool boiling test. The quality test included two parts: the total mass flow rate measurement and the vapor mass flow rate estimation. In the total mass flow rate measurement, the three-way valve was manually opened to direct the liquid into the measuring cup for 30 seconds. Then, the total fluid weight would be measured by the balance. By knowing the fluid weight and the time interval, the total mass flow rate can be calculated. The entire total mass flow rate measurement was repeated six times. The average total mass flow rate was then calculated from the measured data.

In the vapor mass flow rate estimation, high speed images of the flowing bubbles were captured by focusing the high speed camera on the marked section. The two-phase flow motions of bubbles inside the marked section would be captured by the high speed camera. In the determination of vapor quality, two typical bubble shapes were considered and found using high speed images, including the round or spherical bubble and the column or cylindrical bubble. Assuming that the round bubble and column bubble were perfectly spherical and cylindrical, respectively, the volume of vapor could be estimated. The vapor volume was estimated by measuring the corresponding bubble volume using ImageJ software. The software was used to measure the radius of the round bubbles and the radius and the height of the column bubbles. The vapor volume flow rate was estimated by taking into account the volume of each image bubble, and the

corresponding time interval. The time interval between two successive bubble images was 100 ms. In total, fifteen images were used to determine vapor quality. With the vapor volume flow rate, vapor density and the total mass flow rate, the approximate quality of the two-phase flow can be found by using Equation 3.2, as follows:

$$\text{Quality } (\%) = \frac{Vapor\ volume\ flow\ rate \times Vapor\ density}{Total\ mass\ flow\ rate} \times 100\% \tag{3.2}$$

3.2.5 Uncertainty analysis

The uncertainty analysis method was used in this study based on the Kline-McClintock methodology [47]. The uncertainty analysis equations are shown below:

$$\mathrm{R} = \mathrm{R}(v_1, v_2, \dots\dots, v_n) \tag{3.3}$$

$$w_R = \left[\sum_{i=1}^{n}\left(\frac{\partial R}{\partial v_i} w_i\right)^2\right]^{\frac{1}{2}} \tag{3.4}$$

Where *R* is the function with n independent variables, $v_1, v_2, \dots\dots, v_n$ are the independent variables, w_i is the uncertainty interval for each variables, w_R is the uncertainty of function *R*. More detail of uncertainty analysis of measurement can be found in the appendix A.

4. RESULT AND DISCUSSION

The experimental observations including the confined pool boiling heat transfer performance, the pressure inside the confined structures and the two-phase flow quality estimation are presented in this section. Firstly, the measurement of the unconfined pool boiling curve, which is used as the reference line is presented. Secondly, the results of the pool boiling heat transfer performance when using flange structures are presented and discussed. Thirdly, the effects of the mesh orifice size (2.5, 3.5 and 4.5 mm diameter) on the pool boiling heat transfer are shown and discussed as well. Then, the effects of the plate orifice size (2 and 4 mm diameter) on the pool boiling heat transfer are presented. Finally, the results of the pump assisted test are shown and discussed. The bubble motion images when using confined structures pool boiling tests are also included in this section in order to clearly explain how the confined structures influence bubble motions and enhance the pool boiling heat transfer.

4.1 Unconfined pool boiling

The unconfined pool boiling curve was obtained and used as the reference line in this research. The average heating element surface temperature and the input heat flux were measured at the same time in order to obtain the boiling curve. The average heating element surface temperature was acquired by using the IR images as described in the previous chapter. The spatial standard deviation of the surface temperature ranged between 0.5 and 0.7 $^{\circ}$C, which indicates that the unconfined pool boiling process was

relatively homogenous compared to the confined pool boiling due to the bubble formation mechanism. The standard deviation of the temperature measurement was less than 0.4 ˚C for each point, which was about 2% in error. The input heat flux was calculated by using Equation 3.1. The uncertainty of heat flux measurement was about 1.8%, which is shown in Appendix A. The small errors in surface temperature and input heat flux measurement indicate that the experiments were reproducible. The unconfined pool boiling curve is shown in Figure 20. Furthermore, the bubble images during the unconfined boiling process are shown in Figure 21.

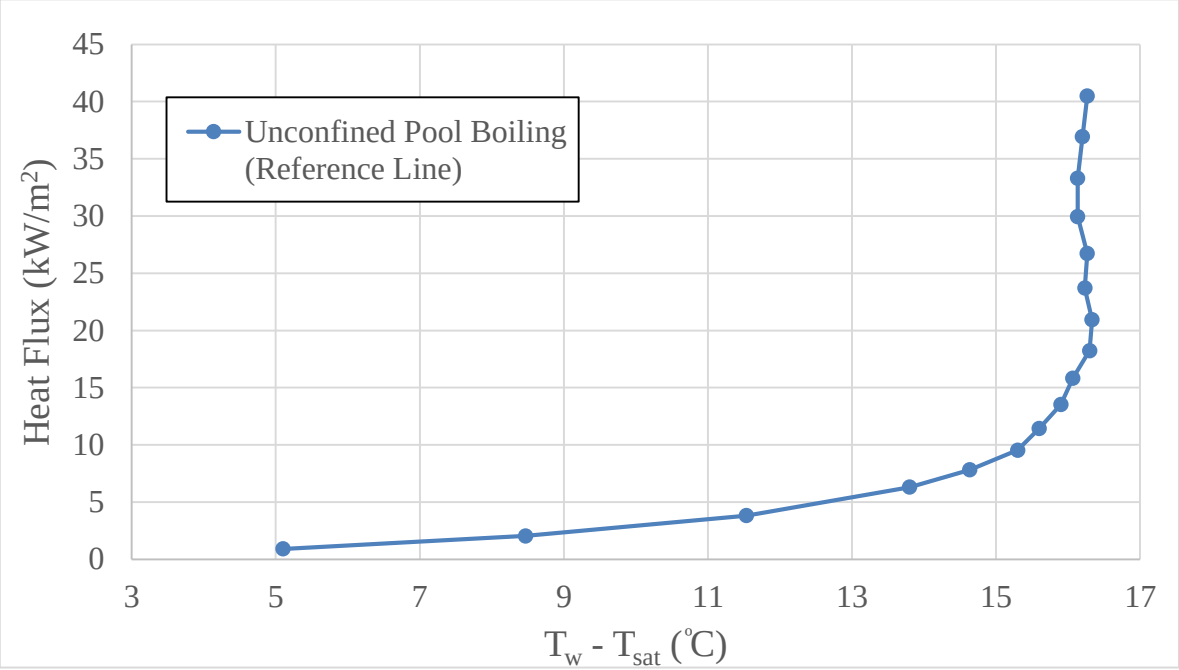

Figure 20. Unconfined pool boiling curve for HFE-7100

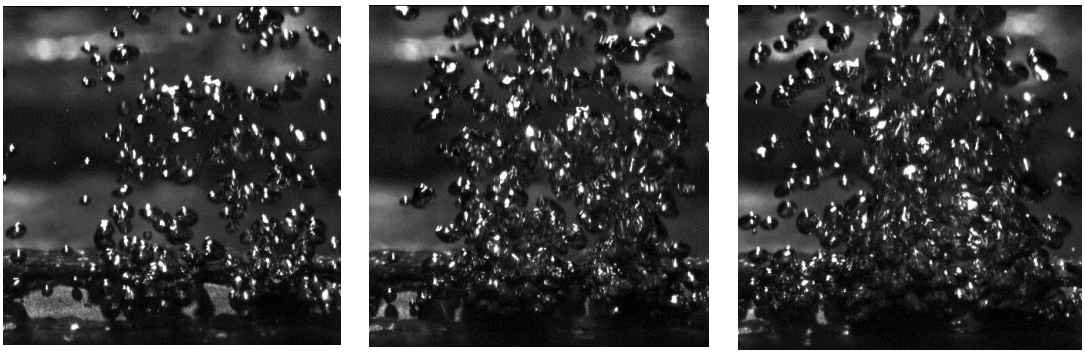

(a) (b) (c)

Figure 21. Bubble images during unconfined pool boiling process at (a) 13.5 kW/m2 (b) 23.5 kW/m^2 (c) 30 kW/m^2 for HFE-7100

4.2 Confined structures pool boiling

The boiling mechanism in confined structures was different from that in the unconfined pool boiling. Pool boiling with confined structures had a higher spatial standard deviation across the heating element in terms of surface temperature compared to unconfined pool boiling (0.6 ~ 1.2 $^{\circ}$C). This may be attributed to the coalescences of bubbles inside the confined space. Furthermore, the confined spaces led to the formation of coalesced bubble-induced shear flow which would bring single phase fluid in the space, resulting in a significant temperature variation along the surface [36]. Specifically, the induced shear flow would remove the superheated layer near the heating surface, which in turn leads to heating surface temperature variations. Consequently, higher spatial standard deviations of surface temperature were observed. More details about these observations are discussed in the following sections

Reference Cases	
Case A	Unconfined Pool Boiling
Case B	2 mm Hole Plate, No Flanges
Case C	4 mm Hole Plate, No Flanges

Table 4. Reference cases

		Plate Orifice Size	
		2 mm	4 mm
Mesh Orifice Size	No Mesh	Case D	Case E
	2.5 mm	Case F	Case G
	3.5 mm	Case H	Case I
	4.5 mm	Case J	Case K

Table 5. Experimental cases with the use of flanges

4.2.1 Effect of flange structures on pool boiling heat transfer

The effect of flange structures on pool boiling heat transfer process was investigated by comparing the boiling curves with the unconfined pool boiling case (Case A) and the confined structure pool boiling without flanges cases (Case B and C). Figures 22 and 23 show the boiling curve when using different plate orifice diameters (2 mm and 4 mm).The standard deviation values of the heating element surface temperature in repeated experiments were less than 0.7 $^{\circ}$C (less than 4% error) in the entire confined structures pool boiling tests. The boiling curves with error bars for confined structures pool boiling tests can be found in Appendix B.

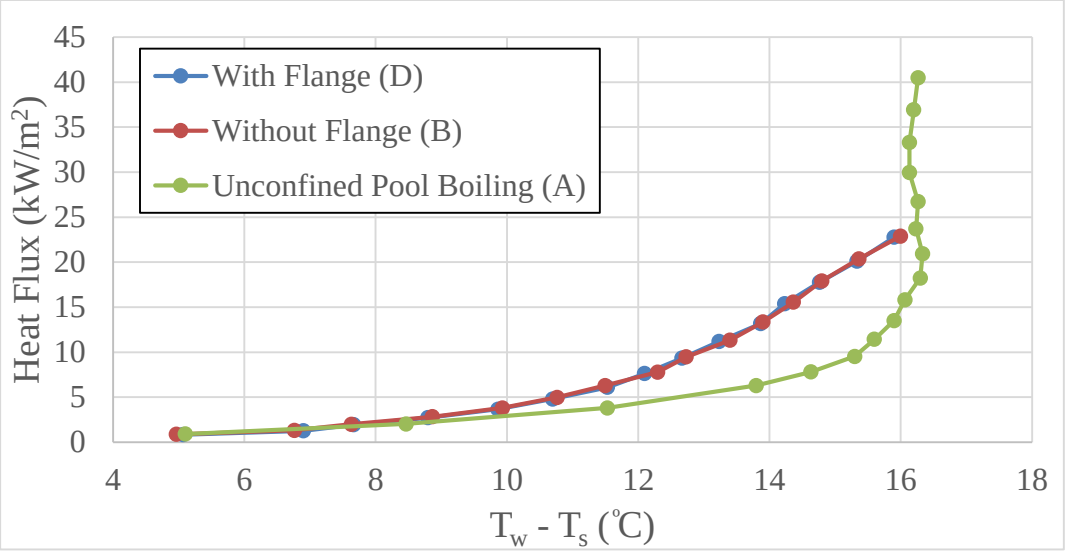

Figure 22. Boiling curves of different confined structures with 2 mm orifice plate

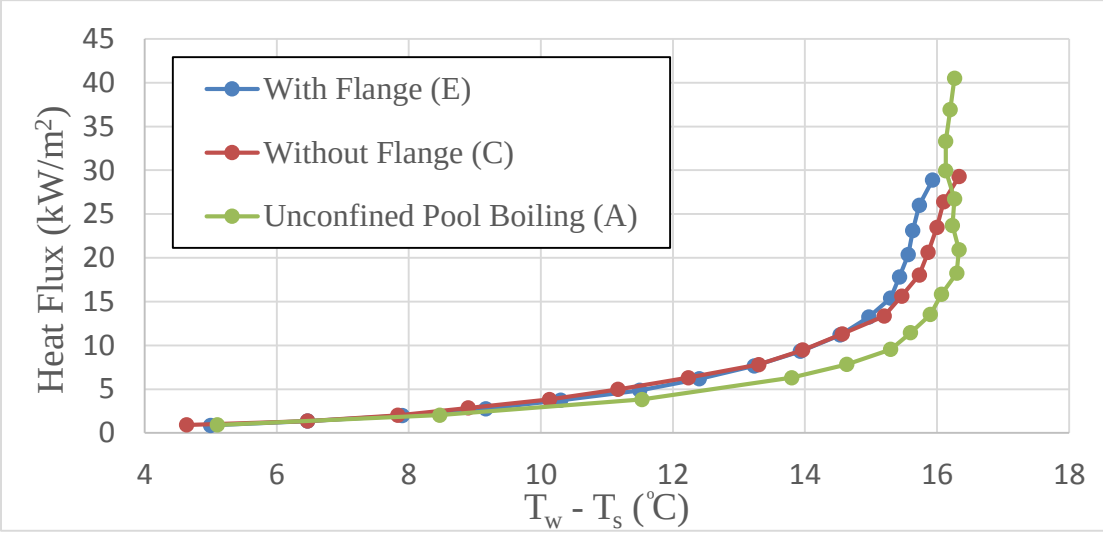

Figure 23. Boiling curves of different confined structures with 4 mm orifice plate

It can be seen from Figure 22 that the flange structure has no effect on pool boiling heat transfer when using a 2 mm orifice plate. The boiling curve of case D was nearly identical to case B. The enhancement of pool boiling only came from the confined

plate. When using a 4 mm orifice confined plate, the flange led to a slight enhancement within the high heat flux region. The surface temperature reduction at high heat flux region compared to case C (without flange) was only 0.4 °C. Although the flanges structure can avoid bubbles from escaping through the sides of the confined plate, the flange structure would not provide a significant change on the pool boiling heat transfer.

4.2.2 Effect of the mesh orifice diameter on pool boiling heat transfer

The effect of the mesh orifice diameter on the pool boiling heat transfer was also studied by comparing the boiling curves with the reference case (Case A). Figures 24 and 25 show the boiling curves when different mesh orifice diameters (2.5, 3.5 and 4.5 mm) were used with single orifice flanged plates.

For the cases of 2 mm plate hole diameter (cases F, H, and J) shown in Figure 24, the optimum heat transfer performance was achieved by using the smallest mesh orifice size (2.5 mm diameter). The boiling curve for case F depicts a 0.7 to 3.1 °C reduction of heated surface temperature during the test. The boiling curve in case H (3.5 mm mesh orifice) is characterized by a relatively small temperature reduction of about 0.5 to 2.4 °C compared to case F. However, when using the largest mesh orifice size (case J: 4.5 mm mesh orifice), the surface temperature reduction was worse when compared to case F and case H in low and moderate heat flux regions. The boiling curve of case J in Figure 22 shows a 0.5 ~ 1.6 °C surface temperature reduction.

For the cases of 4 mm plate hole diameter (case G, I, and K) shown in Figure 25, the smallest mesh orifice size (case G: 2.5 mm mesh orifice) can still provide the largest

surface temperature reduction. A 0.4 ~ 2.5 ℃ of temperature reduction can be found in case G. However, in cases I and K, the improvements of pool boiling heat transfer were relatively small compared to other cases. For cases I and K, the surface temperature reductions were about 0.2 ~ 1.5 ℃.

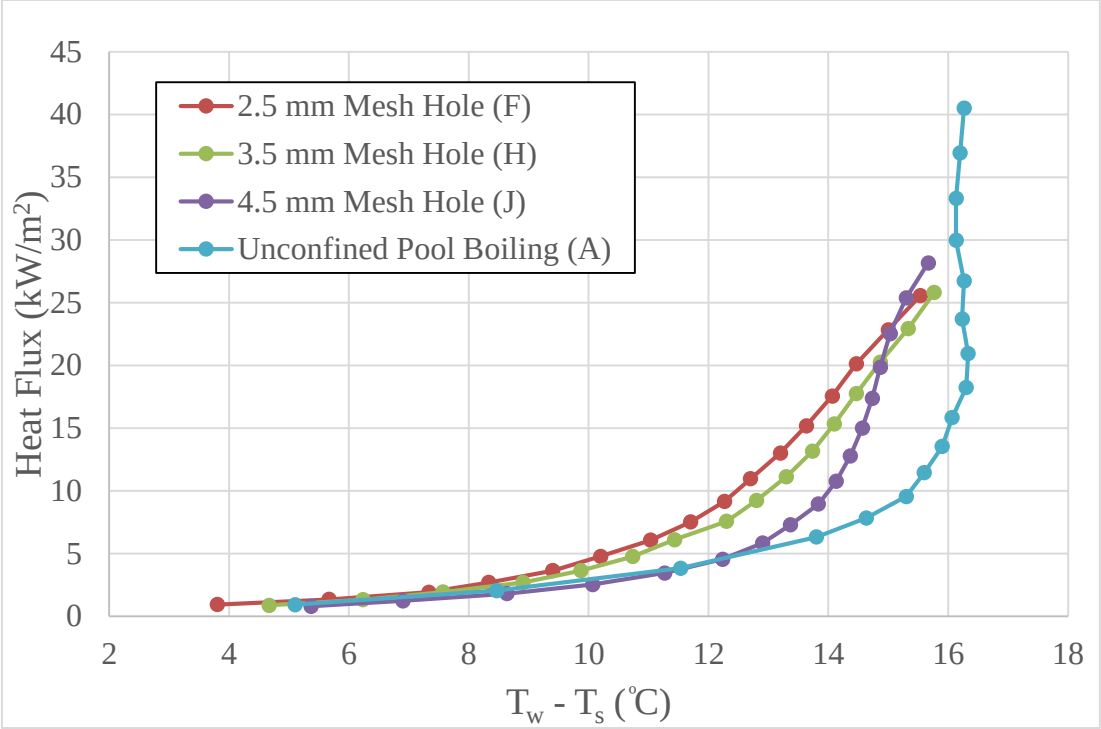

Figure 24. Mesh orifice size effect on boiling curves when using 2 mm hole flanged plate

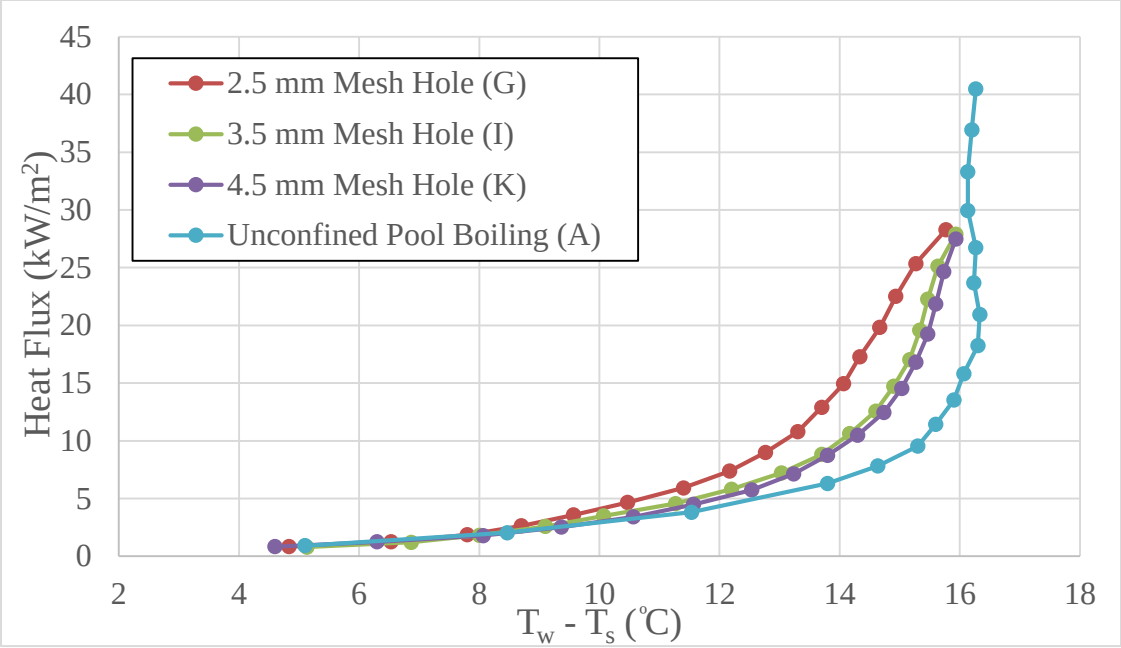

Figure 25. Mesh orifice size effect on boiling curves when using 4 mm hole flanged plate

In order to achieve a better comparison between among cases, the enhancement percentages of the heat transfer coefficient were calculated using Equations 4.1 and 4.2 and shown in Figures 26 and 27.

$$\mathrm{h} = \frac{q''}{\Delta T} \tag{4.1}$$

$$\text{enhancement (\%)} = \frac{h_c - h_{uc}}{h_{uc}} \times 100\% \tag{4.2}$$

Where the h is the heat transfer coefficient, q'' is the heat flux value, ΔT is the temperature difference between the heating element surface and the liquid saturation temperature, h_c is the heat transfer coefficient of the confined pool boiling and h_{uc} is the

heat transfer coefficient of the unconfined pool boiling. The average uncertainty of the heat transfer coefficient were 4.6%. At the intermediate and high heat flux region, the uncertainty of enhancement percentages were about 6.5%. Therefore, heat transfer enhancement values for heat flux values less than 5 kW/m^2 have been omitted. Consequently, Figures 26 and 27 only show the enhancement percentages for heat flux values greater than 5 kW/m^2.

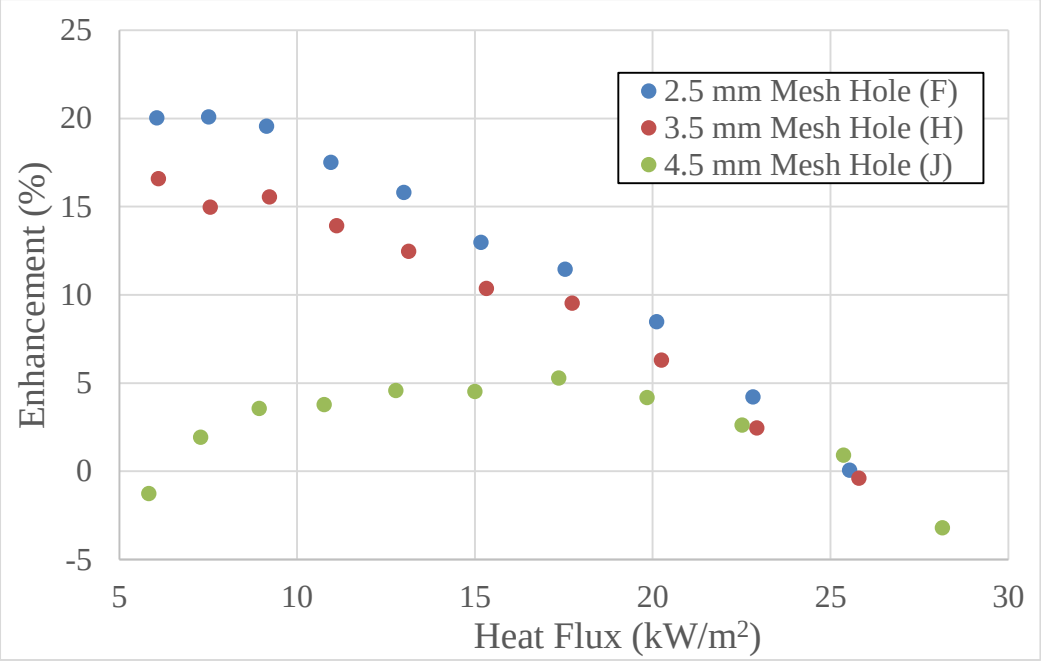

Figure 26. Percentage of enhancement of heat transfer coefficient when using 2 mm hole flanged plate with different mesh orifice size

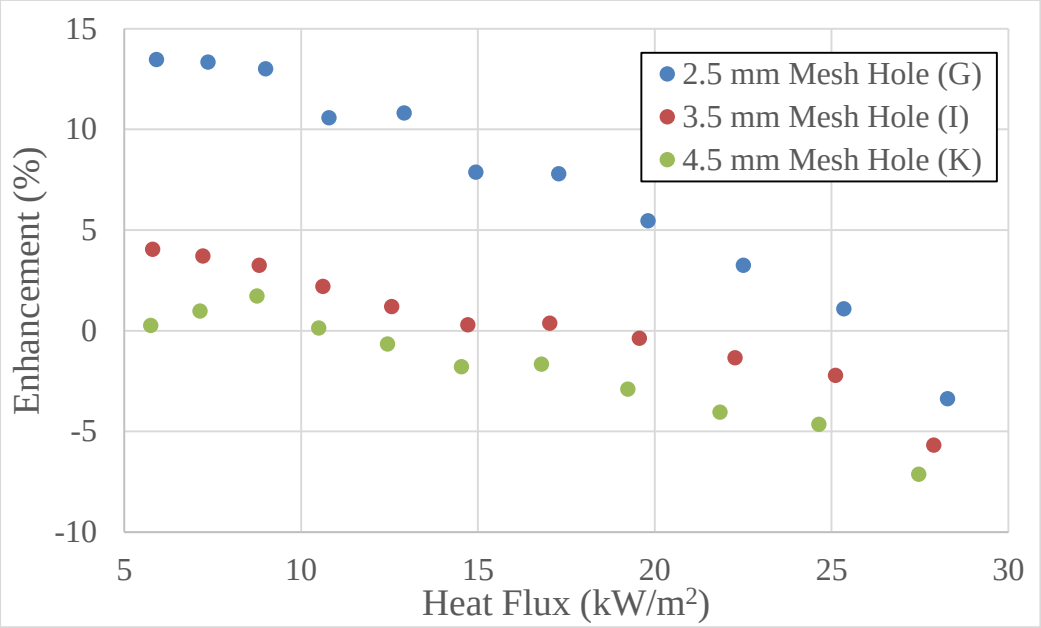

Figure 27. Percentage of enhancement in heat transfer coefficient when using 4 mm hole flanged plate with different mesh orifice size

As seen in Figures 26 and 27, the greatest enhancement of the heat transfer coefficient in confined structures pool boiling tests can be found when the heat flux is between 5 and 10 kW/m^2. This behavior indicates that there is an optimum heat flux input, which can optimize the bubble generation and the departure process. The percentage of enhancement in the heat transfer coefficient gradually decreased between 5 and 25 kW/m^2. This behavior may be related to the increasing number of active nucleation sites as heat flux increases, which leads to a proliferation of bubbles, deactivation of nucleation sites present at low heat flux and the activation of larger nucleation sites at high heat flux [48]. Under those circumstances, bubble departure frequency or bubble departure diameter should increase, which would lead to higher vapor quality (as discussed below). However, the lower level of enhancement at higher

heat flux values suggests that mesh itself becomes a limiting factor in term of heat transfer. Eventually, a significant reduction of the heat transfer coefficient was detected when the heat flux is between 25 and 30 kW/m^2. The reduction of the heat transfer coefficient can be attributed to the partial dry-out or film boiling effect at the heating surface [49]. The vapor film is assumed to have covered the heating surface and deteriorated the heat transfer performance.

From the observation of Figures 24 to 27, the mesh confined structures can always provide reductions on the heating element surface temperature. Furthermore, the heat transfer coefficient would also be enhanced. The amount of the enhancement on the pool boiling heat transfer depends on the size of mesh orifice. The smaller mesh diameter can provide a larger amount of enhancement. The enhanced performance of the pool boiling may be attributed to an induced bubble coalescence process inside the confined space. However, the effects of buoyancy-driven shear flow should also be taken into account as explained below.

The bubble coalescence process does influence the pool boiling heat transfer in two main ways. The first is the direct evaporation from the liquid microlayer under the coalesced bubbles. The micolayer volume would be expanded during bubble coalescence process, as shown in Figure 28. The supplementary microlayer vaporization increases the latent heat transfer and locally reduces the wall temperature [50]. The bubble departure diameter also increases. The second is the induced shear flow caused by the coalesced bubbles departure (buoyancy-driven convection process). The induced shear flow promotes bubble growth and bubble detachment from the nucleation site. Higher

bubble departure frequency should be expected in the presence of induced shear flow [51]. Furthermore, the induced shear flow draws the single-phase liquid into the confined space, thus removing the superheated layer at the heated surface [36]. The regrowth of the superheated layer also enhances the heat transfer process.

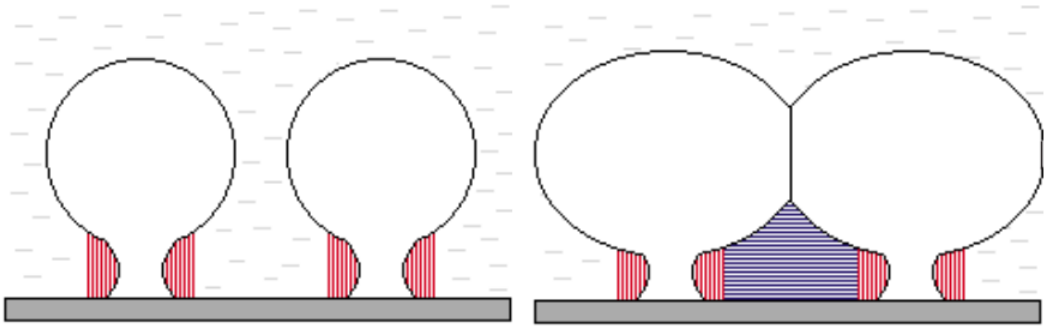

Figure 28. Schematic of the supplementary microlayer [50]

The mesh can provide a restriction on the motion of bubbles, which can force the bubbles to coalesce inside the confined space. During the formation of coalesced bubbles, more liquid would be vaporized and the heat dissipated from the heating element would also be increased. In general, the induced shear flow caused by the coalesced bubbles departure reduces the heated surface temperature and increases the bubble departure frequency. Consequently, the heat transfer coefficient of the confined pool boiling can be enhanced.

4.2.3 Effect of the plate orifice diameter with mesh on pool boiling heat transfer

The effect of the plate orifice diameter on pool boiling heat transfer was also studied by comparing the boiling curves to the reference case. Figures 29, 30 and 31 show the boiling curves comparisons when using different plate orifice sizes with the same mesh hole diameter. The plate orifice diameters were 2 mm and 4 mm. A clear trend was shown in these figures that the smaller plate orifice size can always provide a better enhancement on the pool boiling heat transfer. The 2 mm diameter plate cases (case F, H and J) can provide 0.2 ~ 0.75 °C greater heating element surface temperature reduction in the moderate heat flux region when compared to the 4 mm diameter plate cases. This trend can also be attributed to the higher bubble restriction provided by smaller plate orifice size.

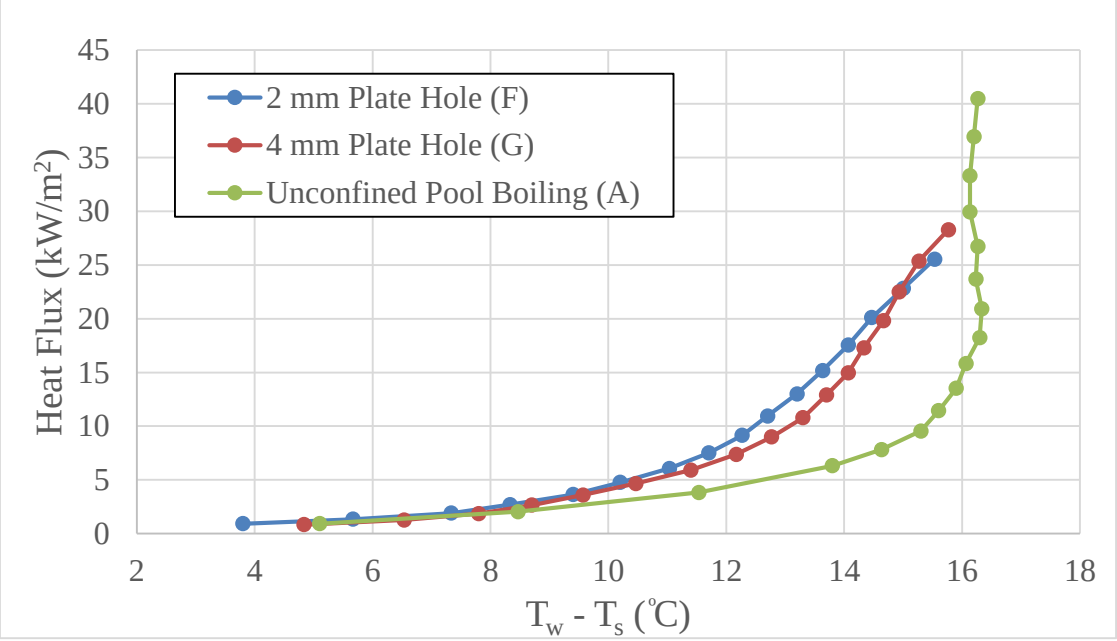

Figure 29. Plate orifice size effects on boiling curves when using 2.5 mm hole mesh

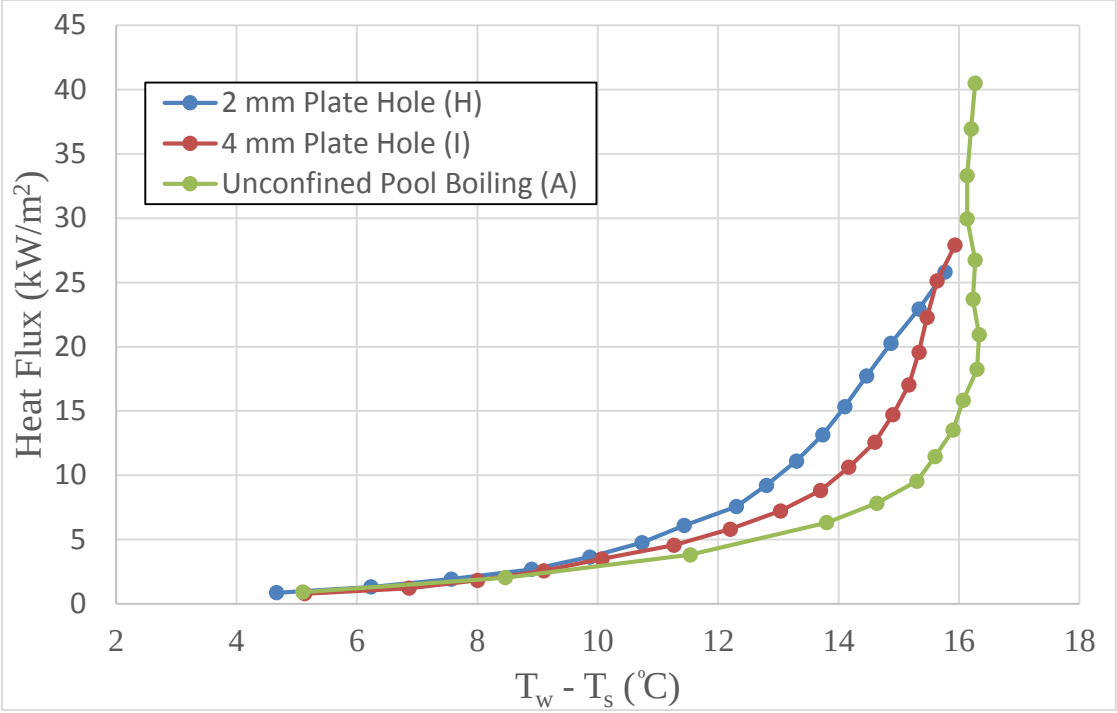

Figure 30. Plate orifice size effects on boiling curves when using 3.5 mm hole mesh

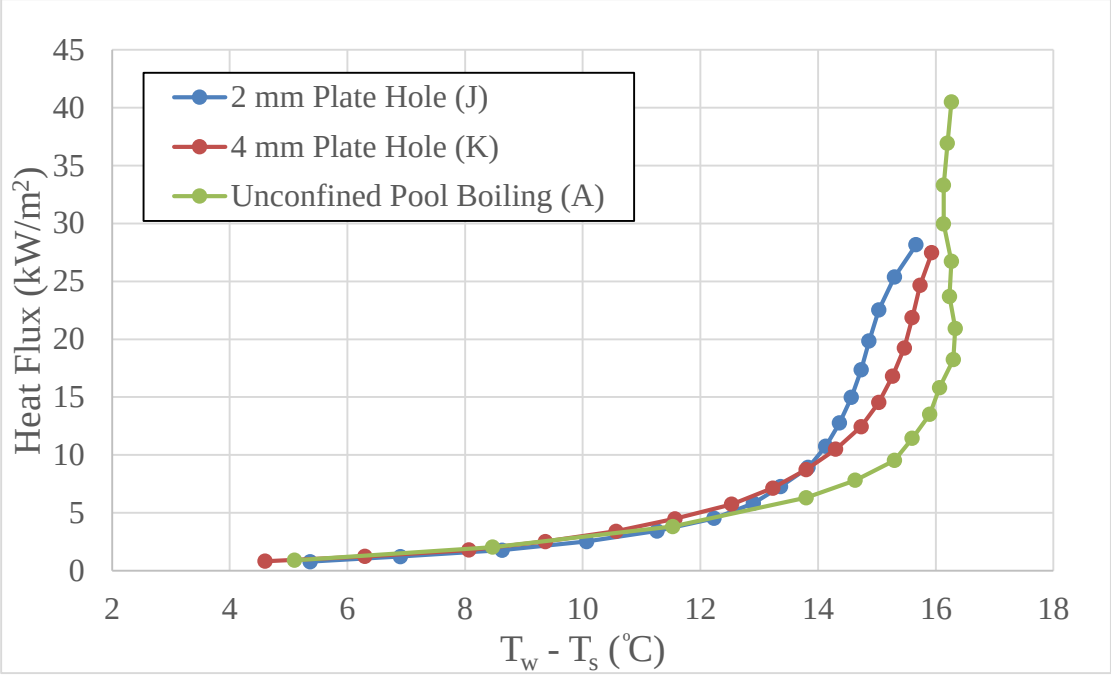

Figure 31. Plate orifice size effects on boiling curves when using 4.5 mm hole mesh

Table 6 summarizes the experimental results when using different plate orifice sizes and mesh orifice sizes. The best performance case was case F, which used the combination of the smallest plate orifice (2 mm) and mesh orifice (2.5 mm). The worst performance case was case K, which was the combination of the largest plate orifice (4 mm) and mesh orifice (4.5 mm). The effect of plate orifice size is noticeable. In summary, the better heat transfer performance takes place when using a 2 mm orifice plate. It can also be found that reducing mesh orifice size can provide a further enhancement on the confined pool boiling. The enhancement from the confined structures can be attributed to the interplay of several mechanisms including induced bubble coalescence, greater nucleation site density, and greater departure diameter and frequency driven by induced shear flow.

		Plate Orifice Size	
		2 mm	4 mm
Mesh Orifice Size	No Mesh	**Case D** ♦ Enhanced in all heat flux region ♦ Temperature reduction: 0.3-2.5 ℃	**Case E** ♦ Enhanced in all heat flux region ♦ Temperature reduction: 0.2-1.4 ℃
	2.5 mm	**Case F** ♦ Best performance case ♦ Enhanced in all heat flux region ♦ Temperature reduction: 0.7-3.1 ℃	**Case G** ♦ Enhanced in all heat flux region ♦ Temperature reduction: 0.4-2.5 ℃
	3.5 mm	**Case H** ♦ Enhanced in all heat flux region ♦ Temperature reduction: 0.5-2.4 ℃	**Case I** ♦ Enhanced in all heat flux region ♦ Temperature reduction: 0.2-1.5 ℃
	4.5 mm	**Case J** ♦ Enhanced in middle and high heat flux region ♦ Temperature reduction: 0.5-1.6 ℃	**Case K** ♦ Worst performance case ♦ Enhanced in all heat flux region ♦ Temperature reduction: 0.2-1.4 ℃

Table 6. Effects of plate and mesh orifice size on confined pool boiling performance with the use of flanges

The effect of different restriction levels on bubble motions can be found in the Figures 32 and 33, which compares the best enhancement case (case F: 2.5 mm mesh hole and 2 mm plate hole) and the worst enhancement case (case K: 4.5 mm mesh hole and 4 mm plate hole). The bubbles in the worst performance case were smaller. In contrast, the bubbles in the best performance case were larger. The observations show that the bubble motions in the best enhancement case (case F: 2.5 mm mesh hole and 2 mm plate hole) were more restrictive. The level of restriction on bubble motions inside the confined space had a positive effect on pool boiling heat transfer performance as explained above.

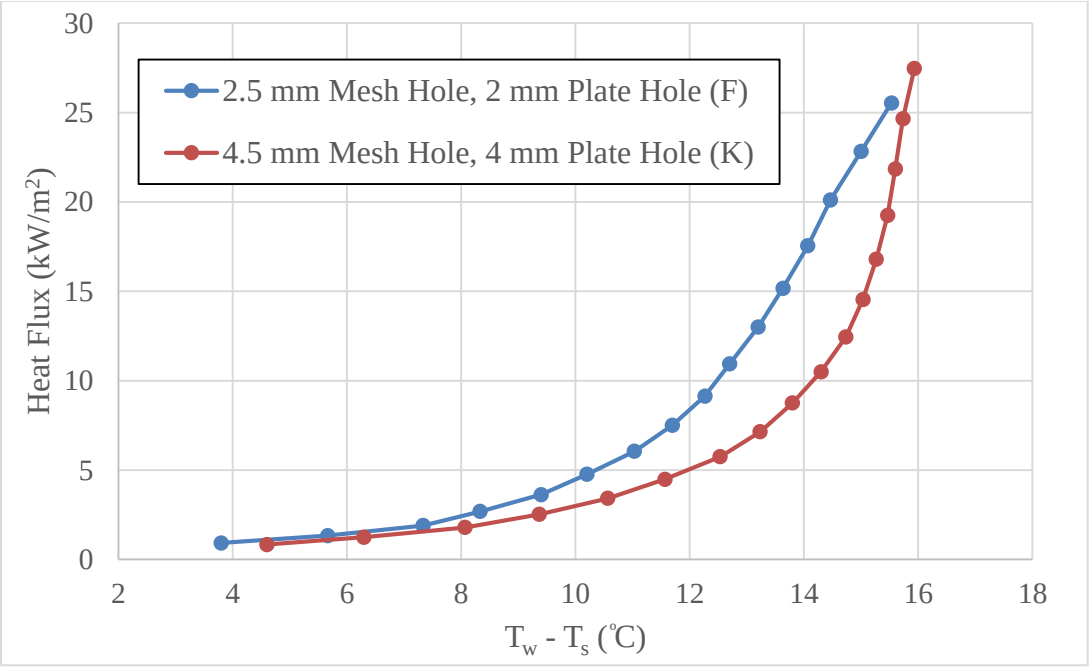

Figure 32. Boiling curves comparison between cases F and K

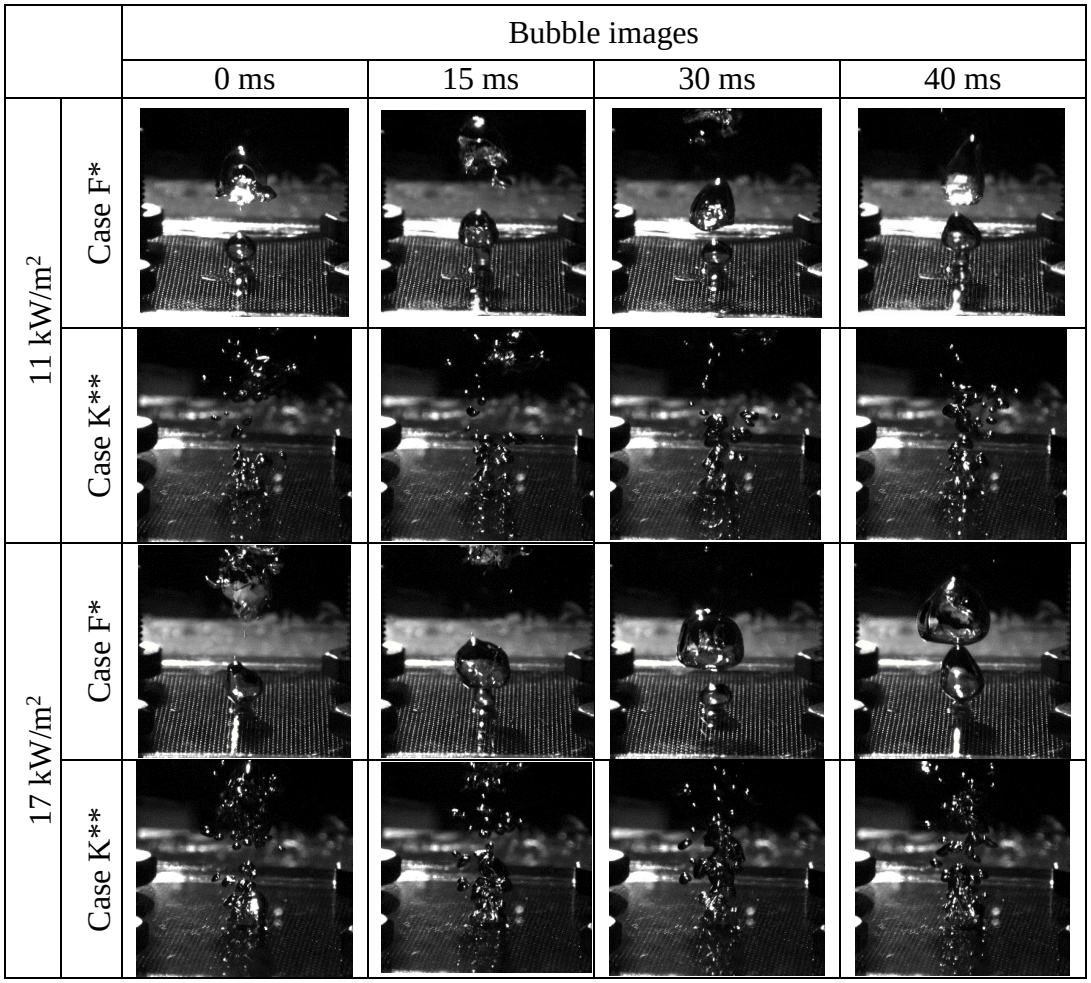

Figure 33. Bubble images comparison between case F and K at different input heat flux (*best performance, ** worst performance)

Figures 34 and 35 show the effects of the induced shear flow when the coalesced bubbles appear to depart from the heating surface. As a result, the surrounding liquid is assumed to be driven into the confined space as induced shear flow, which reduces the heating element surface temperature and tend to homogenize the spatial surface temperature distribution. Figure 35 also shows a common pattern of the shear flow effect on the average heated surface temperature. As the figure shows, the average surface temperature and the standard deviation decrease between 750 and 800 ms, then

increase between 800 and 900 ms. Figure 36 shows how average surface temperature and its standard deviation vary with time (300 to 1000 ms), in which the induced shear flow appears to be intermittent and periodic. The average period of temperature variation shown in Fig. 36 is 170 ms ± 14 ms (8%). The temperature variation indicates that mesh structure regulates the induced shear flow in Case F (2.5 mm mesh hole, 2 mm plate hole). Figure 37 shows how average surface temperature and its standard deviation vary with time in Case D (no mesh, 2 mm plate hole) for the same heat flux input as in Case F. Figure 37 depicts an average period of temperature variation 156.4 ms ± 55.6 ms (36%) for Case D. The relative high standard deviation of average period for Case D suggests that using the mesh in confined pool boiling may regulate the induced shear flow motions, which result in a more periodic surface temperature variation.

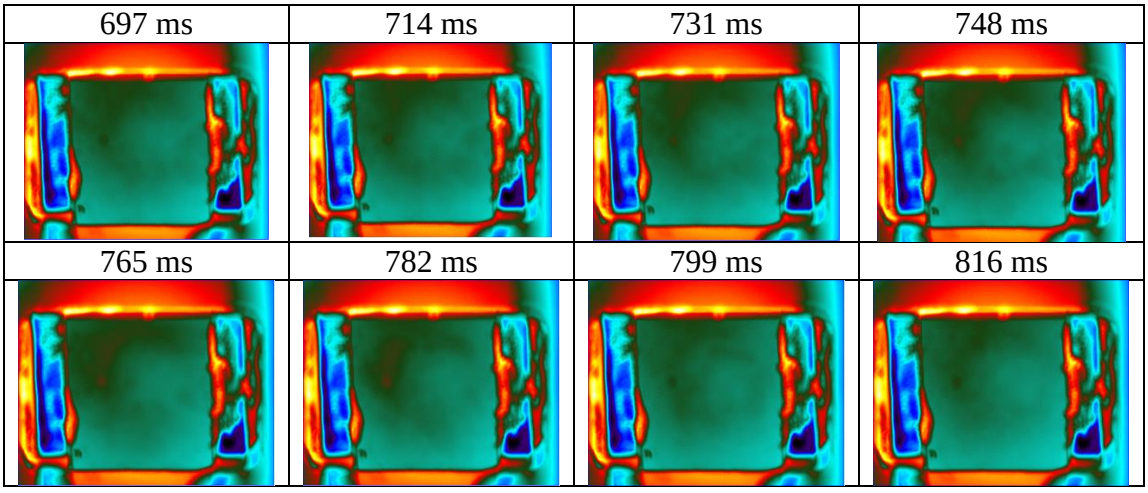

Figure 34. Case F IR images in the confined space when coalesced bubbles departed

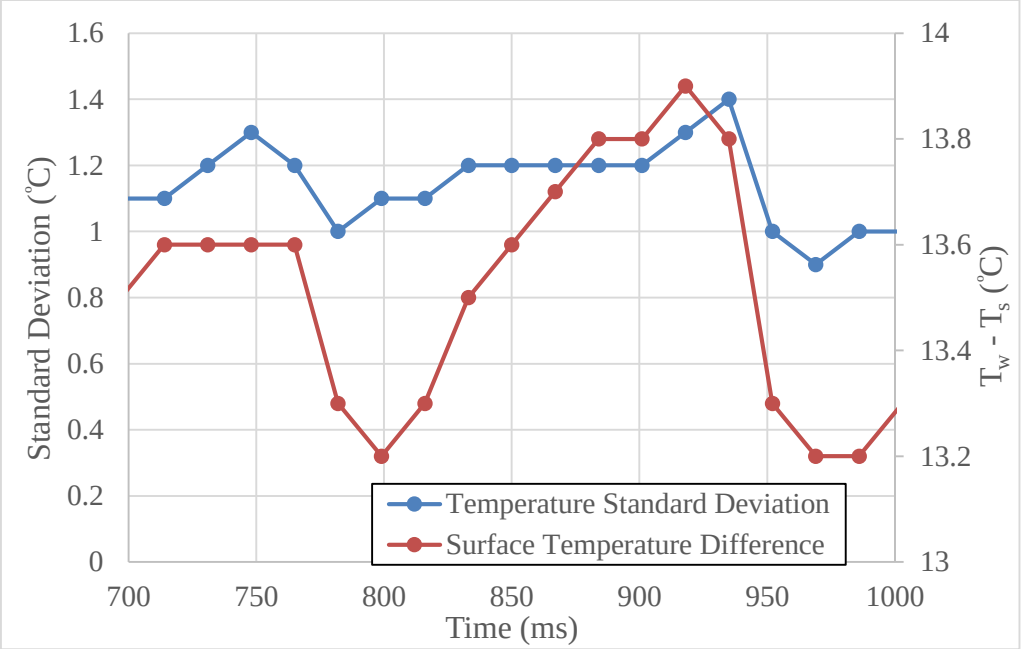

Figure 35. Case F average surface temperature and standard deviation as a function of time, which shows a common pattern of induced shear flow at 17.5 kW/m^2

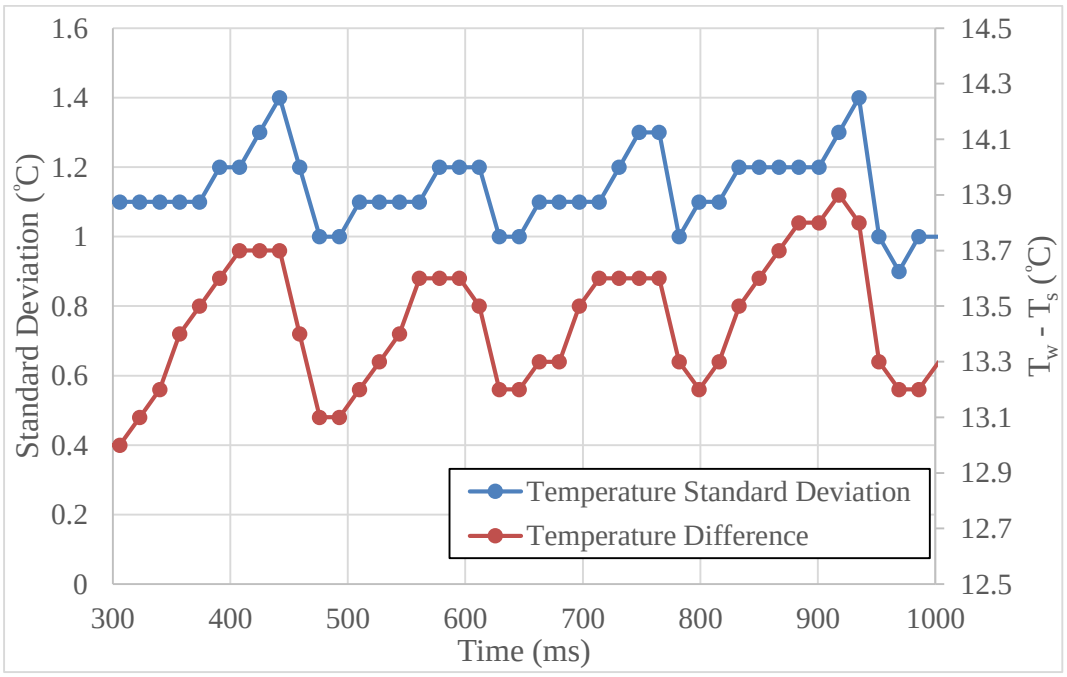

Figure 36. Case F average surface temperature and standard deviation as a function of time, which shows a period of induced shear flow at 17.5 kW/m^2

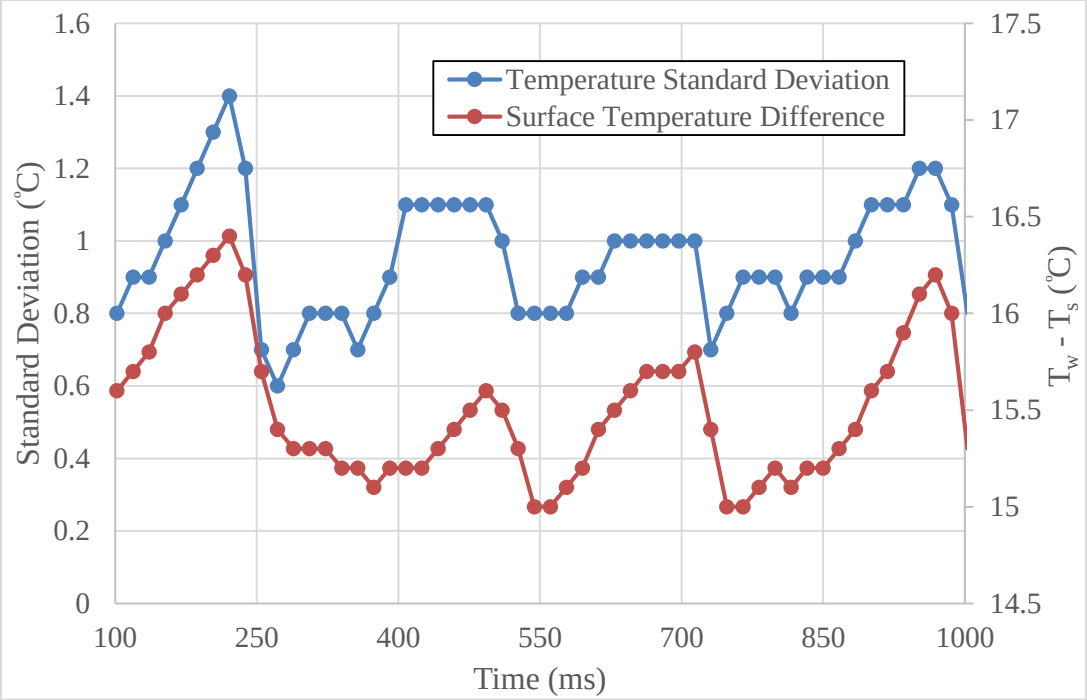

Figure 37. Case D average surface temperature and standard deviation as a function of time, which shows a period of induced shear flow at 17.5 kW/m^2

Furthermore, the heated surface temperature measurement at single points also have similar temperature fluctuation as the average surface temperature. Figure 38 shows where surface temperature at single points were measured. The corresponding results for case F and case D at 17.5 kW/m^2 are shown in Figures 39 through 44. The temperature variations in case D at each point are relatively irregular and random. On the other hand, the single temperature points as shown in Figures 39-41 for Case F depict a more periodic thermal behavior, which suggests that the mesh structure helps control shear flow motion within the confinement cell.

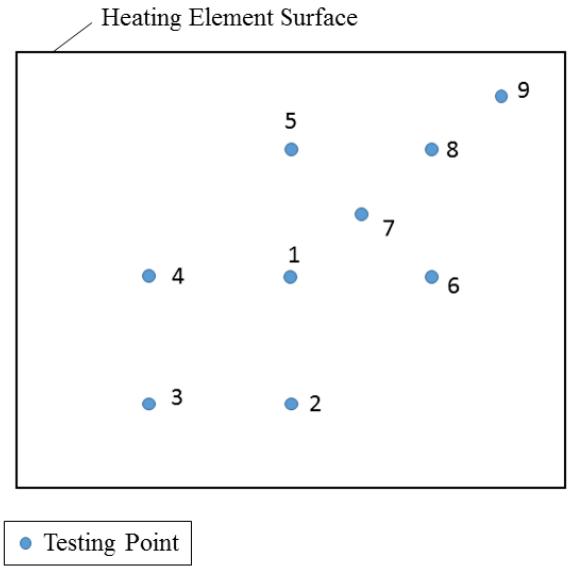

Figure 38. Temperature measurement points distribution at heating element surface

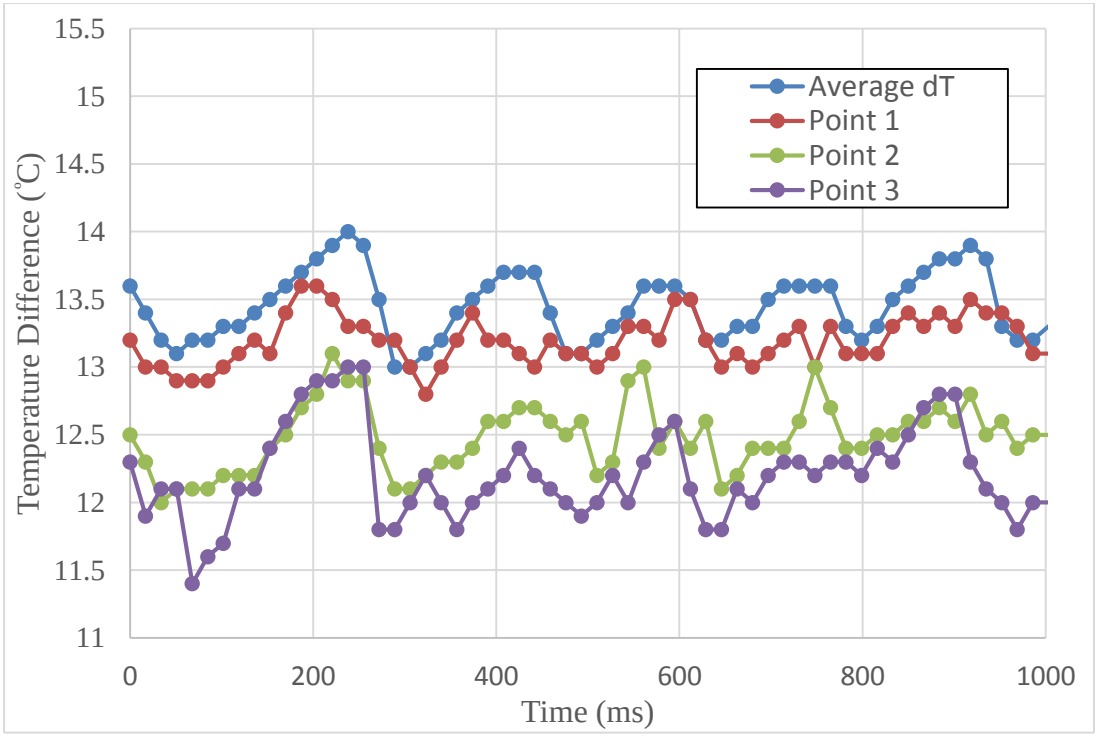

Figure 39. Case F single surface temperature point as a function of time at 17.5 kW/m^2

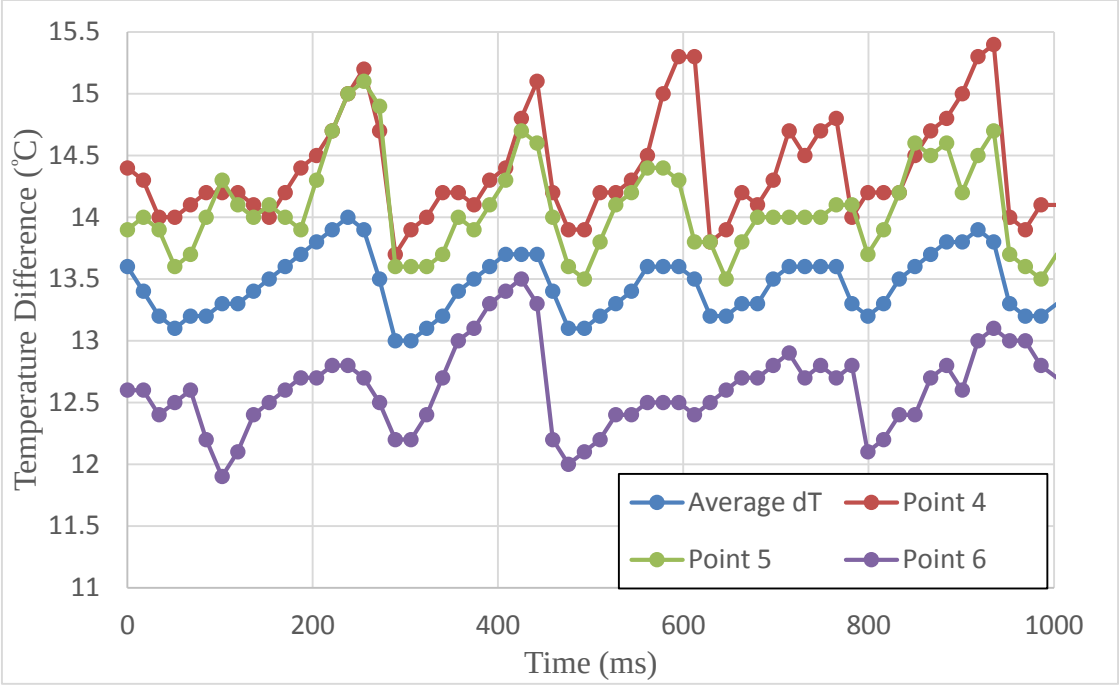

Figure 40. Case F single surface temperature point as a function of time at 17.5 kW/m^2

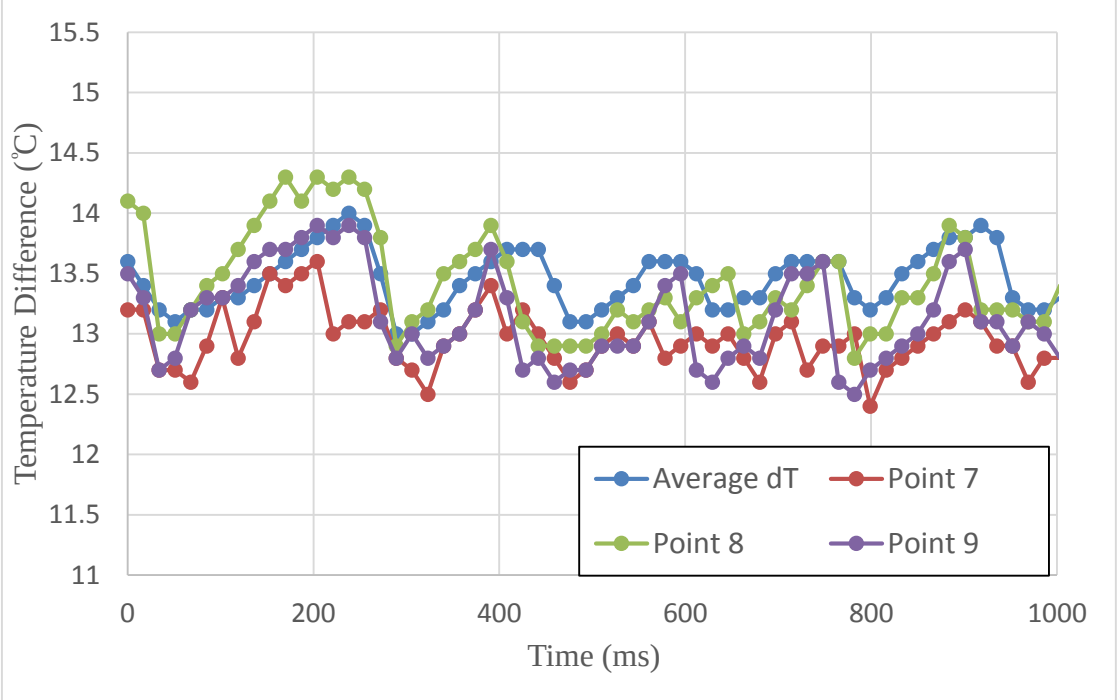

Figure 41. Case F single surface temperature point as a function of time at 17.5 kW/m^2

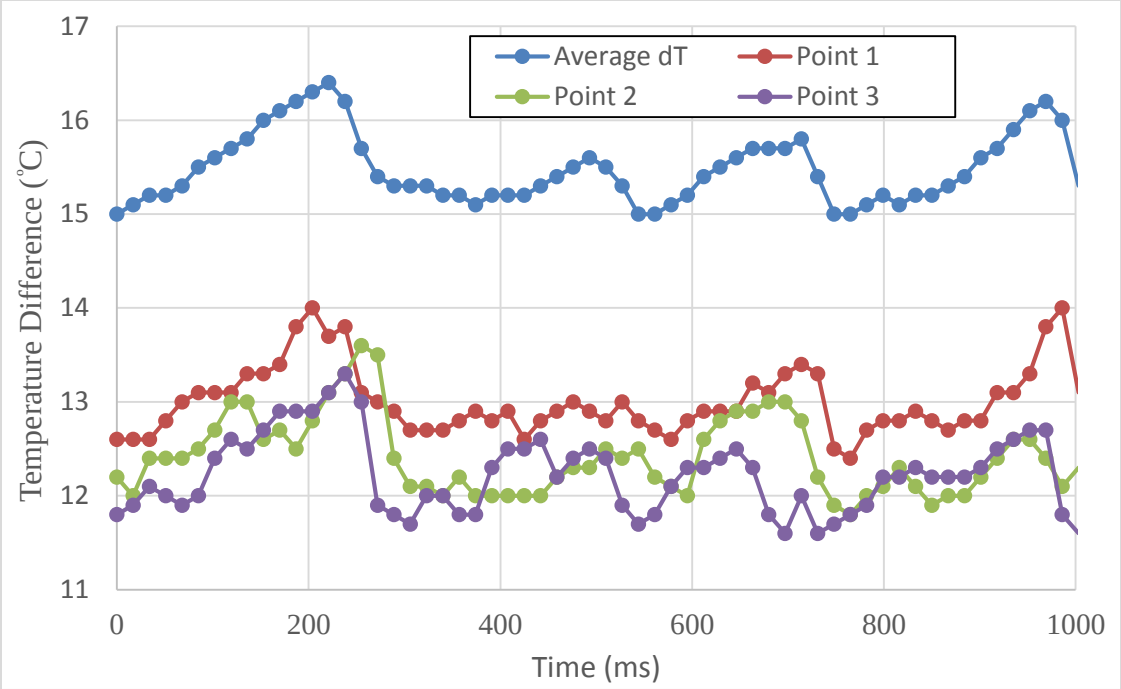

Figure 42. Case D single surface temperature point as a function of time at 17.5 kW/m^2

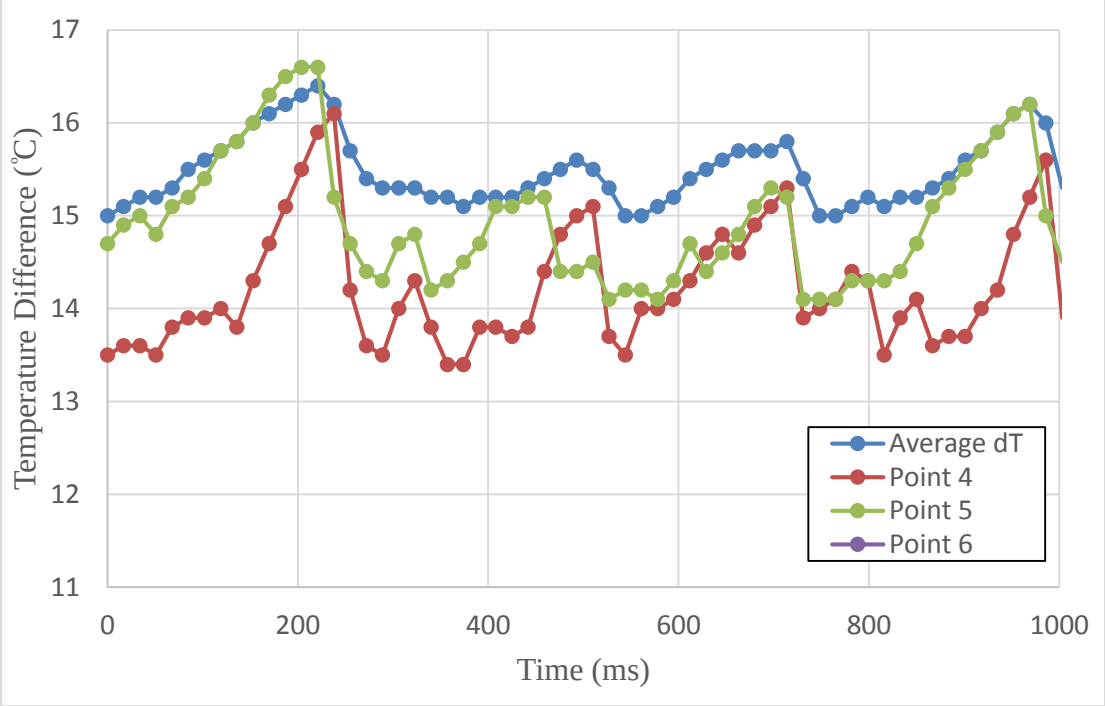

Figure 43. Case D single surface temperature point as a function of time at 17.5 kW/m^2

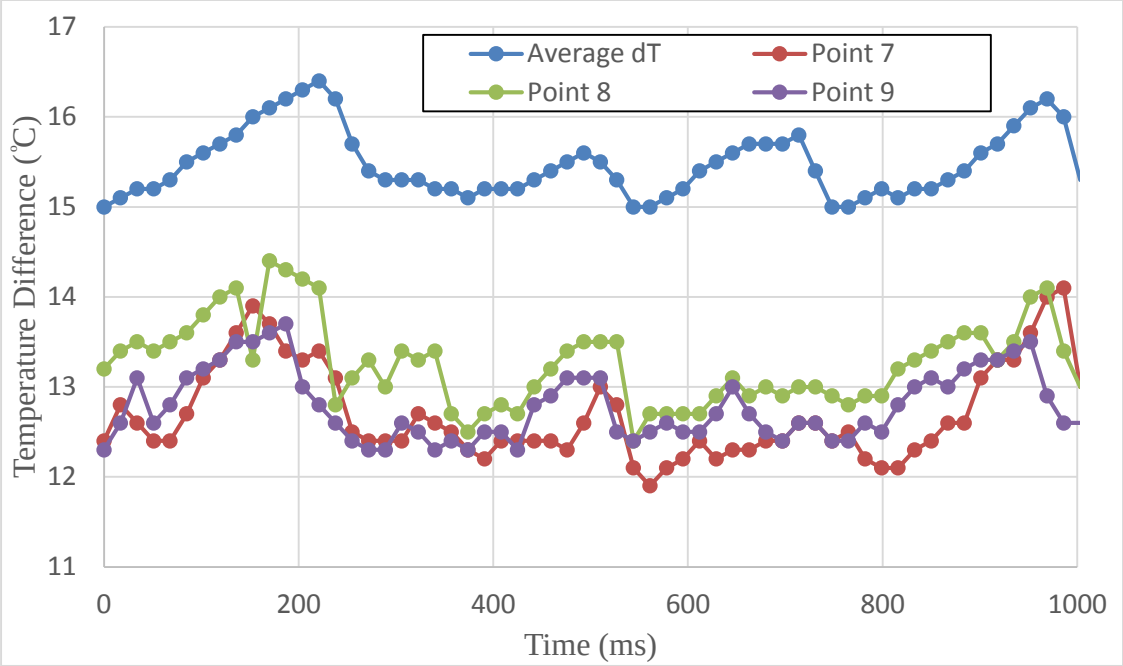

Figure 44. Case D single surface temperature point as a function of time at 17.5 kW/m^2

4.3 Pump assisted test

Pump assisted tests were conducted in order to further investigate the mechanisms in confined pool boiling. Case F (2.5 mm mesh orifice and 2 mm plate orifice), case D (no mesh and 2 mm plate orifice) and case E (no mesh and 4 mm plate orifice) were considered in the study. The pump assisted tests focused on three different heat flux regions (9.5, 13 and 17.5 kW/m^2), where the boiling curves were more diverse, as shown in Figure 45.

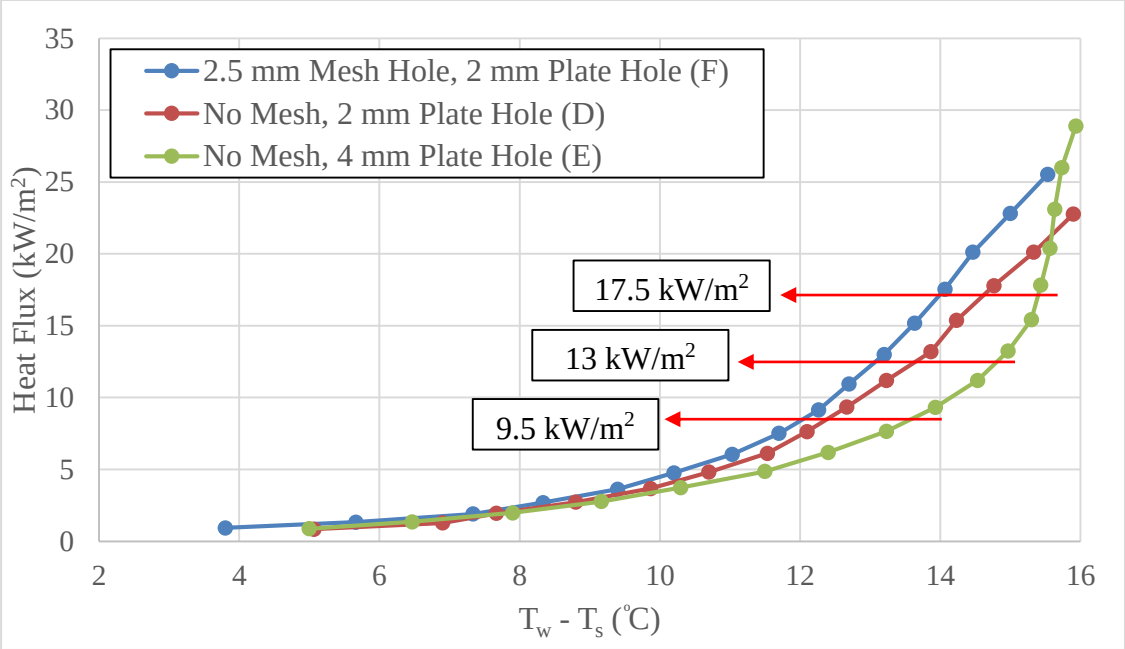

Figure 45. Pump assisted cases and heat flux regions selection

The pump power input was maintained at 0.44 Watt during the tests. Equation 4.3 can be used to describe the influence of the pump system on the pool boiling process.

$$\eta\ (\%) = \frac{Pump\ Power\ Input\ (W)}{Heater\ Power\ Input\ (W)} \times 100\% \tag{4.3}$$

Where the η is the pump influence factor. The pump influence factors for each case at different heat flux values are listed in Table 7. It can be seen that the pump power input is relatively small compared to the heating element power input, which means the influence of the pump on the pool boiling process could be considered to be insignificant. Consequently, the pump assisted test can provide an estimation of the pool boiling heat

transfer mechanisms by allowing the direct measurement of vapor flow and vapor quality throughout the confined well.

Heat Flux Input (kW/m^2)	2.5 mm Mesh Hole, 2 mm Plate Hole (F)	No Mesh, 2 mm Plate Hole (D)	No Mesh, 4 mm Plate Hole (E)
17.5	12%	11%	11%
13	15%	15%	15%
9.5	22%	21%	21%

Table 7. Pump influence factors

The pump assisted test included two parts: the measurement of the pressure inside the confined structures and the two-phase flow quality estimation. The results of these tests are introduced in the following sections.

4.3.1 Measurement of pressure inside confined structures

The pressure profiles inside different confined structures were acquired by using a pressure transducer during pump assisted pool boiling tests. The pressure transducer recorded the pressure data for 10 seconds. The average pressure was then used as the pressure condition at the certain heat flux input. The standard deviation of the measurement of pressure was less than 0.25 kPa (less than 1% in error). The results of the pressure measurement are shown in Figure 46.

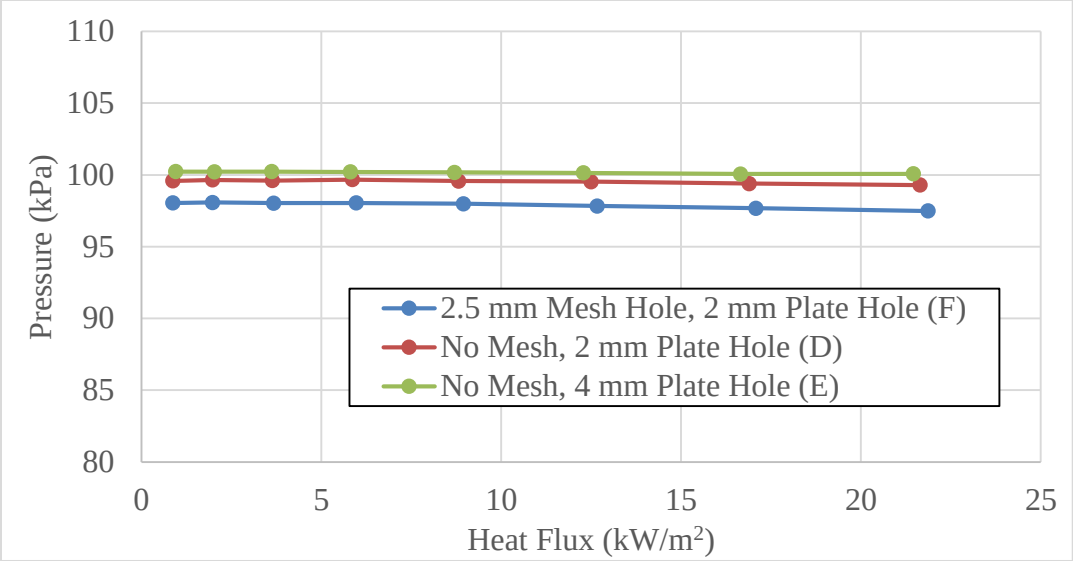

Figure 46. Pressure profiles inside different confined structures

It can be seen from Figure 36 that although the pool boiling heat transfer performances were different, the pressure profiles inside the confined structures showed no significant difference when a metallic mesh was used. Furthermore, the pressure values were nearly constant during the tests. The pressure profiles only had a 3% difference when using different confined structures. Consequently, the pressure condition is not a major factor on the heat transfer process in the confined structures pool boiling.

4.3.2 Two-phase flow quality estimation

The two-phase flow quality estimation tests included two parts: The total mass flow rate measurement and the vapor mass flow rate estimation. As discussed in section 3.2.4, the total mass flow rate was acquired by manually opening a three-way valve for

30 seconds and using a balance to measure the weight of fluid coming through the condenser. The vapor mass flow rate was determined by using vapor density and the vapor volume flow rate based on the high speed images as explained above. The two-phase flow quality was calculated by using Equation 3.2.

The results of the total mass flow rate measurement are shown in Figure 47. The standard deviation of the mass flow rate measurement was less than 2.2 g/min (less than 2%). The numbers marked above the mass flow rate bars are the corresponding heat transfer coefficients (kW/m^2-K) in confined pool boiling tests. As seen from Figure 47, the influence of increasing input heat flux on the total mass flow rate was not significant. The direct relation between the heat transfer coefficient and the total mass flow rate still is ambiguous.

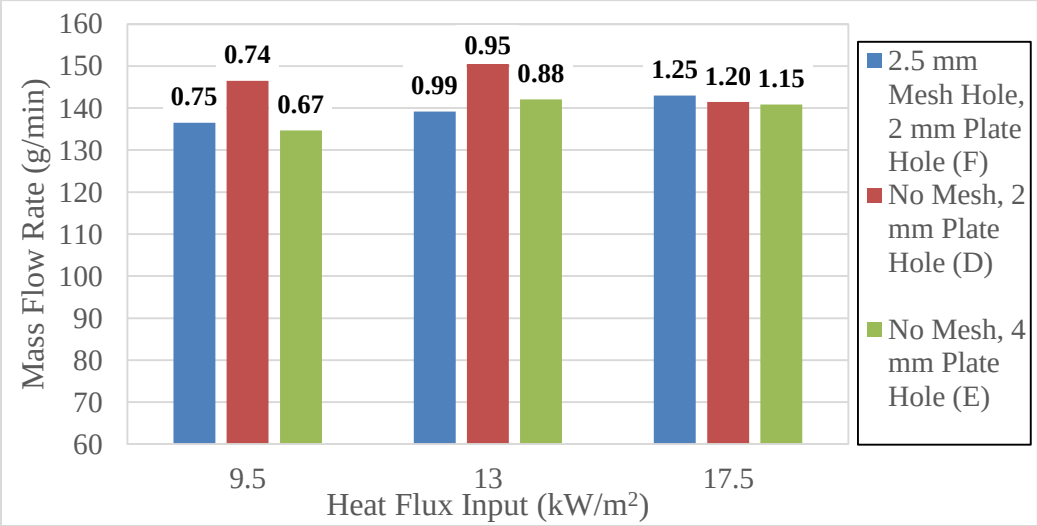

Figure 47. Total mass flow rate as a function of heat flux, case F, D and E. Heat transfer coefficients (kW/m2-K) in confined boiling are marked above the bars

The results of the two-phase flow quality estimation are shown in Table 8 and Figures 48 and 49. The uncertainty of quality measurement was about 13%. It is relatively high because of the random bubble motions inside the marked tube.

	2.5 mm Mesh Hole, 2 mm Plate Hole (F)		No Mesh, 2 mm Plate Hole (D)		No Mesh, 4 mm Plate Hole (E)	
Average Heat Flux (kW/m^2)	Heat Transfer Coefficient (kW/m^2-K)	Quality (%)	Heat Transfer Coefficient (kW/m^2-K)	Quality (%)	Heat Transfer Coefficient (kW/m^2-K)	Quality (%)
9.5	0.75	24	0.74	16	0.67	10
13	0.99	26	0.95	21	0.88	18
17.5	1.25	45	1.21	32	1.15	30

Table 8. Two-phase flow quality with heat transfer coefficient in confined pool boiling, case F, D and E

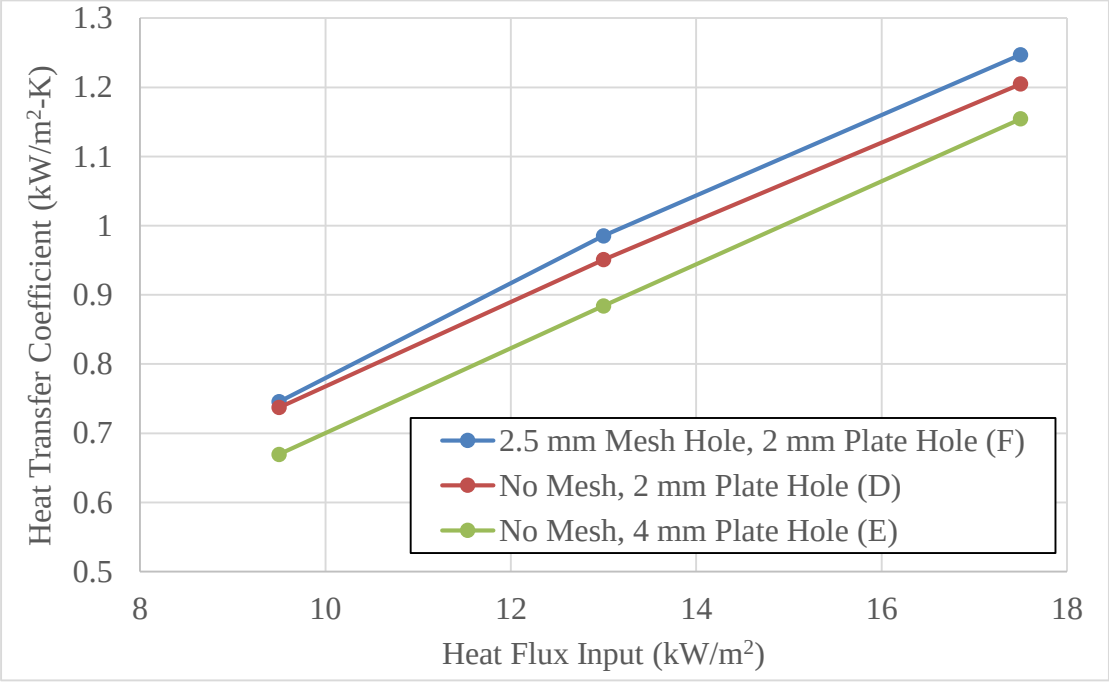

Figure 48. Heat transfer coefficient as a function of input heat flux, case F, D and E.

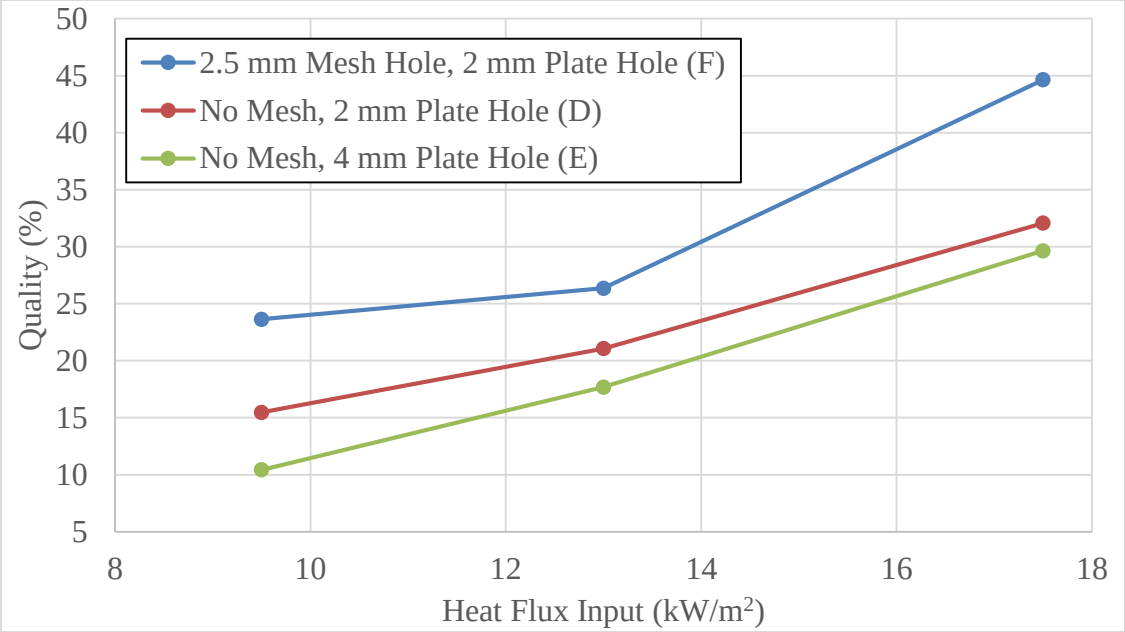

Figure 49. Two-phase flow quality as a function of input heat flux, case F, D and E

As shown in Figure 48, increasing the input heat flux would improve the two-phase flow quality. Furthermore, at the same input heat flux, the case with a higher two-phase flow quality had a higher heat transfer coefficient. The two-phase flow quality directly reflects the amount of generated vapor. A higher quality indicates that more working fluid is evaporated during the pool boiling process. The above figures and table also show that Case F (2.5 mm mesh orifice and 2 mm plate orifice) is the best performer when compared to the other two cases (D and E). Therefore, using a metallic mesh also leads to greater vapor quality, which is indicative of the enhanced two-phase flow process.

In order to further understand the mechanisms of the confined pool boiling, a model has been proposed to estimate the liquid shear stress inside the confined structures. Several assumptions have been made in an effort to simplify the calculations. Firstly, the

confined plate is assumed to be a circular plate. Secondly, the two-phase flow is considered to be homogenous at each radial distance, meaning that the liquid and vapor phases have the same radial velocity. Thirdly, the two-phase flow quality linearly increases from zero to the measured value in the radial direction, as shown in Figure 50.

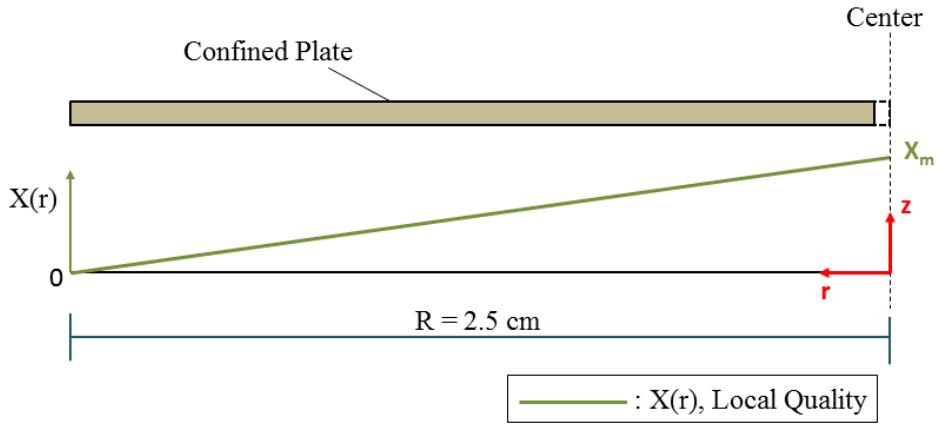

Figure 50. Assumption of quality change inside confined space

Figure 50 shows the variation of quality in the radial direction, where *X(r)* is the local quality as a function of *r*, X_m is the measured two-phase flow quality, *R* is the radius of confined plate. The local quality can be determined using following equation:

$$X(r) = -\frac{X_m}{R}r + X_m \tag{4.3}$$

Furthermore, the flow velocity at the circumference of the confined plate (u_{in}) and at the plate orifice (u_{exit}) can be calculated by using Equations 4.4 and 4.5

$$u_{in} = \frac{\dot{m}}{\rho_l 2\pi R \cdot Th} \tag{4.4}$$

$$u_{exit} = \frac{\dot{m}}{\rho_{mix} \pi r_{orifice}^2} \tag{4.5}$$

Where $\dot{m}$ is the measured total mass flow rate, ρ_l is the liquid density, Th is the height of confined space (1.3 mm for the mesh confined structure, 2.3 mm for no mesh confined structure), ρ_{mix} is the two-phase flow density, $r_{orifice}$ is the plate orifice radius.

Then, it is assumed that the vapor would accumulate at the bottom of the confined plate or mesh or at the top of the confinement cell. The slip condition is also assumed at the interface between the liquid and vapor phases; however, there is no slip-condition between heated surface and the liquid phase. Furthermore, the local liquid velocity is linearly changing in the z direction, as shown in Figure 51.

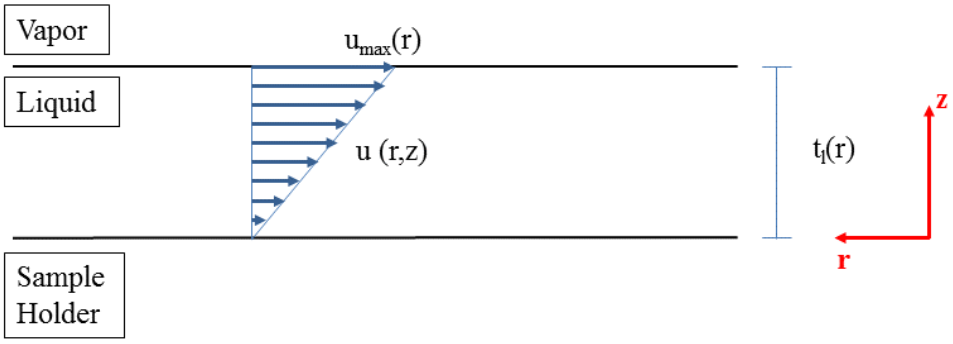

Figure 51. Assumption for local liquid velocity

Where *u (r,z)* is the local liquid velocity, $u_{max}(r)$ is the local liquid maximum velocity, $t_l(r)$ is the local liquid thickness.

Furthermore, it is assumed that the local liquid maximum velocity would linearly increase from u_{in} to u_{exit} in the radial direction, as shown in Figure 52.

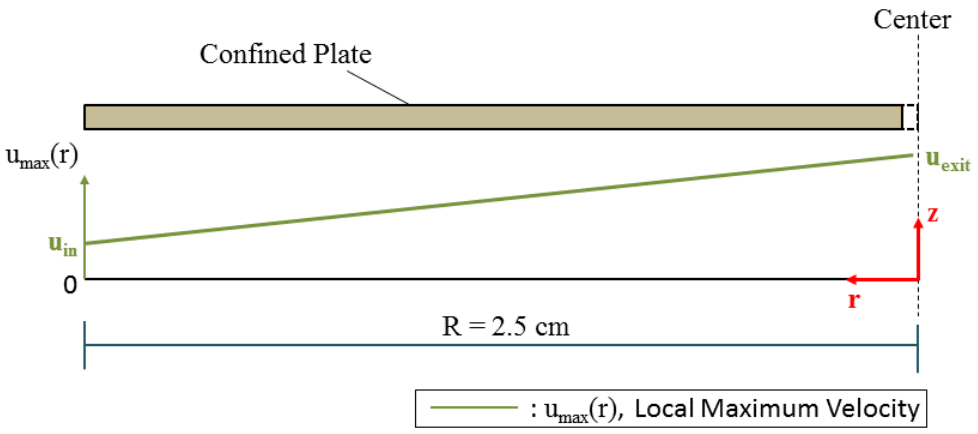

Figure 52. Assumption for local liquid maximum velocity change

Then, the local liquid maximum velocity can be determined by using Equation 4.6.

$$u_{max}(r) = \left(\frac{u_{in} - u_{exit}}{R}\right) r + u_{exit} \tag{4.6}$$

Then, the local quality *X(r)* can be expressed in the following form:

$$X(r) = \frac{\dot{m}_v}{\dot{m}_{tot}} = \frac{u_{mix}\rho_v A_v(r)}{u_{mix}\left(\rho_v A_v(r) + \rho_l A_l(r)\right)} \tag{4.7}$$

$$X(r) = \frac{\rho_v A_v(r)}{\rho_v A_v(r) + \rho_l A_l(r)}$$

where $\dot{m}_v$ is the local vapor mass flow rate, $\dot{m}_{tot}$ is the local total mass flow rate, u_{mix} is the local two-phase flow velocity, ρ_v is the vapor density, ρ_l is the liquid density, $A_v(r)$ is the local cross sectional area for vapor, $A_l(r)$ is the local cross sectional area of the liquid phase. In Equation 4.7, it is evident that at each radial distance, the liquid and vapor area ratio is equal to the liquid and vapor thickness ratio. By rearranging Equation 4.7, the following equation can be derived:

$$\frac{A_v(r)}{A_l(r)} = \frac{t_v(r)}{t_l(r)} = \frac{X(r)\rho_l}{\rho_v(1-X(r))} \tag{4.8}$$

Where the local liquid thickness, $t_l(r)$, can be determined by:

$$\begin{cases} \dfrac{t_v(r)}{t_l(r)} = \dfrac{X(r)\rho_l}{\rho_v(1-X(r))} \\ Th = t_l(r) + t_v(r) \end{cases} \tag{4.9}$$

$$t_l(r) = \frac{Th \times \rho_v(1-X(r))}{X(r)\rho_l + (1-X(r))\rho_v} \tag{4.10}$$

By knowing the local liquid maximum velocity and the local liquid thickness shown in Figure 42, the local liquid velocity, *u(r,z),* can be calculated by Equation 4.11

$$u(r,z) = \frac{u_{max}(r)}{t_l(r)} z \tag{4.11}$$

Finally, the local shear stress can be determined by Equation 4.12

$$\tau = \mu \frac{du}{dz} = \mu \frac{u_{max}(r)}{t_l(r)} \tag{4.12}$$

Where τ is the local shear stress, μ is the kinematic viscosity. The local shear stress for cases F, D and E for different input heat flux values at the middle point of the confined plate (r = 1 cm) have been calculated and are shown in Table 9. The results in this table can provide an estimation of the shear stress condition within the confined space.

	2.5 mm Mesh Hole, 2 mm Plate Hole (F)	No Mesh, 2 mm Plate Hole (D)	No Mesh, 4 mm Plate Hole (E)
Heat Flux (kW/m^2)	Shear Stress (mPa)	Shear Stress (mPa)	Shear Stress (mPa)
9.5	7.9	4.4	1.0
13	8.0	4.7	1.1
17.5	9.5	4.8	1.2

Table 9. Shear stress estimation for case F, D and E as a function of input heat flux at r = 1 cm

As shown in the Table 9, increasing heat flux can only slightly change the shear stress. However, a significant increase in shear stress can be found when using different confined structures. The higher shear stress in the confined space indicates that the effect of induced shear flow rate should be considered in the heat transfer analysis. Previous studies have shown that higher shear rate can improve bubble departure frequency and enhance the heat transfer efficiency [20-23, 25]. The findings using the shear stress

model are consistent with those studies. The case with higher shear stress (shear flow rate) also depicts higher heat transfer coefficient values.

The results of the two-phase flow quality estimation and the shear stress model generally support the notion that the bubble coalescence process would enhance the pool boiling heat transfer in two main ways: the supplementary microlayer vaporization during bubble coalesced process and the induced shear flow caused by the coalesced bubble departure. The supplementary microlayer vaporization increases the latent heat transfer and bubble departure diameter and locally reduces the wall temperature. The induced shear flow removes the superheated layer at the heated surface and promotes the bubble departure frequency. An increase of vapor generation (quality) and the induced shear flow rate (shear stress) can be found when increasing the level of confinement on the pool boiling process. The confined structure that provides the highest bubble restriction (the smallest mesh and plate orifice) had the highest two-phase flow quality and induced shear flow rate, which result in the most significant enhancement on the pool boiling heat transfer (i.e. Case F).

Furthermore, although the pump power input was relatively low when compared to the heating element power input, the heat transfer performance in pump assisted tests would lead to enhanced heat transfer performance, as shown in Figure 53. However, using a mesh in confined structure can still provide a higher heat transfer coefficient when compared to the no-mesh cases when a pump is used to facilitate bubble departure, as shown in Figure 54. This behavior suggests that the mesh in a confined structure can enhance the pool boiling heat transfer process more than the pump (forced convection).

Therefore, the mesh but no-pump test results suggest that bubble permeation through the mesh could lead to better phase separation, which cannot be replicated using a solid plate.

Figures 55 and 56 show that when the pump is used, the level of flow intermittence (i.e. periodic flow behavior) diminishes, resulting in lower average surface temperature. Same trend can also be found in Figures 57 and 58, which show the heated surface temperature measurement at different single points. The variations of temperature (standard deviations) at each point in Case F and D when using a pump (0.07 ℃) are relatively small compared to the same cases without using the pump (0.4 ℃). This behavior also suggests that the pump-assisted system reduces the periodicity of the shear flow induced by large bubble coalescence taking place within the confinement cell. Furthermore, Figures 55 and 56 also show that the standard deviation of surface temperature (or temperature variation along the surface) is greater than for the cases without the use of the pump (see Figures 36-37). The results suggest that by using a pump, the variation in quality within the confinement region is probably greater than when no pump is used.

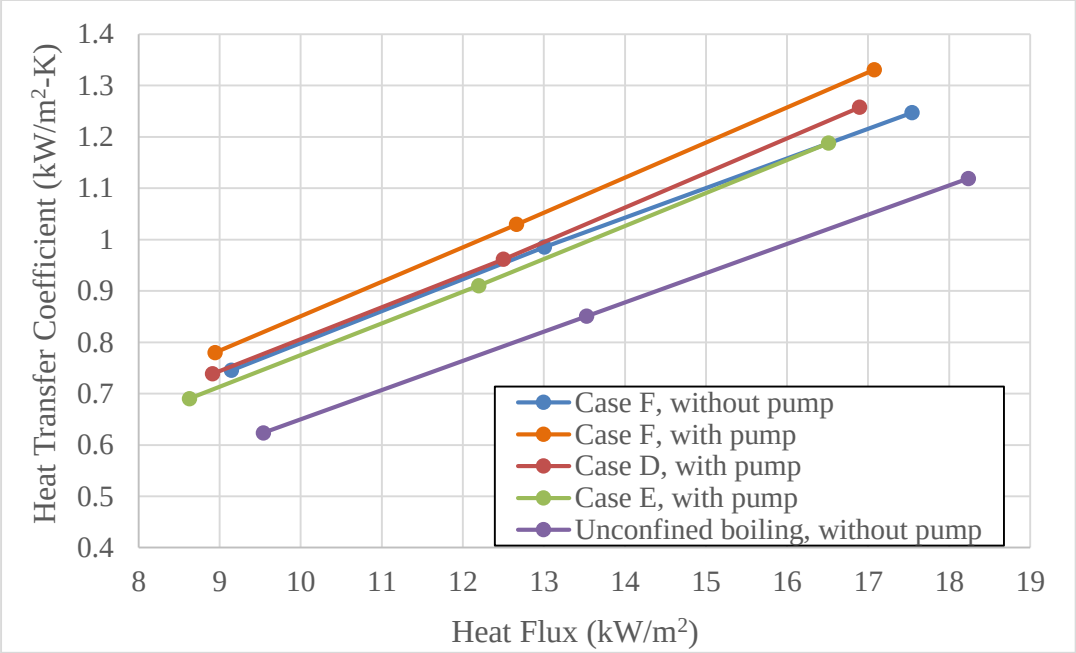

Figure 53. Heat transfer coefficient comparison between case F (2.5 mm mesh hole, 2 mm plate hole) without pump, case D (no mesh, 2 mm plate hole) with pump, case E (no mesh, 4 mm plate hole) with pump and unconfined pool boiling

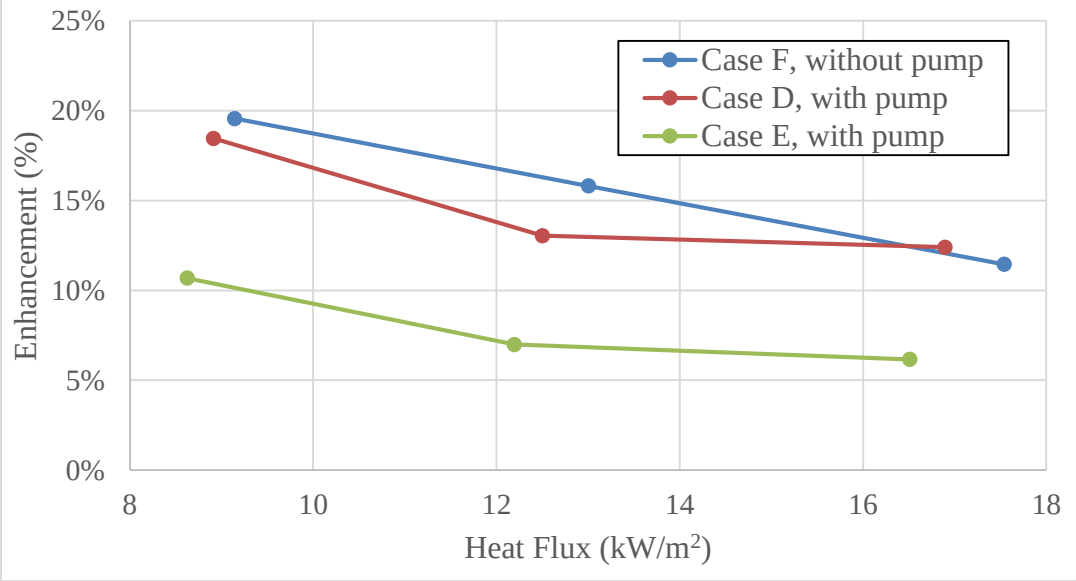

Figure 54. Enhancement percentage of heat transfer coefficient between case F (2.5 mm mesh hole, 2 mm plate hole) without pump, case D (no mesh, 2 mm plate hole) with pump and case E (no mesh, 4 mm plate hole) with pump

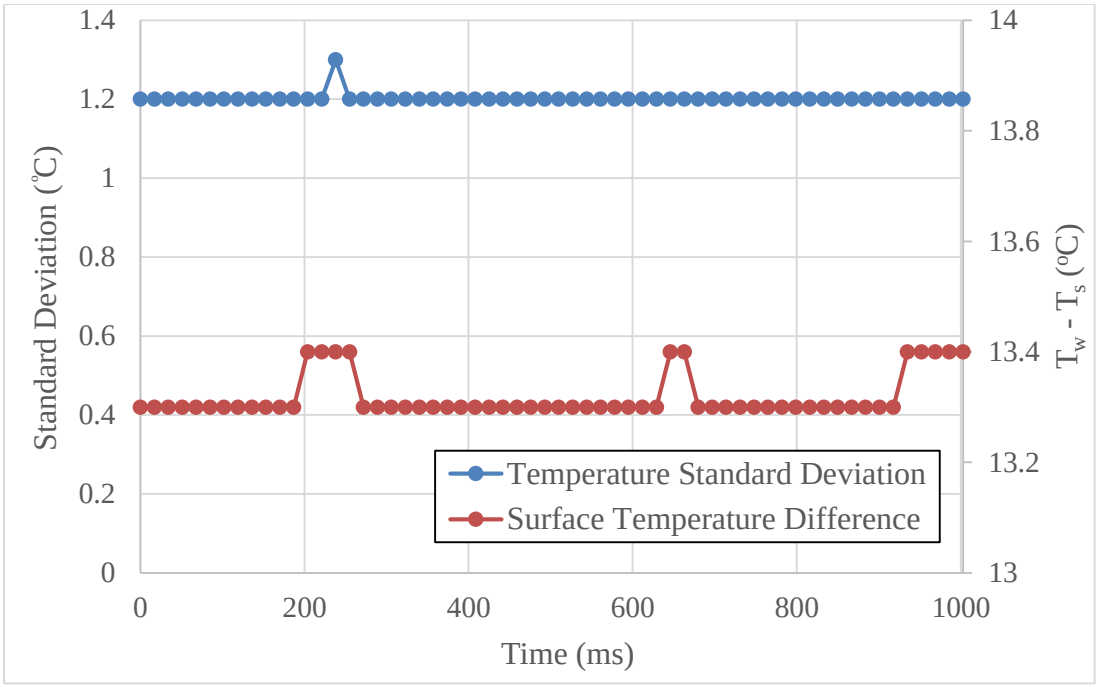

Figure 55. Case F with pump average surface temperature and standard deviation as a function of time 17.5 kW/m^2

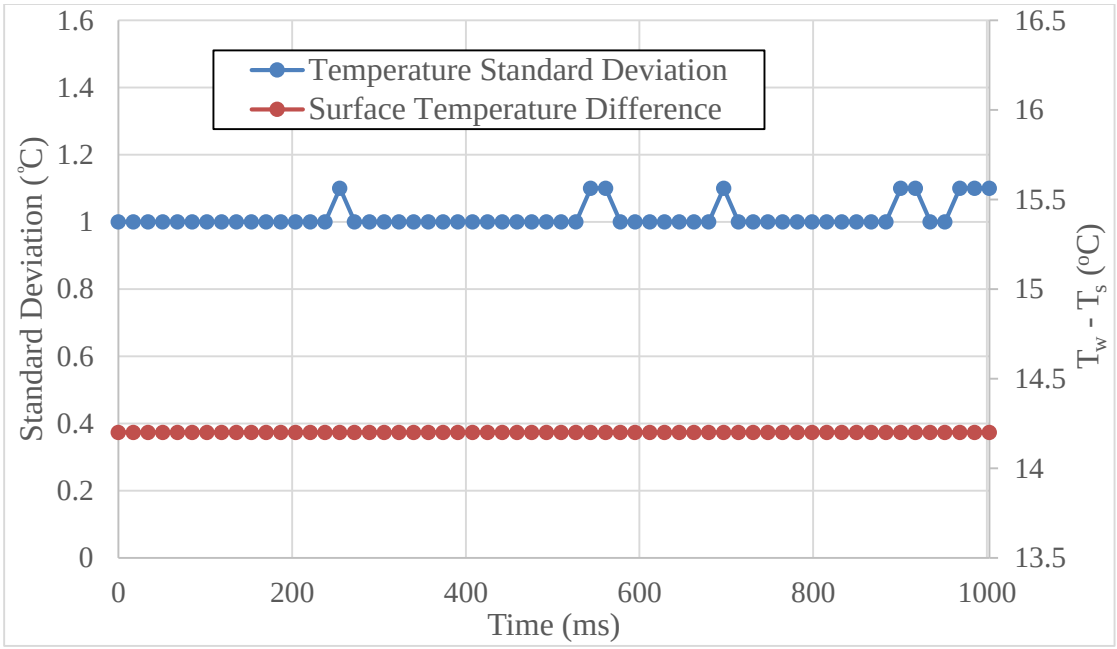

Figure 56. Case D with pump average surface temperature and standard deviation as a function of time 17.5 kW/m^2

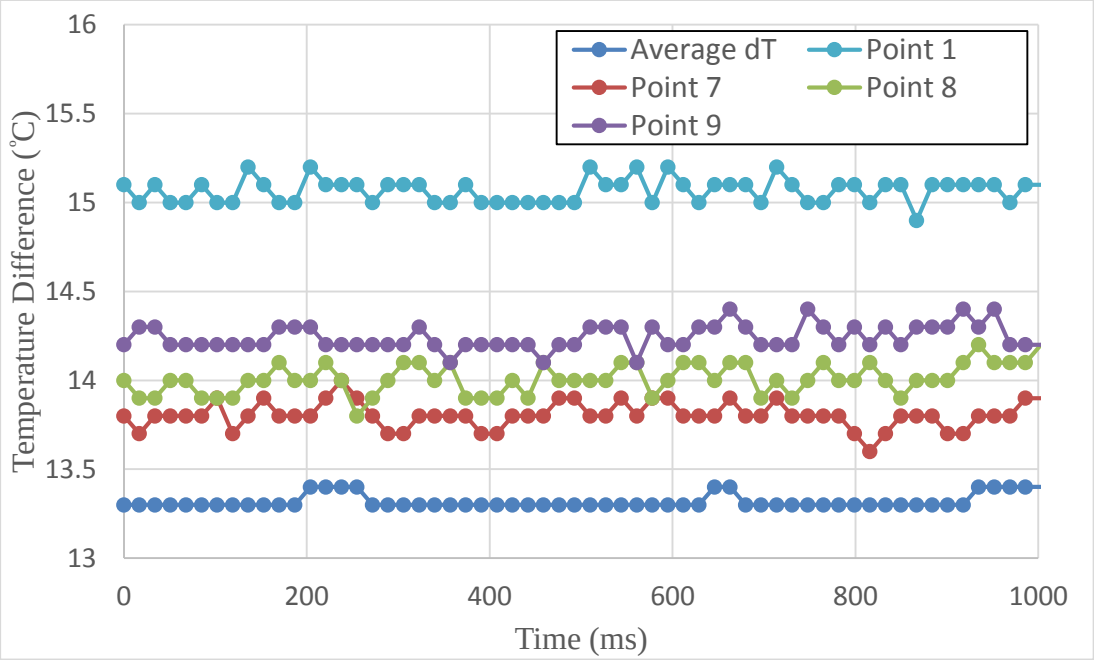

Figure 57. Case F with pump single surface temperature point as a function of time at 17.5 kW/m^2

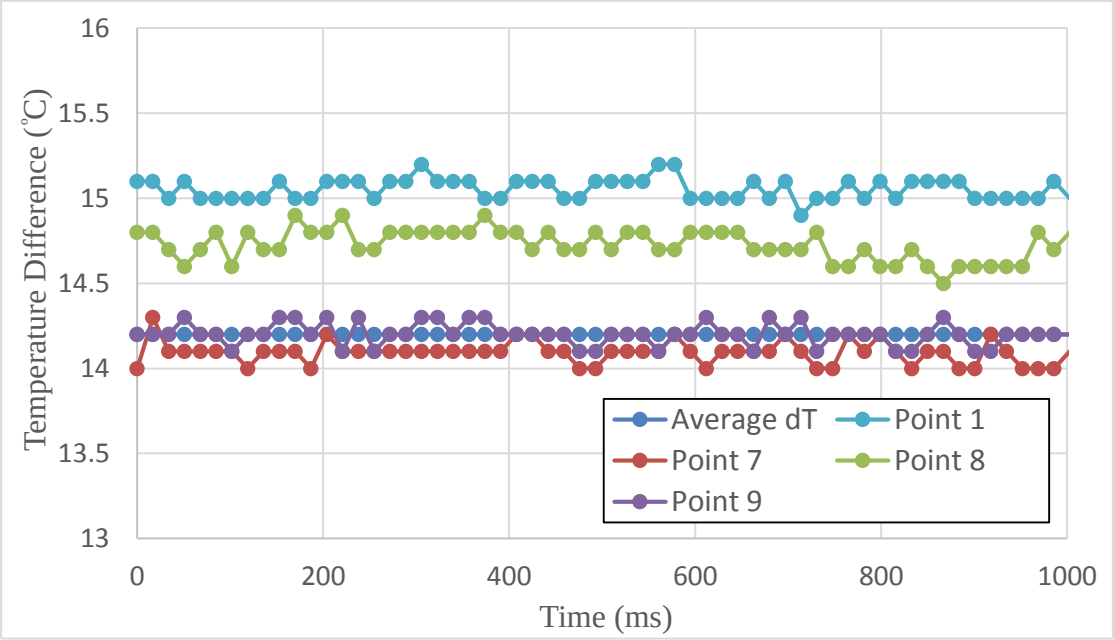

Figure 58. Case D with pump single surface temperature point as a function of time at 17.5 kW/m^2

5. CONCLUSION

The confined structures including the flange, the confined plate with a central orifice (2 and 4 mm diameter) and the mesh with a central orifice (2.5, 3.5 and 4.5 mm diameter) were studied in order to understand the effects of confinement on the pool boiling heat transfer. The images of bubble motions and the heated surface temperature profiles were also acquired by using a high speed camera and an infrared camera. Furthermore, the pressure condition inside the confined space and the two-phase flow quality during confined pool boiling tests were also obtained by using a pump assisted system.

According to the results of the confined pool boiling tests (cases D – K), the effects of confined structures on the boiling heat transfer can be evaluated. Firstly, the flange-confined structures would not provide a significant change in terms of boiling heat transfer. The boiling curves of flanged cases were nearly identical to the cases without flanges. Secondly, the use of the plate and mesh confined structures would significantly improve the heat transfer performance compared to the unconfined pool boiling. Thirdly, reducing mesh orifice size and plate orifice size can generally enhance boiling heat transfer. The best heat transfer performance was achieved by using the smallest plate orifice size (2 mm) and mesh orifice size (2.5 mm).

The enhancement of the confined pool boiling can be attributed to the interplay of several mechanisms including the induced bubble coalescence process and the induced shear flow. The supplementary microlayer vaporization during the bubble

coalescence process is assumed to increase the latent heat transfer and the bubble departure diameter. The induced shear flow caused by the departure of the coalesced bubbles helped remove the superheated layer near the heated surface and could have led to an increase of bubble departure frequency. Consequently, the pool boiling heat transfer efficiency was enhanced.

From the pressure measurement results during confined pool boiling tests, the pressure was not the main factor that improved the pool boiling heat transfer. The pressure remained nearly constant in different confined structure boiling tests.

The results of the two-phase flow quality estimation and the shear stress estimation model showed that the quality and the shear stress would increase when increasing the level of confinement.

In summary, the pool boiling heat transfer process can be enhanced by using a confined structure consisting of flanges, a plate with a central orifice and a mesh with a central orifice. The amount of enhancement depends on the size of plate orifice and mesh orifice. Smaller orifice size at the mesh and the plate results in higher heat transfer enhancement.

REFERENCES

[1] Carey, Van P. "Liquid-vapor phase-change phenomena." New York: Taylor and Francis, (2008).

[2] Nukiyama, Shiro. "The maximum and minimum values of the heat Q transmitted from metal to boiling water under atmospheric pressure." *International Journal of Heat and Mass Transfer* 9, no. 12 (1966): 1419-1433.

[3] Rohsenow, Warren M. "A method of correlating heat transfer data for surface boiling of liquids." *Transactions of ASME* 74, (1953): 969-976

[4] Forster, H. K., and Novak Zuber. "Dynamics of vapor bubbles and boiling heat transfer." *AIChE Journal* 1, no. 4 (1955): 531-535.

[5] Borishanski, V. M. "Correlation of the effect of pressure on the critical heat flux and heat transfer rates using the theory of thermodynamic similarity." *Problems of Heat Transfer and Hydraulics of Two-Phase Media* (1969): 16-37.

[6] Stephan, K., and M. Abdelsalam. "Heat-transfer correlations for natural convection boiling." *International Journal of Heat and Mass Transfer* 23, no. 1 (1980): 73-87.

[7] Forster, K. E., and R. Greif. "Heat transfer to a boiling liquid: mechanism and correlations." *ASME Journal of Heat Transfer* 81, (1959): 43-53.

[8] Mikic, B.B. and W. M. Rohsenow. "A new correlation of pool-boiling data including the effect of heating surface characteristics." *Journal of Heat Transfer* 91, no. 2 (1969): 245-250.

[9] Mikic, B.B. and W. M. Rohsenow. "Bubble growth rates in non-uniform temperature field." *Prog. Heat Mass Transfer* 2 (1969): 283-292.

[10] Dhir, V. K. "Boiling heat transfer." *Annual Review of Fluid Mechanics* 30, no. 1 (1998): 365-401.

[11] Corty, Claude, and Alan Shivers Foust. "Surface variables in nucleate boiling." New York: American Institute of Chemical Engineers, (1953).

[12] Berenson, P. J. "Experiments on pool-boiling heat transfer." *International Journal of Heat and Mass Transfer* 5, no. 10 (1962): 985-999.

[13] Bankoff, S. G. "The prediction of surface temperatures at incipient boiling." *Chemical Engineering Progress Symposium Series, AIChE*, vol. 55, (1959): 87-94.

[14] Phan, Hai Trieu, Nadia Caney, Philippe Marty, Stéphane Colasson, and Jérôme Gavillet. "Surface wettability control by nanocoating: the effects on pool boiling heat transfer and nucleation mechanism." *International Journal of Heat and Mass Transfer* 52, no. 23 (2009): 5459-5471.

[15] Takata, Y., S. Hidaka, J. M. Cao, T. Nakamura, H. Yamamoto, M. Masuda, and T. Ito. "Effect of surface wettability on boiling and evaporation." *Energy* 30, no. 2 (2005): 209-220.

[16] Kaneyasu, Nishikawa, Fujita Yasunobu, Uchida Satoru, and Ohta Haruhiko. "Effect of surface configuration on nucleate boiling heat transfer." *International Journal of Heat and Mass Transfer* 27, no. 9 (1984): 1559-1571.

[17] Park, K-A., and A. E. Bergles. "Effects of size of simulated microelectronic chips on boiling and critical heat flux." *Journal of Heat Transfer* 110, no. 3 (1988): 728-734.

[18] Bakhru, Nanik, and John H. Lienhard. "Boiling from small cylinders." *International Journal of Heat and Mass Transfer* 15, no. 11 (1972): 2011-2025.

[19] Lu, Ming-Chang, Renkun Chen, Vinod Srinivasan, Van P. Carey, and Arun Majumdar. "Critical heat flux of pool boiling on Si nanowire array-coated surfaces." *International Journal of Heat and Mass Transfer* 54, no. 25 (2011): 5359-5367.

[20] Klausner, J. F., R. Mei, D. M. Bernhard, and L. Z. Zeng. "Vapor bubble departure in forced convection boiling." *International Journal of Heat and Mass Transfer* 36, no. 3 (1993): 651-662.

[21] Situ, Rong, Takashi Hibiki, Mamoru Ishii, and Michitsugu Mori. "Bubble lift-off size in forced convective subcooled boiling flow." *International Journal of Heat and Mass Transfer* 48, no. 25 (2005): 5536-5548.

[22] Koumoutsos, N., R. Moissis, and A. Spyridonos. "A study of bubble departure in forced-convection boiling." *Journal of Heat Transfer* 90, no. 2 (1968): 223-230.

[23] Ivey, H. J. "Relationships between bubble frequency, departure diameter and rise velocity in nucleate boiling." *International Journal of Heat and Mass Transfer* 10, no. 8 (1967): 1023-1040.

[24] Bergles, A. E., and W. M. Rohsenow. "The determination of forced-convection surface-boiling heat transfer." *Journal of Heat Transfer* 86, no. 3 (1964): 365-372.

[25] Yilmaz, Salim, and J. W. Westwater. "Effect of velocity on heat transfer to boiling Freon-113." *Journal of Heat Transfer* 102, no. 1 (1980): 26-31.

[26] Siegel, R., and E. G. Keshock. "Effects of reduced gravity on nucleate boiling bubble dynamics in saturated water." *AIChE Journal* 10, no. 4 (1964): 509-517.

[27] Merte Jr, Herman. "Nucleate pool boiling: High gravity to reduced gravity; liquid metals to cryogens." *New Mexico Univ., Transactions of the Fifth Symposium on Space Nuclear Power Systems* 1001 (1988): 437-442.

[28] Rainey, K. N., S. M. You, and S. Lee. "Effect of pressure, subcooling, and dissolved gas on pool boiling heat transfer from microporous, square pin-finned surfaces in FC-72." *International Journal of Heat and Mass Transfer* 46, no. 1 (2003): 23-35. 23-35.

[29] Incropera, Frank P., and Frank P. Incropera. "Fundamentals of Heat and Mass Transfer." Hoboken, NJ: John Wiley, (2007).

[30] Lienhard, John H., and Roger Eichhorn. "Peak boiling heat flux on cylinders in a cross flow." *International Journal of Heat and Mass Transfer* 19, no. 10 (1976): 1135-1142.

[31] Kandlikar, Satish G. "Development of a flow boiling map for subcooled and saturated flow boiling of different fluids inside circular tubes." *Journal of Heat Transfer* 113, no. 1 (1991): 190-200.

[32] Petukhov, B. S., and V. N. Popov. "Theoretical calculation of heat exchange and frictional resistance in turbulent flow in tubes of an incompressible fluid with variable physical properties." *High Temperature* 1 (1963): 69-83.

[33] Gnielinski, Volker. "New equations for heat and mass-transfer in turbulent pipe and channel flow." *International Chemical Engineering* 16, no. 2 (1976): 359-368.

[34] Bergles, Arthur E. "Enhancement of pool boiling." *International Journal of Refrigeration* 20, no. 8 (1997): 545-551.

[35] Yao, Shi-Chune, and Yung Chang. "Pool boiling heat transfer in a confined space." *International Journal of Heat and Mass Transfer* 26, no. 6 (1983): 841-848.

[36] Zhao, Yaohua, Takaharu Tsuruta, and Chaoyue Ji. "Experimental study of nucleate boiling heat transfer enhancement in a confined space." *Experimental Thermal and Fluid Science* 28, no. 1 (2003): 9-16.

[37] Rops, C. M., R. Lindken, J. F. M. Velthuis, and J. Westerweel. "Enhanced heat transfer in confined pool boiling." *International Journal of Heat and Fluid Flow* 30, no. 4 (2009): 751-760.

[38] Misale, M., G. Guglielmini, and A. Priarone. "Nucleate boiling and critical heat flux of HFE-7100 in horizontal narrow spaces." *Experimental Thermal and Fluid Science* 35, no. 5 (2011): 772-779.

[39] Chia-Hsiang, Hsu. "Enhancement of Pool Boiling Heat Transfer in Confined Space." Master Thesis. College Station: Texas A&M University, (2014).

[40] Zhang, Taolue, Hsin-Min Tsai, and Jorge Alvarado. "Effects of single and double streams of droplet impingements on surface cooling." *Atomization and Sprays* 24, no. 10 (2014): 875-893.

[41] Soriano, Guillermo E., Taolue Zhang, and Jorge L. Alvarado. "Study of the effects of single and multiple periodic droplet impingements on liquid film heat transfer." *International Journal of Heat and Mass Transfer* 77 (2014): 449-463.

[42] Zhang, Taolue, Jorge Alvarado, Anoop Kanjirakat, and Reza Sadr. "Experimental characterization and numerical simulation of crown propagation induced by impingement of droplet train." *Bulletin of the American Physical Society* 59 (2014).

[43] Zhang, Taolue, Jorge Alvarado, Anoop Kanjirakat, and Reza Sadr. "Hydrodynamics of micro-scale surface flows induced by triangulated droplet stream impingement array." *Bulletin of the American Physical Society* 59 (2014).

[44] Zhang, Taolue, J. P. Muthusamy, Jorge L. Alvarado, Anoop Kanjirakat, and Reza Sadr. "Numerical and experimental investigations of crown propagation dynamics induced by droplet train impingement." *International Journal of Heat and Fluid Flow* 57 (2016): 24-33.

[45] Muthusamy, J. P., Taolue Zhang, Jorge Alvarado, Anoop Kanjirakat, and Reza Sadr. "Effects of high frequency droplet train impingement on crown propagation dynamics and heat transfer." *Journal of Heat Transfer* 138, no. 2 (2016): 020903.

[46] Zhang, Taolue, Jorge Alvarado, J. P. Muthusamy, Anoop Kanjirakat, and Reza Sadr. "Effects of high frequency droplet train impingement on spreading-splashing transition, film hydrodynamics and heat transfer." *Journal of Heat Transfer* 138, no. 2 (2016): 020902.

[47] Kline, Stephen J., and F. A. McClintock. "Describing uncertainties in single-sample experiments." *Mechanical Engineering* 75, no. 1 (1953): 3-8.

[48] Del Valle, Victor H., and D. B. R. Kenning. "Subcooled flow boiling at high heat flux." *International Journal of Heat and Mass Transfer* 28, no. 10 (1985): 1907-1920.

[49] Katto, Yoshiro, Sadao Yokoya, and Kozo Teraoka. "Nucleate and transition boiling in a narrow space between two horizontal, parallel disk-surfaces." *Bulletin of JSME* 20, no. 143 (1977): 638-643.

[50] Bonjour, Jocelyn, Marc Clausse, and Monique Lallemand. "Experimental study of the coalescence phenomenon during nucleate pool boiling." *Experimental Thermal and Fluid Science* 20, no. 3 (2000): 180-187.

[51] Zhang, Lei, and Masahiro Shoji. "Nucleation site interaction in pool boiling on the artificial surface." *International Journal of Heat and Mass Transfer* 46, no. 3 (2003): 513-522.

APPENDIX A

UNCERTAINTY ANALYSIS

1. Heat flux measurement

Equation 1 was used to calculate the heat flux value (q") in this research.

$$q'' = \frac{P_{in} - Q_{loss}}{A} \quad (1)$$

Where the P_{in} is the power input from the power supply, Q_{loss} is the heat loss through the sample holder and air, A is the heating element area. It is noted that the power input and heat loss can be calculated from the following equations:

$$P_{in} = I \times V \quad (2)$$

$$Q_{loss} = 0.0939T_d - 0.2659 \quad (3)$$

Where *I* is the input current from the power supply, *V* is the input voltage from the power supply, T_d is the temperature difference between the heating element surface and the liquid saturation temperature. By substituting the Equation 2 and Equation 3 into Equation 1, the expression of the heat flux value uncertainty can be shown as follow:

$$\Delta q'' = \sqrt{\left(\frac{\partial q''}{\partial I}\Delta I\right)^2 + \left(\frac{\partial q''}{\partial V}\Delta V\right)^2 + \left(\frac{\partial q''}{\partial T_d}\Delta T_d\right)^2 + \left(\frac{\partial q''}{\partial A}\Delta A\right)^2} \quad (4)$$

Where the $\Delta q''$is the uncertainty of the heat flux value, ΔI is the uncertainty of the current reading, ΔV is the uncertainty of the voltage reading, ΔT_d is the uncertainty of temperature reading, ΔA is the uncertainty of the heating element area value.

The error of the measurement of the voltage and current of the power supply used in this study according to manufacturers are shown below:

Error in voltage = 0.1% reading + 0.2% rated output voltage

Error in current = 0.1% reading + 0.4% rated output current

The uncertainty of the surface temperature is acquired by taking into account the surface temperature standard deviation. By substituting these values into Equation 4, the uncertainty of the heat flux at the maximum heat flux condition in the confined structure pool boiling test is found to be 0.0519 W/cm^2, which is about 1.8% of the maximum heat flux obtained during the test.

2. Heat transfer coefficient

The heat transfer coefficients in this research was calculated from Equation 5.

$$h = \frac{q''}{\Delta T} \quad (5)$$

Where the h is the heat transfer coefficient, q" is the heat flux value, ΔT is the temperature difference between the heating element surface and the liquid saturation temperature. Consequently, the expression of heat transfer coefficient uncertainty can be shown as follow:

$$\frac{\Delta h}{h} = \sqrt{\left(\frac{\Delta q"}{q"}\right)^2 + \left(\frac{\Delta T}{T}\right)^2} \tag{6}$$

The uncertainty of heat transfer coefficient is about 4.6% in this research.

3. Enhancement percentage in heat transfer coefficient

The enhancement percentage in heat transfer coefficient in this research was calculated by Equation 7.

$$\text{enhancement } (\%) = \frac{h_c - h_{uc}}{h_{uc}} \times 100\% \tag{7}$$

Where h_c is the heat transfer coefficient of the confined pool boiling, h_{uc} is the heat transfer coefficient of the unconfined pool boiling. The uncertainty of enhancement percentage calculation can also be derived, as follow:

$$\frac{\Delta ehancement\ (\%)}{enhancement\ (\%)} = \sqrt{\left(\frac{\Delta h_c}{h_c}\right)^2 + \left(\frac{\Delta h_{uc}}{h_{uc}}\right)^2} \quad (8)$$

The uncertainty of enhancement percentage in heat transfer coefficient is about 6.5%.

4. Two-phase flow quality estimation

The two-phase flow quality in this research was calculated by the following equation.

$$\text{X}\ (\%) = \frac{\dot{V}_v \times \rho_v}{\dot{m}_{tot}} \times 100\% \quad (9)$$

Where X is the two-phase flow quality, $\dot{V}_v$ is the vapor volume flow rate, ρ_v is the vapor density, $\dot{m}_{tot}$ is the total mass flow rate. The uncertainty of the two-phase flow quality estimation can be calculated by Equation 10.

$$\frac{\Delta X}{X} = \sqrt{\left(\frac{\Delta \dot{V}_v}{\dot{V}_v}\right)^2 + \left(\frac{\Delta \dot{m}_{tot}}{\dot{m}_{tot}}\right)^2} \quad (10)$$

The uncertainty of the two-phase flow quality estimation is about 13.7% in this research.

APPENDIX B

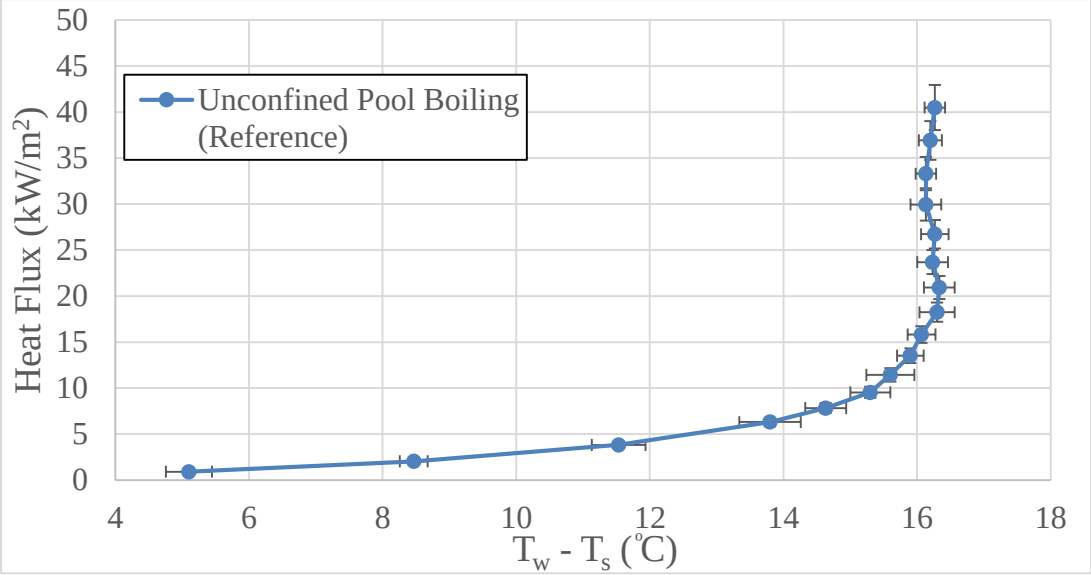

Figure 59. The unconfined boiling curve with error bar, case A

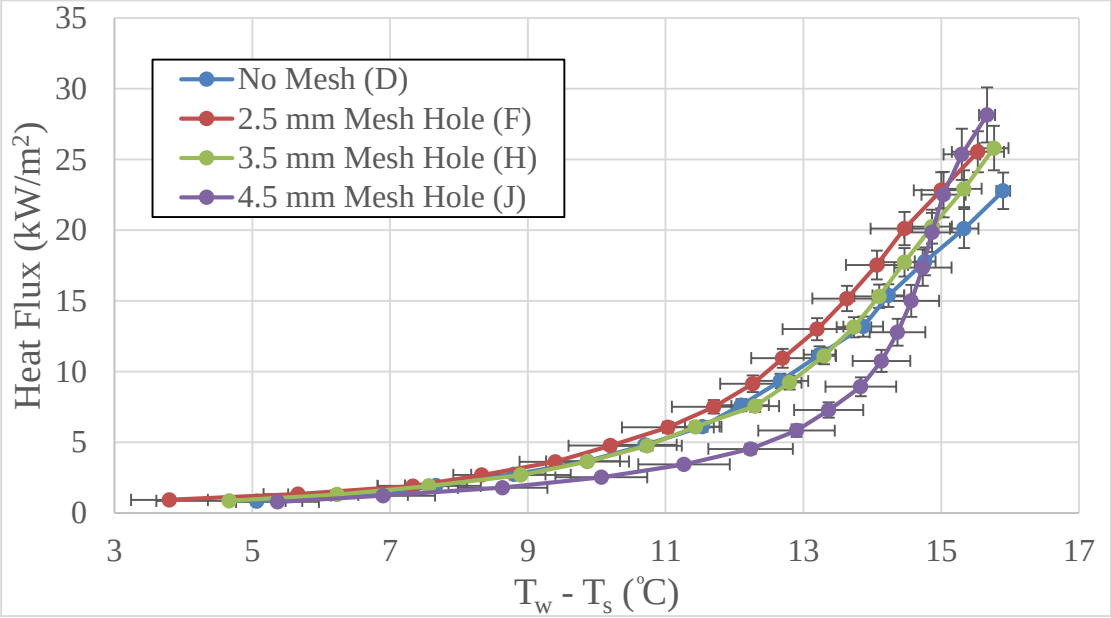

Figure 60. The boiling curves with error bar of the mesh orifice sizes when using 2 mm hole plate, case D, F, H and J

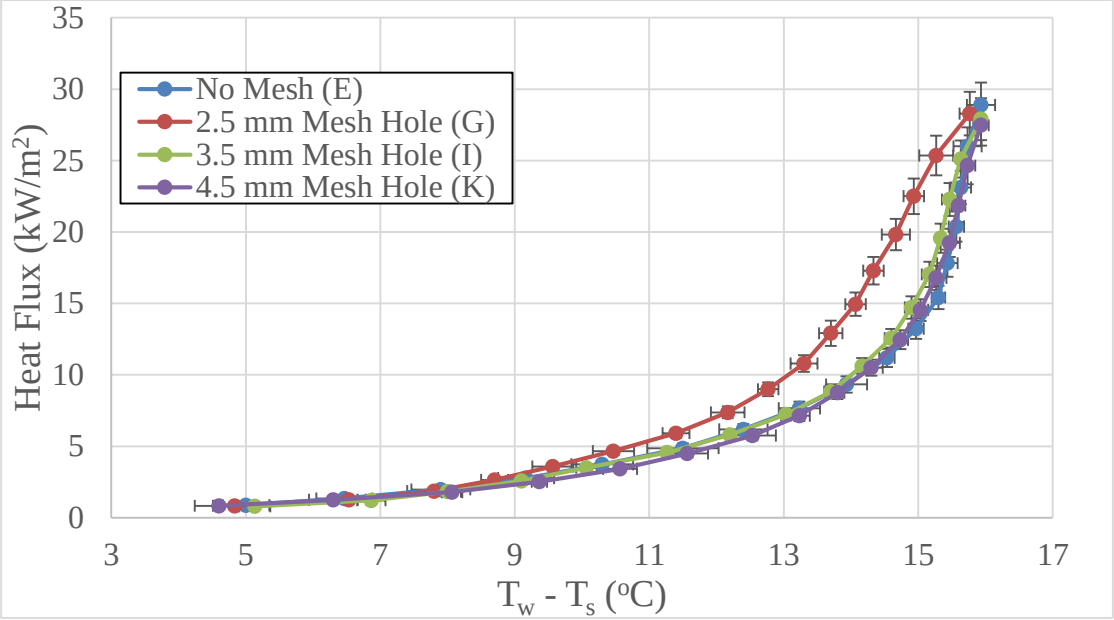

Figure 61. The boiling curves with error bar of the mesh orifice sizes when using 4 mm hole plate, case E, G, I and K